Sensitivity of the Cherenkov Telescope Array to TeV photon emission from the Large Magellanic Cloud

A. Acharyya,[1] R. Adam,[2,3] A. Aguasca-Cabot,[4] I. Agudo,[5] A. Aguirre-Santaella,[6] J. Alfaro,[7] R. Aloisio,[8] R. Alves Batista,[6] E. Amato,[9] E. O. Angüner,[10] C. Aramo,[11] C. Arcaro,[12] K. Asano,[13] J. Aschersleben,[14] H. Ashkar,[3] M. Backes,[15,16] A. Baktash,[17] C. Balazs,[18] M. Balbo,[19] J. Ballet,[20] A. Bamba,[21,22] A. Baquero Larriva,[23,24] V. Barbosa Martins,[25] U. Barres de Almeida,[26] J. A. Barrio,[23] D. Bastieri,[12] P. Batista,[25] I. Batkovic,[12] J. R. Baxter,[13] J. Becerra González,[27] J. Becker Tjus,[28] W. Benbow,[29] E. Bernardini,[12] M. I. Bernardos Martín,[5]★ J. Bernete Medrano,[30] A. Berti,[31] B. Bertucci,[32] V. Beshley,[33] P. Bhattacharjee,[34] S. Bhattacharyya,[35] C. Bigongiari,[36] A. Biland,[37] E. Bissaldi,[38,39] F. Bocchino,[40] P. Bordas,[4] J. Borkowski,[41] E. Bottacini,[12] M. Böttcher,[16] F. Bradascio,[42] A. M. Brown,[43] A. Bulgarelli,[44] L. Burmistrov,[45] S. Caroff,[34] A. Carosi,[36] E. Carquín,[46] S. Casanova,[47] E. Cascone,[48] F. Cassol,[49] M. Cerruti,[50] P. Chadwick,[43] S. Chaty,[50] A. Chen,[51] A. Chiavassa,[52,53] L. Chytka,[54] V. Conforti,[44] J. Cortina,[30] A. Costa,[55] H. Costantini,[49] G. Cotter,[56] S. Crestan,[57] P. Cristofari,[58] F. D'Ammando,[59] M. Dalchenko,[45] F. Dazzi,[60] A. De Angelis,[12] V. De Caprio,[48] E. M. de Gouveia Dal Pino,[61] D. De Martino,[48] M. de Naurois,[3] V. de Souza,[62] M. V. del Valle,[61] A. G. Delgado Giler,[62,14] C. Delgado,[30] D. della Volpe,[45] D. Depaoli,[63] T. Di Girolamo,[11,64] A. Di Piano,[44] F. Di Pierro,[52] R. Di Tria,[65] L. Di Venere,[38] S. Diebold,[66] M. Doro,[12] D. Dumora,[67] V. V. Dwarkadas,[68] C. Eckner,[34,69] K. Egberts,[70] G. Emery,[49] J. Escudero,[5] D. Falceta-Goncalves,[71] E. Fedorova,[36,72] S. Fegan,[3] Q. Feng,[29] D. Ferenc,[73] G. Ferrand,[74] E. Fiandrini,[32] M. Filipovic,[75] V. Fioretti,[44] L. Foffano,[76] G. Fontaine,[3] Y. Fukui,[77] D. Gaggero,[78] G. Galanti,[57] G. Galaz,[7] S. Gallozzi,[36] V. Gammaldi,[6] M. Garczarczyk,[25] C. Gasbarra,[79] D. Gasparrini,[79] A. Ghalumyan,[80] M. Giarrusso,[81] G. Giavitto,[25] N. Giglietto,[38,39] F. Giordano,[65] A. Giuliani,[57] J.-F. Glicenstein,[42] P. Goldoni,[50] J. Goulart Coelho,[82,83] J. Granot,[84,85] D. Green,[31] J. G. Green,[31] M.-H. Grondin,[67] O. Gueta,[25] D. Hadasch,[13] P. Hamal,[86] T. Hassan,[30] K. Hayashi,[13,87] M. Heller,[45] S. Hernández Cadena,[88] N. Hiroshima,[74] B. Hnatyk,[72] R. Hnatyk,[72] W. Hofmann,[63] J. Holder,[89] M. Holler,[90] D. Horan,[3] P. Horvath,[54] M. Hrabovsky,[54] M. Hütten,[13] M. Iarlori,[91] T. Inada,[13] F. Incardona,[55] S. Inoue,[74] F. Iocco,[11,64]★ M. Jamrozy,[92] W. Jin,[1] I. Jung-Richardt,[93] J. Jurýšek,[86] D. Kantzas,[34] V. Karas,[94] H. Katagiri,[95] D. Kerszberg,[96] J. Knödlseder,[97] N. Komin,[51] P. Kornecki,[58] K. Kosack,[20] G. Kowal,[71] H. Kubo,[13] A. Lamastra,[36] J. Lapington,[98] M. Lemoine-Goumard,[67] J.-P. Lenain,[99] F. Leone,[100] G. Leto,[55] F. Leuschner,[66] E. Lindfors,[101] T. Lohse,[102] S. Lombardi,[36] F. Longo,[103] R. López-Coto,[5] A. López-Oramas,[27] S. Loporchio,[38] P. L. Luque-Escamilla,[104] O. Macias,[105] P. Majumdar,[106] D. Mandat,[86] S. Mangano,[30] G. Manicò,[81] M. Mariotti,[12] P. Marquez,[96] G. Marsella,[81,107] J. Martí,[104] P. Martin,[97]★ M. Martínez,[96] D. Mazin,[13,31] S. Menchiari,[108] D. M.-A. Meyer,[70] D. Miceli,[12] M. Miceli,[107,40] J. Michałowski,[47] A. Mitchell,[93] R. Moderski,[41] L. Mohrmann,[63] M. Molero,[27] E. Molina,[4] T. Montaruli,[45] A. Moralejo,[96] D. Morcuende,[23] A. Morselli,[79] E. Moulin,[42] V. Moya,[23] R. Mukherjee,[109] K. Munari,[55] A. Muraczewski,[41] S. Nagataki,[74] T. Nakamori,[110] A. Nayak,[43] J. Niemiec,[47] M. Nievas,[27] M. Nikołajuk,[111] K. Nishijima,[112] K. Noda,[13] D. Nosek,[113] B. Novosyadlyj,[114] S. Nozaki,[31] M. Ohishi,[13] S. Ohm,[25] A. Okumura,[115,116] B. Olmi,[40,9] R. A. Ong,[117] M. Orienti,[59] R. Orito,[118] M. Orlandini,[44] E. Orlando,[103] S. Orlando,[40] M. Ostrowski,[92] I. Oya,[119] A. Pagliaro,[120] M. Palatka,[86] F. R. Pantaleo,[38,39] R. Paoletti,[108] J. M. Paredes,[4] N. Parmiggiani,[44] B. Patricelli,[36,121] M. Pech,[86] M. Pecimotika,[122] M. Persic,[103,123] O. Petruk,[33] E. Pierre,[99] E. Pietropaolo,[91] G. Pirola,[31] M. Pohl,[70] E. Prandini,[12] C. Priyadarshi,[96] G. Pühlhofer,[66] M. L. Pumo,[100,81] M. Punch,[50]

★ E-mail: m.isabel.bernardos@gmail.com (MIB); fabio.iocco.astro@gmail.com (FI); pierrick.martin@irap.omp.eu (PM)

F. S. Queiroz,[124,125] A. Quirrenbach,[126] S. Rainò,[65] R. Rando,[12] S. Razzaque,[127] A. Reimer,[90] O. Reimer,[90] T. Reposeur,[67] M. Ribó,[4] T. Richtler,[128] J. Rico,[96] F. Rieger,[63] M. Rigoselli,[57] V. Rizi,[91] E. Roache,[29] G. Rodriguez Fernandez,[79] P. Romano,[129] G. Romeo,[55] J. Rosado,[23] A. Rosales de Leon,[43] B. Rudak,[41] C. Rulten,[43] I. Sadeh,[25] T. Saito,[13] M. Sánchez-Conde,[6] H. Sano,[13] A. Santangelo,[66] R. Santos-Lima,[61] S. Sarkar,[56] F. G. Saturni,[36] A. Scherer,[7] P. Schovanek,[86] F. Schussler,[42] U. Schwanke,[102] O. Sergijenko,[72,130,131] M. Servillat,[58] H. Siejkowski,[132] C. Siqueira,[62] S. Spencer,[93,56] A. Stamerra,[36,133] S. Stanič,[35] C. Steppa,[70] T. Stolarczyk,[20] Y. Suda,[134] T. Tavernier,[86] M. Teshima,[31] L. Tibaldo,[97] D. F. Torres,[135] N. Tothill,[75] M. Vacula,[54] B. Vallage,[42] P. Vallania,[52,136] C. van Eldik,[93] M. Vázquez Acosta,[27] M. Vecchi,[14] S. Ventura,[108] S. Vercellone,[129] A. Viana,[62] C. F. Vigorito,[52,53] J. Vink,[105] V. Vitale,[79] V. Vodeb,[35] S. Vorobiov,[35] T. Vuillaume,[34] S. J. Wagner,[126] R. Walter,[19] M. White,[137] A. Wierzcholska,[47] M. Will,[31] R. Yamazaki,[138] L. Yang,[127,139] T. Yoshikoshi,[13] M. Zacharias,[126] G. Zaharijas,[35] D. Zavrtanik,[35] M. Zavrtanik,[35] A. A. Zdziarski,[41] V. I. Zhdanov,[72] K. Ziętara[92] and M. Živec[35]

Affiliations are listed at the end of the paper

ABSTRACT

A deep survey of the Large Magellanic Cloud at ∼0.1–100 TeV photon energies with the Cherenkov Telescope Array is planned. We assess the detection prospects based on a model for the emission of the galaxy, comprising the four known TeV emitters, mock populations of sources, and interstellar emission on galactic scales. We also assess the detectability of 30 Doradus and SN 1987A, and the constraints that can be derived on the nature of dark matter. The survey will allow for fine spectral studies of N 157B, N 132D, LMC P3, and 30 Doradus C, and half a dozen other sources should be revealed, mainly pulsar-powered objects. The remnant from SN 1987A could be detected if it produces cosmic-ray nuclei with a flat power-law spectrum at high energies, or with a steeper index 2.3–2.4 pending a flux increase by a factor of >3–4 over ∼2015–2035. Large-scale interstellar emission remains mostly out of reach of the survey if its >10 GeV spectrum has a soft photon index ∼2.7, but degree-scale 0.1–10 TeV pion-decay emission could be detected if the cosmic-ray spectrum hardens above >100 GeV. The 30 Doradus star-forming region is detectable if acceleration efficiency is on the order of 1−10 per cent of the mechanical luminosity and diffusion is suppressed by two orders of magnitude within <100 pc. Finally, the survey could probe the canonical velocity-averaged cross-section for self-annihilation of weakly interacting massive particles for cuspy Navarro–Frenk–White profiles.

Key words: acceleration of particles – Magellanic Clouds – dark matter – gamma-rays: general.

1 INTRODUCTION

It seems quite rare for a spiral galaxy like our Milky Way (MW) to be orbited by two star-forming satellites with the size and proximity of the Magellanic Clouds (James & Ivory 2011; Liu et al. 2011). It is even more valuable that one of the two is a disc that can be observed at high Galactic latitudes and under favourable inclination (Subramanian & Subramaniam 2010; Jacyszyn-Dobrzeniecka et al. 2016). The Large Magellanic Cloud (LMC) is an extraordinary opportunity for virtually all fields in astrophysics and constitutes a very convenient bridge between detailed studies of the MW and surveys of far more distant galaxies.

In the field of high-energy astrophysics, the LMC is one of the rare external star-forming galaxies on which spatially resolved studies can be carried out. At both GeV and TeV energies, with the performances of current instruments, only the Magellanic Clouds and Andromeda can be spatially resolved at a level allowing meaningful studies (Abdo et al. 2010a, b; Ackermann et al. 2016, 2017; Acero et al. 2009; Abdalla et al. 2018d). The LMC is among the most interesting because of its proximity and large angular size, low

inclination, and relatively high star formation activity. The LMC is also home to unique and extraordinary objects – the most luminous H II region of the Local Group, 30 Doradus, the most powerful pulsar, PSR J0537-6910, the remnant of the most nearby core-collapse supernova of modern times, SN 1987A – all of which are either confirmed or expected particle accelerators and gamma-ray emitters.

The current high-energy (HE) and very-high-energy (VHE) picture of the LMC was revealed by Fermi-LAT and H.E.S.S. observations and features five point sources, three of which are detected in both the GeV and TeV domains: the pulsar PSR J0537-6910 and its nebula, the supernova remnant N 132D, and the gamma-ray binary LMC P3; the other two are the pulsar PSR J0540-6919, whose pulsed magnetospheric emission is detected only in the GeV range, and the superbubble 30 Doradus C, detected only in the TeV range (Ackermann et al. 2015, 2016; Abramowski et al. 2015). The LMC also exhibits galaxy-scale diffuse emission that is most likely interstellar in origin and arises from the galactic population of cosmic-rays (CRs), on top of which kpc-scale emission components of uncertain origin were observed from regions seemingly devoid of

gas (Ackermann et al. 2016). These extended signals, however, were only detected in the ~100 MeV–100 GeV range and crucial higher energy information is missing to build a complete and coherent picture of CRs in the LMC. Emission in the ~100 GeV–100 TeV range probes more energetic CRs and an earlier stage of their life cycle because the bulk of higher energy CRs can escape the system more easily through more efficient diffusion.[1]

The future of VHE gamma-ray astronomy comprises the Cherenkov Telescope Array (CTA), whose construction recently started. CTA will be the first observatory in this energy range to be open to the community. It will be deployed on two sites, one in the Northern hemisphere, on the island of La Palma, Spain, and the other in the Southern hemisphere, in the Atacama desert, Chile. The southern site will give access, among other major targets, to the LMC, which other recent experiments such as the High-Altitude Water Cherenkov Observatory (HAWC) or the Large High-Altitude Air Shower Observatory (LHAASO) do not. In its final configuration, CTA will be an order of magnitude more sensitive than the current generation of Imaging Atmospheric Cherenkov Telescope (IACT) observatories, over a larger energy range from 20 GeV to 200 TeV, and with enhanced energy and angular resolution (Cherenkov Telescope Array Consortium et al. 2019). Thanks to a larger field of view, the instrument will have a survey capability that will be exploited in several ambitious Key Science Projects (KSPs) led by the CTA Consortium on proprietary time (Cherenkov Telescope Array Consortium et al. 2019). One such project is a deep survey of the LMC. It will consist of two phases: over the first 4 yr, a scan of the whole galaxy for a total of 340 h of observations, which corresponds to about 250 h of effective exposure; then, over the following 6 yr, a long-term monitoring of SN 1987A for about 150 h, if it was detected in phase one.

The scientific objectives are as many as a star-forming galaxy can offer: population studies of different classes of objects, analyses of the interstellar medium and the population of galactic CRs, and indirect searches of Dark Matter (DM). More specifically, the questions that gave rise to the project and their context are as follows:

CR lifecycle: What are the properties of CRs in the LMC at the galaxy scale, as revealed by their gamma-ray interstellar emission? The LMC is a different galactic setting compared to the MW (different geometry, metallicity, star formation rate density), and thus constitutes an opportunity to test our understanding of the way a CR population builds up over long times and large scales, and whether the conditions of CR transport differ from those inferred for our Galaxy (e.g. the respective role of diffusion and advection, or the magnitude of the diffusion coefficient). In particular, a deep survey may inform us about the CR lifecycle on small/intermediate scales, typically in the vicinity of major particle accelerators. Due to its lower CR background compared to the MW (Ackermann et al. 2016), the LMC is a good target to search for inhomogeneities in the CR distribution, resulting for instance from recent or sustained CR injection episodes and/or enhanced confinement near the source. This may be crucial for a proper understanding of the CR lifecycle and associated non-thermal emissions (D'Angelo et al. 2018).

Particle accelerators: What is the population of particle accelerators in the LMC, and does it differ in any way from the different

gamma-ray source classes we know of today? The handful of objects currently known are rare and extreme sources that make up the high-luminosity end of the population of gamma-ray emitters in the LMC. While fine spectral studies of this small number of extreme objects may be instrumental in solving some puzzles in our current understanding of particle acceleration (e.g. the electron-to-proton ratio, or the maximum attainable energy), CTA will push the census beyond out-of-the-norm sources and may usefully complement the survey of the MW. The favourable viewpoint of the LMC can make it easier to relate particle accelerators to their environment, owing to a reduced line-of-sight confusion and accurate distance estimate. The increase in the number of known gamma-ray sources in the LMC is also interesting as CTA deep observations will occur in the wake of other major surveys of the LMC in the X-ray (with eRosita, e.g. Sasaki et al. 2022) and radio (with the Australian Square Kilometre Array Pathfinder (ASKAP), e.g. Pennock et al. 2021) bands, providing an exquisite multiwavelength coverage of sources like supernova remnants (SNRs) or PWNe.

Nature of DM: What information can the CTA survey of the LMC bring on the nature of DM? The LMC has a mass of the order of 10^9 M$_\odot$ enclosed in 8.9 kpc and more than a half is due to a dark halo (van der Marel et al. 2002). Study of the rotational curves of the LMC revealed that it must contain a dark compact bulge with an anomalously high mass-to-luminosity ratio as large as $M/L \sim 20$–50 (Sofue 1999) compared to that calculated for the MW $M/L \sim 7$ (Sofue 2013). With these characteristics, the LMC is one more potentially suitable source for indirect searches of DM signal in our neighbourhood. In addition, such an investigation will take place in a specific global context, with different contamination of the hypothetical dark matter signal and various possible biases in the analyses compared to studies of the Galactic Centre (GC) or dwarf spheroidals.

In this paper, we provide a quantitative assessment of the detection prospects for the planned survey of the LMC. We developed a model for the entire galaxy emission at very high energies, from populations of discrete sources to interstellar emission on various scales and a possible DM annihilation component. Based on this model, we simulated CTA observations of the LMC using the latest instrument response functions estimates, and we analysed these data using existing prototypes for the CTA science tools. In addressing the above questions, we investigated the conditions for the survey realization under which its scientific potential would be maximized, especially the distribution of the exposure. Our goal is to go beyond what is already known and evaluate the prospects for detecting new sources and opening new avenues for high-energy astrophysics in the LMC.

The structure of the paper is as follows: In Section 2, we introduce the gamma-ray emission model used for the LMC, including a possible additional emission component produced from DM annihilation in the LMC. Section 3 is dedicated to the description of the simulation and analysis methods of CTA observations. In Section 4, results on detectability of the various classical emission components in our model are presented, as well as sensitivity curves for CTA detection of a DM-related signal. Finally, Section 5 is dedicated to conclusions.

Throughout the paper, the distance of the LMC is assumed to be $d = 50.1$ kpc (Pietrzyński et al. 2013). Sky positions are given in equatorial coordinates corresponding to the J2000.0 epoch. We will refer to objects such as LHA 120-N 157B as N 157B for short but emphasize that the full denomination should be used when searching for these objects in the CDS/Simbad data base.

---

[1] The time-scale to diffuse over 1 kpc is on the order of 1 Myr for 10 GeV particles, and on the order of 100 kyr for 10 TeV particles, assuming a diffusion coefficient as introduced in equation (5).

2 EMISSION MODEL

In this section, we describe the model that was developed for the gamma-ray emission of the LMC galaxy and used as input to the survey simulations. Since the VHE emission of the LMC is still largely unexplored, and only a handful of extreme objects have been detected so far, this model is based for the most part on simulated components, inspired by the knowledge of VHE source populations in the Galaxy and informed by observations of the LMC at other wavelengths (e.g. X-ray SNRs).

We considered a baseline model consisting of classical emission components that can be seen as guaranteed, in the sense that their contribution should exist even if some of their properties may differ from the assumed ones (e.g. the number of PWNe or the exact level or spectrum of interstellar emission): (i) the four already known VHE sources; (ii) population of SNRs, PWNe, and pulsar haloes; and (iii) interstellar emission from the galactic population of CRs.

We also envisioned possible emission from the 30 Doradus star-forming region but left it out of the baseline model as such a process cannot be considered to be sufficiently under control theoretically or observationally. We provide in the last subsection a description of the possible spectral and morphological properties of a more speculative component, which is the VHE emission from the annihilation of DM particles in the mass halo of the LMC.

2.1 Known point sources

In the VHE domain, there are currently four known sources in the LMC: N 157B interpreted as a pulsar wind nebula (PWN); N 132D interpreted as an SNR; 30 Doradus C interpreted as a superbubble (SB), although alternative explanations as an SNR exist; and LMC P3 clearly identified as a gamma-ray binary from the orbital modulation of the signal. Extensive physical context will be given for each known object in Section 4.2. We left aside other possible sources outside the LMC boundaries but within the survey footprint, such as those detected with the Fermi-LAT and whose spectrum could have been extrapolated to the CTA range (for instance, quasar PKS 0601-70).

All-known sources were modelled as point-like objects in our work, although depending on the actual nature of the emission from 30 Doradus C, it might be at the limit of being extended for CTA. The spectral models for the first three objects were taken from the physical model fits to the H.E.S.S. measurements in Abramowski et al. (2015), retaining the hadronic model for N 132D and leptonic model for 30 Doradus C (see Section 4.2 for a justification). There is currently no published broad-band physical model for LMC P3 and we used one that is currently being developed by one of us (N. Komin, private communication).

The source is modelled in a typical way for gamma-ray binaries (Dubus 2013). The compact object is assumed to be a pulsar that generates a relativistic magnetized outflow, and electron-positron pairs are accelerated in the interaction of this outflow with the stellar wind of the companion star. Gamma-ray emission from the system arises from inverse-Compton scattering of the population of energetic pairs in the cosmic microwave background and the stellar photon field of the massive star companion. A power-law distribution of positrons and electrons with index 1.5 and energy of 5×10^{37} erg in the 0.5–50 TeV range reproduces the H.E.S.S. measurements over the 1–10 TeV range (Abdalla et al. 2018a), without exceeding the Fermi-LAT upper limits above 10 GeV (Ackermann et al. 2016). The dense stellar photon field is assumed to have an effective temperature

40 000 K and an orbit-averaged energy density 291 erg cm^{-3}. Since the orbital light curve of LMC P3 remains poorly characterized as of now (Abdalla et al. 2018a), we left aside its modelling and analysis as a variable source.

2.2 Source populations: PWNe, SNRs, pulsar haloes

The four known objects listed above are the most extreme members of larger populations that CTA can be expected to unveil, at least partially, and it is one goal of this paper to quantify what fraction of those populations will be probed with the survey. We developed a population model consisting of four classes of sources: shell-like SNRs, interacting supernova remnants (iSNRs), and PWNe, which are the dominant classes of associated VHE sources in the Galaxy (Abdalla et al. 2018b, c), and pulsar haloes, which constitute an emerging class that has the potential to account for a significant fraction of currently unidentified VHE emitters (Linden et al. 2017; Sudoh, Linden & Beacom 2019; Albert et al. 2020; Martin et al. 2022b). We did not include in our model population components for gamma-ray binaries or microquasars.

The population synthesis framework is extensively described in Martin et al. (2022b, except for iSNRs), where it was applied to the MW. In what follows, we provide a concise description of the different population components and adaptation of the model to the case of the LMC, and we refer the reader to the original paper for more details.

2.2.1 Supernova explosions and pulsar birth

The four classes of objects considered for our model result from supernova explosions, so the rates for such events set the normalization of the various populations. The supernova (SN) rate in the LMC is uncertain by at least a factor of 2, with published values ranging from 0.002 to 0.005 SN yr^{-1} (van den Bergh 1991; Leahy 2017; Bozzetto et al. 2017; Ridley & Lorimer 2010). Estimates based on the present-day star formation rate or massive star population are shaky because the star formation history of the LMC was not steady over the past ~100 Myr (Harris & Zaritsky 2009), so the current SN rate and SN types ratio are partially disconnected from the current star formation rate. Building upon the works and arguments of van den Bergh (1991), Leahy (2017), and Maggi et al. (2016), we considered as baseline an SN rate of $r_{SN} = 0.002$ SN yr^{-1}, with a ratio of core-collapse to thermonuclear supernovae (SNe) of $r_{CC}/r_{Ia} = 1.3$. After a calibration of the population model to known VHE sources in the Milky Way, we assumed that the fraction of core-collapse SNe producing neutron stars is 0.75 (Lorimer et al. 2006), such that the rate of pulsar birth in the LMC is $r_{PSR} = 0.000\,85$ SN yr^{-1}. The source population model starts with the random generation of supernovae over the last 400 kyr (the lifetime of the longest lived objects, pulsar haloes), with random generation of a number of events from a Poisson distribution, random generation of an age in a uniform distribution, then random generation of a SN type in a binomial distribution and finally, for core-collapse SNe, random selection of those giving birth to pulsars again from a binomial distribution.

2.2.2 Locations of objects

In a first stage, SNe, and their pulsars when appropriate, are randomly distributed over the LMC according to the following prescription: thermonuclear SNe are uniformly distributed over the gas disc of the galaxy, as defined in Section 2.3, while core-collapse SNe are

distributed among the different massive star-forming regions of the LMC in proportion to their ionizing luminosity, following the list of H II regions and their properties in Pellegrini et al. (2012) and with an added random scatter in position by $0.05°$ to account for the typical extent of the regions. In a second stage, we include in our model the present-day knowledge of more than 60 real SNRs in the LMC, with X-ray and dynamical properties derived in a homogeneous way in Maggi et al. (2016) and Leahy (2017). For each real SNR, we select among the model SNRs the one with the same type and the smallest distance in the (age, density, energy) space. That a proper match can be obtained is guaranteed, from the statistical point of view, by the fact that the properties of model SNRs were sampled from distributions inferred from observations of real SNRs in the LMC (see below). For those model objects for which an association is made, the initial random location is replaced by the location of the actual X-ray SNR, and this affects not only the model SNR but also the model PWN, if any, for objects resulting from core-collapse SNe.

2.2.3 Interstellar conditions

The evolution of all systems and their non-thermal radiation are influenced by the surrounding interstellar conditions, directly or indirectly. For each system, the surrounding magnetic field strength is randomly sampled from a uniform distribution with mean $4\,\mu G$ and half-width $3\,\mu G$ (see Section 2.3 for more details). Similarly, the interstellar radiation field is taken to vary from one object to the other and it was randomly drawn from a uniform distribution between two extreme field models (see Section 2.3 for more details). In both cases, this is meant to incorporate in the model the fact that some objects will arise in star-forming regions with intense radiation fields, while others will be born in more isolated and quiescent environments. Last, the interstellar gas density was also taken to vary from one object to the other, and its value was randomly sampled from a lognormal distribution, inspired by those inferred in Leahy (2017) for the upstream medium of SNRs detected in X-rays, that we approximated as a single distribution with mean $\mu_{log(n_H)} = -1.0$ and standard deviation $\sigma_{log(n_H)} = 0.9$ for n_H in units of $H\,cm^{-3}$.

2.2.4 SNRs

The modelling of the population of SNRs is based on the framework presented in Cristofari et al. (2013). It implements analytical prescriptions for the dynamics of the forward shock in the remnant and computes the evolution of a parametrized distribution of non-thermal particles energized at the shock and trapped in the remnant upon downstream advection. Different treatments are used depending on whether the SNR results from a thermonuclear or core-collapse explosion: in the former case, the expansion occurs in a uniform circumstellar medium, while in the latter case it occurs in a layered wind-blown cavity shaped by the progenitor massive star. The model is valid over the free expansion and Sedov–Taylor stages and breaks down as the forward shock becomes radiative. We assumed a lifetime $\tau_{SNR} = 60\,kyr$ for model SNRs but some do not even reach that limit as they become radiative before.

2.2.5 iSNRs

The modelling of the population of iSNRs was inspired from a similar work performed in the context of the anticipation of the planned Galactic Plane Survey with CTA (Remy et al. 2022). The modelling

starts with the generation of a synthetic population of molecular clouds, based on the inferred mass spectrum and cloud density in the LMC (Fukui et al. 2008), and extrapolating it in the range of masses where the catalog is not complete. The probability for a cloud to be interacting with an SNR is parametrized as a power law in cloud mass and calibrated on the basis of what is observed in our Galaxy (for a molecular cloud population relevant to the Galaxy). Ultimately, a flat probability distribution seems to be appropriate. For those clouds in interaction, the proton spectrum in each remnant is randomly sampled from parameter distributions derived from the study of such systems in the MW. It is typically a broken power-law spectrum with relatively soft indices. A synthetic population is generated by computing the pion decay spectrum associated with the interacting system,[2] given the random-sampled particle spectrum and cloud density. These mock iSNRs are then assigned to the mock core-collapse SNRs not associated with existing X-ray remnants, after removing the brightest object in the population to account for the fact that we already have a prominent interacting system in our emission model, N 132D.

2.2.6 PWNe

The modelling of the population of PWNe is based on the model presented in Mayer et al. (2012) and updated in Abdalla et al. (2018c). It starts with the random generation of the pulsar population with initial spin periods and magnetic fields sampled from typical distributions for young pulsars, which determines the spin-down history of the pulsars and sets the power available for the production of non-thermal particles in each system. The development of a model PWN until its randomly selected age is described as the expansion of a spherical nebula over three dynamical stages, with its content of non-thermal particles evolving as a result of injection, energy losses, and escape. We assumed a lifetime $\tau_{PWN} = 100\,kyr$ for PWNe, a limit consistent with most of the observed population (Abdalla et al. 2018c), after which they transition to the halo stage (see below).

2.2.7 Pulsar haloes

The modelling of the population of halos is based on the diffusion-loss model implementation presented in Martin, Marcowith & Tibaldo (2022a), in which electron–positron pairs injected at a central point diffuse away spherically in a medium characterized by a two-zone concentric structure for diffusion properties, with an outer region typical of the average interstellar medium (ISM) and an inner region where diffusion is suppressed down to values inferred for the Geminga pulsar halo (Abeysekara et al. 2017). Particle injection into the halo is assumed to start at the end of the PWN phase, when the pulsar exits it original nebula as a result of its natal kick, with a spectrum that is similar in shape and normalization to that fed into the PWN. Particles experience radiative losses in the randomly sampled magnetic field and radiation fields for the system (see above). The different scalings of the diffusion and loss processes with particle energy result in a characteristic energy-dependent morphology for halos. We assumed a lifetime $\tau_{HALO} = 400\,kyr$ for the mock haloes, which is dictated by the characteristic age of the Geminga pulsar.

---

[2]The gamma-ray production cross section used for these calculations is taken from Kafexhiu et al. (2014), as implemented in the NAIMA PYTHON package (Zabalza 2015).

Table 1. Summary of the main parameters used in the modelling of the source population model.

Parameter	Unit	Value
Supernovae		
Supernova rate r_{SN}	SN yr^{-1}	0.002
ccSNe / SNe Ia ratio r_{CC}/r_{Ia}	–	1.3
Pulsar-producing fraction	–	0.75
Pulsars		
Initial magnetic field B_0	G	$\mathcal{L}(12.65, 0.55)$
Initial period P_0	ms	$\mathcal{N}(50, 35)$
Braking index n	–	3.0
Neutron star inertia I_{NS}	g cm^2	10^{45}
Neutron star radius R_{NS}	km	12
SNRs		
Ejecta mass M_{ej}	M$_\odot$	1.4 for SNe Ia, 5.0 for ccSNe
Ejecta energy E_0	erg	$\mathcal{L}(50.7, 0.5)$
Particle injection distribution S_{SNR}	–	PLEC
Particle distribution index α	–	$\mathcal{U}(2.3, 0.1)$
Particle injection efficiency η_{SNR}	–	$\mathcal{U}(0.2, 0.1)$
Electron-to-proton injection ratio ξ	–	10^{-3}
Age limit	yr	6×10^4
PWNe		
Nebula magnetic field initial strength	G	5×10^{-5}
Nebula magnetic field evolution index	–	0.6
Particle injection distribution S_{PWN}	–	BPLEC
Particle distribution index below break α_1	–	1.5
Particle distribution index above break α_2	–	$\mathcal{U}(2.4, 0.4)$
Particle distribution break energy E_{brk}	GeV	100
Particle distribution cut-off energy E_{cut}	TeV	$\mathcal{U}(500, 300)$
Particle injection efficiency η_{PWN}	–	$\mathcal{U}(0.7, 0.3)$
Age limit	yr	10^5
Pulsar halos		
Suppressed diffusion region size R_{SDR}	pc	50
Suppressed diffusion normalization at 100 TeV D_0^{SDR}	cm^2 s^{-1}	4×10^{27}
Average interstellar diffusion normalization at 10 GeV D_0^{ISM}	cm^2 s^{-1}	10^{29}
Diffusion rigidity scaling index δ_D	–	1/3
Particle injection distribution S_{HALO}	–	$S_{HALO} = S_{PWN}$
Particle injection efficiency η_{HALO}	–	$\eta_{HALO} = \eta_{PWN}$
Age limit	yr	4×10^5

Notes. Notes to the table:
$\mathcal{U}(\mu, \sigma)$ means uniform distribution of mean and half-width μ and σ.
$\mathcal{N}(\mu, \sigma)$ means normal distribution of mean and standard deviation μ and σ.
$\mathcal{L}(\mu, \sigma)$ means lognormal distribution of mean and standard deviation of the logarithm μ and σ.
(B)PLEC stands for (broken) power law with exponential cut-off.

2.2.8 Model calibration

The population synthesis model features a number of free parameters that should be set to provide a representative emission distribution at a population level. It is not possible to calibrate it on LMC observations owing to the small number of sources detected so far, and especially because the latter are most likely extreme objects. Instead, the model was calibrated against the population of known Galactic sources in the VHE range, as described in Martin et al. (2022b), which resulted in a selection of possible values and statistical distributions for the parameters governing the evolution of the different object classes. Once calibrated, the population synthesis could be run for the specific conditions of the LMC. The parameters eventually adopted are summarized in Table 1.

2.2.9 Model realization

The random realization of the source population model that we used in our simulations and analyses of the survey contains 71 SNRs, 10 iSNRs, 91 PWNe, and 167 pulsar halos within the prescribed age or dynamical limits. Fig. 1 displays the 1–10 TeV energy flux of mock sources as a function of their age, compared to the H.E.S.S. 99 per cent confidence level upper limit on SN 1987A (for observations done over 2003–2012; see Komin, Haupt & H.E.S.S. Collaboration 2019) and the foreseen CTA 5σ detection threshold as determined in Section 4.1. The model population, calibrated on Galactic objects, extends nicely up to the H.E.S.S. sensitivity upper limit. In this realization, only two PWNe exceed it, which is consistent with the currently detected population which comprises two pulsar-powered sources. This confirms that the population is
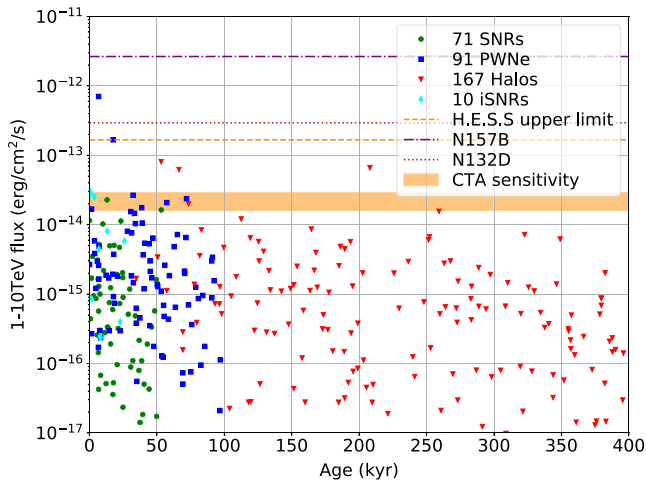
Figure 1. Luminosity as a function of age for the random realization of our PWNe, SNRs, iSNRs, and pulsar halos population model for the LMC. Overlaid is the upper limit on point-like emission from H.E.S.S. (using the limit on SN 1987A from Abramowski et al. 2015), and the range of threshold luminosity for a detection with significance above 5σ with CTA (see Section 4.1). Also shown are the levels of emission for the strongest (N 157B) and weakest (N 132D) of the currently known sources.

well normalized and that currently detected objects are the most extreme members of their class. We kept these high luminosity mock objects in the population model as they could well be there and have escaped detection with H.E.S.S. simply because the H.E.S.S. survey did not uniformly cover the full extent of the LMC. The discussion on the fraction of the population that could be accessible to CTA is presented in Section 4.

Fig. 2 shows the spectra of all individual objects in the realization of our source population model that we used for simulation and analysis. Fig. 3 shows the layout and sizes of the source population model objects over the LMC, on top of an Hα image of the galaxy. The built-in correlation of most sources with H II regions is clearly apparent (except with 30 Doradus, which we decided to treat separately) and the figure makes it clear that this could result in some degree of source confusion. In some places especially, for instance south of 30 Doradus towards H II regions N158, N159, and N160 (DEM L269, L271, L284) or west of the LMC towards H II region N82 (DEM L22), the crowding is quite high.

Most objects have radial sizes below 0.05°, with a handful of rare PWNe and SNRs reaching up to 0.1°, which means that the majority of the population will be detected as point-like objects for CTA. In practice, in the survey simulations described in Section 3, the morphological information from the source population models was simplified. All PWNe and SNRs were treated as uniform brightness disks if their projected radii is above 3 arcmin, and as point sources otherwise. For pulsar halos, although the model does include the full energy-dependent morphology, they were modeled as projected two-dimensional Gaussian intensity distribution with a size characteristic of that obtained at 3 TeV, except if their 95 per cent containment radius is smaller than 3 arcmin, in which case they were treated as point sources (see the discussion on halo size estimate in Martin et al. 2022b).

2.3 Interstellar emission from the LMC's population of CRs

Interstellar emission was computed under the assumptions of steady CR injection from an ensemble of point sources, followed by diffu-

sive transport in the ISM and interaction with model distributions for interstellar components (gas, photon, and magnetic fields). The final templates for interstellar emissions result from convolving a model distribution of sources with average emission kernels for pion-decay and inverse-Compton processes, plus a correction by the actual gas distribution for the pion-decay component. Some of the assumptions introduced below are inspired by studies of our Galaxy but there is no solid observational evidence that CR transport in the LMC and the MW behaves the same, especially in the VHE regime. So when assessing the detectability of interstellar emission from the LMC, we will also envision the possibility that some features of our models depart from their baseline values. In what follows, we provide a concise description of the preparation of the large-scale interstellar emission components.

2.3.1 CR source distribution

In star-forming galaxies, CRs are mainly energized by the mechanical power provided by massive stars in the form of winds and outflows, core-collapse SN explosions, and compact objects, and an additional contribution comes from thermonuclear SN explosions. Lacking a solid understanding of the relative contribution of each class of CR accelerators to the overall CR injection luminosity, we simplified the problem by considering that injection occurs in massive-star-forming regions without specifying the objects actually involved or their respective particle acceleration properties. We did not include a source distribution model for injection by thermonuclear SNe, which can be expected to be more uniformly spread over the galaxy. Instead, we considered the alternative scenario of a distribution of CR injection sites that is less clustered and confirmed that this has no effect on the detection prospects for this component. As a tracer for CR injection sites related to the massive star population, we used a selection of H II regions from the catalog of Pellegrini et al. (2012), retaining the most luminous ones, that are populated enough for consistency with our steady-state injection assumption, but excluding the most powerful 30 Doradus, that we will handle separately owing to its extraordinary status. For the 138 regions in our sample, we converted H α luminosities into ionizing luminosities, based on the morphological classification and escape fraction determined by Pellegrini et al. (2012), and we took ionizing luminosity as a measure of the richness of each star cluster, to which we assumed CR injection power is proportional. Eventually, the CR source distribution is of the form:

$$M_{\mathrm{CR}}(\boldsymbol{r}) = \sum_k L_k \delta(\boldsymbol{r} - \boldsymbol{r_k}) \qquad (1)$$

with a total of 138 injection sites located at the positions $\{\boldsymbol{r_k}\}$ of selected H II regions and having relative injection luminosities $\{L_k\}$ proportional to ionizing luminosities. More details about the selection of H II regions and derivation of their properties can be found in Appendix A.

2.3.2 CR injection spectrum

We restricted ourselves to CR protons and electrons, treating nuclei via a nuclear enhancement factor when computing hadronic emission (thereby neglecting differences in source spectra for the different species). We assumed that CRs at injection in the ISM follow a power-law distribution in momentum p starting at $1\,\mathrm{GeV}/c$ and exponentially cutting off at $p_{\mathrm{cut, p}} = 1\,\mathrm{PeV}/c$ for protons and $p_{\mathrm{cut, e}} = 100\,\mathrm{TeV}/c$ for electrons. The latter value is in agreement with the
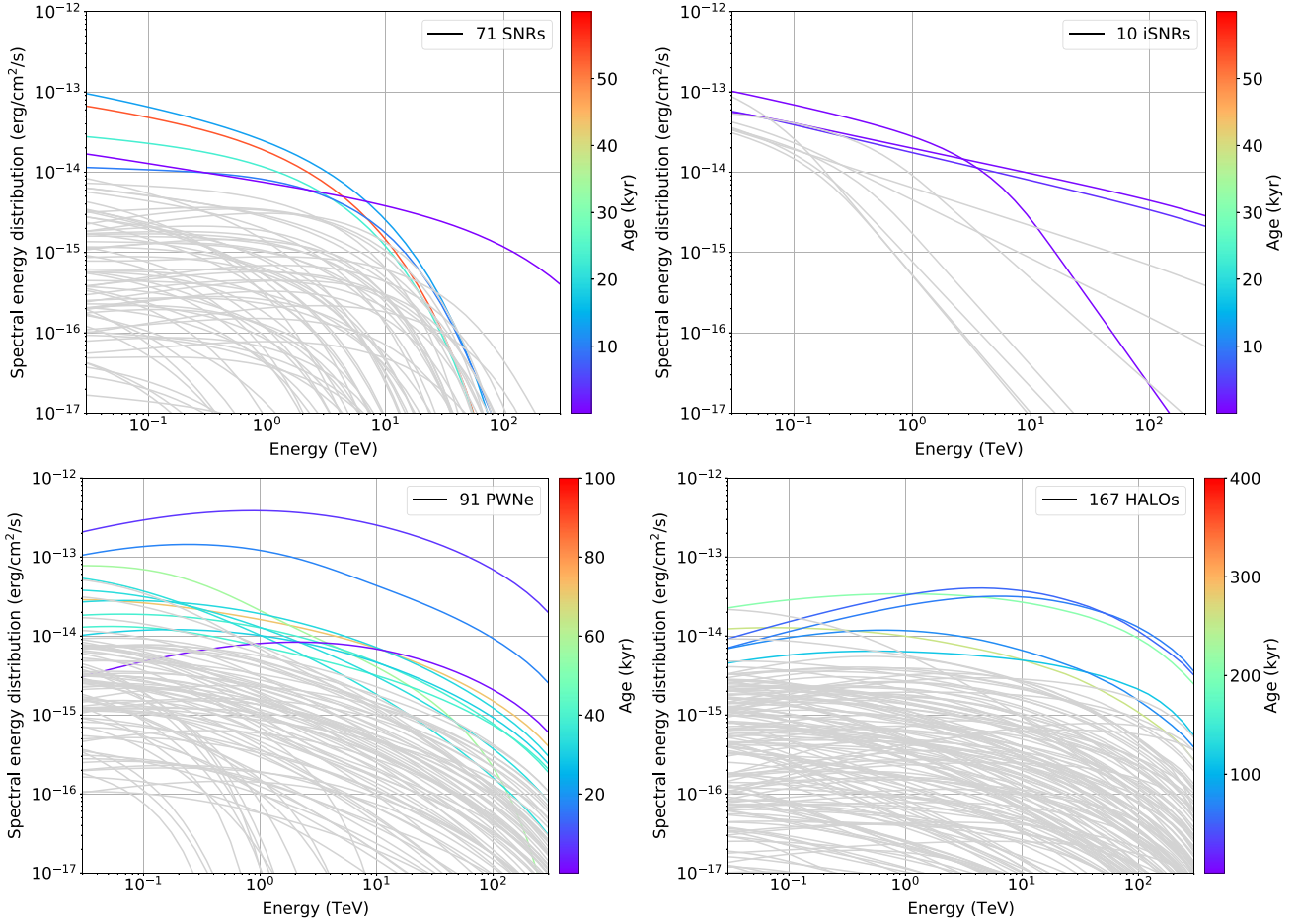
Figure 2. Spectra of all individual objects in the realization of our source population model. Shown in light gray are objects below the approximate sensitivity level of the survey (see Section 4.1). Curve colours encode the age of the members in each source class (with a scaling specific to each class).

highest electron energies inferred in SNRs in the LMC (Hendrick & Reynolds 2001). The CR power spectral density for species X among protons or electrons (respectively specified with subscripts p or e) reads

$$\frac{\mathrm{d}P_{X,\mathrm{inj}}(p)}{\mathrm{d}p} = P_{X,0} \left(\frac{p}{p_0} \right)^{-\alpha_X} \mathrm{e}^{-\frac{p}{P_{X,\mathrm{cut}}}} \tag{2}$$

$$= \beta \frac{\mathrm{d}P_{X,\mathrm{inj}}(E)}{\mathrm{d}E} = \beta Q_X(E), \tag{3}$$

where E is kinetic energy and $\beta = v/c$. For our baseline scenario, we started from assumptions inspired by our knowledge of the CR population of the MW and adopted $\alpha_p = 2.45$ and $\alpha_e = 2.65$ (we neglected the possibility of breaks in the injection spectra). These values are representative of the higher energy part of the injection spectra in the widely used diffusion + reacceleration propagation models tested against a variety of observables (Trotta et al. 2011; Orlando 2018). This assumption is however considered a minimal baseline model and the impact of a CR population with a harder spectrum will be discussed below.

2.3.3 CR injection power

The total CR injection power is assumed to be constant in time, at a level corresponding to the long-term average of CR injection by SNe exploding at a rate r_{SN}, each event releasing $E_{SN} = 10^{51}$ erg of mechanical energy, a fraction η of which is tapped by CR acceleration:

$$\int \frac{\mathrm{d}P_{X,\mathrm{inj}}(E)}{\mathrm{d}E} E \mathrm{d}E = \eta_X r_{SN} E_{SN}. \tag{4}$$

We adopted $\eta_p = 10^{-1}$, $\eta_e = 10^{-3}$, and $r_{SN} = 0.002 \, \mathrm{SN \, yr^{-1}}$ as previously. This translates into a total $6.5 \times 10^{39} \, \mathrm{erg \, s^{-1}}$ for the whole galaxy, to be distributed among the different massive star-forming regions in proportion to their ionizing luminosity and then shared into CR electrons and protons in a 1:100 ratio.

2.3.4 CR propagation

CR transport away from each injection site into the ISM is assumed to occur as a result of spatial diffusion limited by energy losses. Both terms are taken as constant and isotropic over the volume of the galaxy. Diffusion is controlled by a momentum-dependent coefficient of the form:

$$D(p) = \beta D_0 \left(\frac{p}{p_0} \right)^{\delta} \tag{5}$$

$$\delta = 1/3 \tag{6}$$

$$D_0 = 10^{29} \, \mathrm{cm^2 \, s^{-1}} \text{ at } p_0 = 10 \, \mathrm{GeV}/c \tag{7}$$

The normalization and index adopted here are typical of the fitted values obtained in the diffusion + reacceleration propagation models
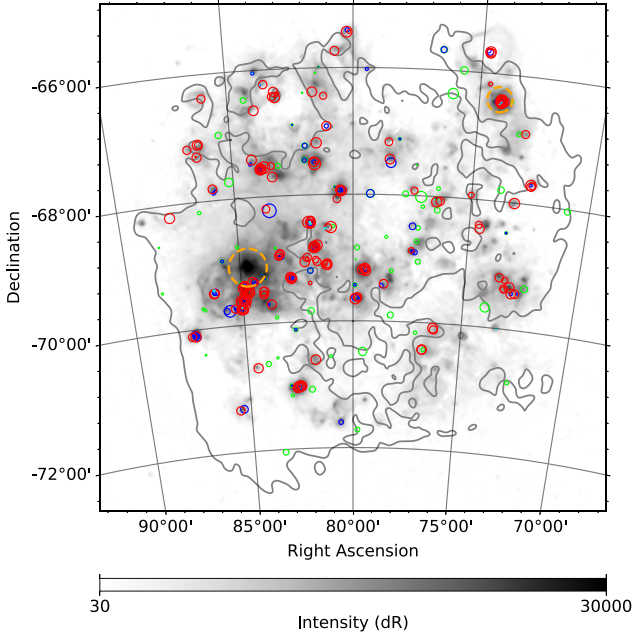
Figure 3. Spatial distribution of source population mock objects over the LMC. The background image is from the Southern H-Alpha Sky Survey Atlas (Gaustad et al. 2001) and displays H α emission intensity in dR units on a logarithmic scale, thus providing a view on ionized gas distribution in the galaxy. The contours trace the typical extent of the atomic gas disc (Kim et al. 2003). The small and large dashed orange circles indicate the locations of regions N11 and 30 Doradus, respectively. Model SNRs, iSNRs, PWNe, and pulsar halos are overlaid as green, cyan, blue, and red circles, respectively. For SNRs or iSNRs and PWNe, the size correspond to the forward shock and nebula outer radius, respectively, while the sizes of haloes correspond to the 95 per cent containment radius of the 3 TeV emission.

from which we borrowed the injection spectra (Trotta et al. 2011; Orlando 2018). Smaller values of a few 10^{28} cm^2 s^{-1}, as frequently found in the literature (e.g. Evoli, Aloisio & Blasi 2019), would lead to interstellar emission in excess of the Fermi-LAT constraint at 10 GeV (see Section 2.6, but also a comment in Appendix B). Energy loss processes include hadronic interactions for CR protons, synchrotron, inverse-Compton scattering, and Bremsstrahlung radiation for CR electrons, plus Coulomb and ionization losses for both species. They occur in homogeneous gas, photons, and magnetic field distribution models that will be introduced below. Protons and electrons spatial distributions are obtained by solving the diffusion-loss equation for a point-like and stationary source (see Appendix B for the details)

2.3.5 Emission kernels

Projected particle angular distribution around a source are computed by integrating the particle spatial distributions (defined in Appendix B) along the line of sight over a thickness $2H$ and for the assumed distance d to the LMC:

$$\frac{dN}{dE\,d\Omega}(\theta, E) = 2d^2 \times \int_0^H \frac{dN}{dE\,dV}\left((\theta^2 d^2 + \ell^2)^{1/2}, E\right) d\ell. \quad (8)$$

The half-thickness H is taken as representative of the target distribution: a 180 pc gas disk scale height for CR protons (Kim et al. 1999), and a 1 kpc magnetic and radiation field halo for CR electrons.

Inverse-Compton and pion-decay angular profiles around a source are computed as[3]

$$\frac{d\Phi_{IC}}{dE_\gamma\,d\Omega}(\theta, E_\gamma) = \iint \frac{dN_e}{dE_e\,d\Omega}\frac{dF_{IC}}{dE_\gamma}(E_e, E_\gamma, \nu)\frac{U(\nu)}{h\nu}\,d\nu\,dE_e, \quad (9)$$

$$\frac{d\Phi_{PD}}{dE_\gamma\,d\Omega}(\theta, E_\gamma) = \int \frac{dN_p}{dE_p\,d\Omega}\frac{dF_{PD}}{dE_\gamma}(E_p, E_\gamma)n_H,\,dE_p, \quad (10)$$

where dF_{IC}/dE_γ is the scattered photon spectrum per electron of energy E_e and target photon of energy $h\nu$, while dF_{PD}/dE_γ is the decay photon spectrum per relativistic proton of energy E_p and target proton. Quantities U and n_H are the photon and gas target densities and we use for all injection sites the same values that are averages over the galaxy (more details are provided below). The resulting emission kernels are convolved with the CR source distribution defined above:

$$\mathcal{S}_{PD,IC}(\boldsymbol{r}, E_\gamma) = M_{CR}(\boldsymbol{r}) \otimes \frac{d\Phi_{PD,IC}}{dE_\gamma\,d\Omega}(\theta, E_\gamma), \quad (11)$$

$$= \sum_k \frac{d\Phi_{PD,IC}^k}{dE_\gamma\,d\Omega}(\|\boldsymbol{r} - \boldsymbol{r_k}\|, E_\gamma), \quad (12)$$

where the sum runs over k injection sites. In the equations above, gamma-ray photon energy was denoted as E_γ, to distinguish it from proton or electron kinetic energy E_p or E_e, but in the following we will denote it simply as E for convenience. For the pion decay component, a nuclear enhancement factor of 1.753 is introduced to account for the contribution of helium and heavier nuclei in CRs and the ISM (computed from Mori 2009, under the assumption of a 0.4 solar metallicity medium[4]). The resulting emission cube is rescaled by a gas column density map of the LMC to recover the actual gas distribution structure of the galaxy, using the following formula:

$$\mathcal{S}_{PD}^{obs}(\boldsymbol{r}, E_\gamma) = \mathcal{S}_{PD}(\boldsymbol{r}, E_\gamma) \times \frac{N_H^{obs}(\boldsymbol{r})}{2n_H z_{gas}}, \quad (13)$$

where the denominator of the fraction on the right-hand side is the average gas column density assumed in this work, computed from parameters defined in the next paragraph, while the numerator refers to the gas column density map derived from observations of the atomic and molecular gas phases (plus a correction for the dark gas), as introduced in Abdo et al. (2010a).

2.3.6 Interstellar gas

We define the gas disc of the LMC as having a radius $R_{gas} = 3.5$ kpc and a scale height $z_{gas} = 0.18$ kpc (Staveley-Smith et al. 2003; Kim et al. 1999). Within this radius, the total interstellar atomic hydrogen mass of the LMC is $M_{HI} = 3.8 \times 10^8$ M$_\odot$ (Staveley-Smith et al. 2003), and the molecular hydrogen mass is $M_{H_2} = 5.0 \times 10^7$ M$_\odot$ (Fukui et al. 2008). Following Abdo et al. (2010a), building upon the results of Bernard et al. (2008), we increased these amounts by 50 per cent to account for the presence of dark neutral gas that could

---

[3]The calculations were performed with the NAIMA package (Zabalza 2015).
[4]We used the median metallicity found in Cole et al. (2005) from intermediate-age and old field stars in the central regions of the LMC. This is however a simplification since the metallicity in the LMC appears to be strongly position-dependent (see Lapenna et al. 2012, and references therein). Interestingly, the 0.4 solar metallicity is consistent with the value obtained for the Fe element from X-ray spectroscopy of SNRs in the LMC (Maggi et al. 2016), although the latter study also shows element-wise variations.

be cold atomic gas with optically thick 21 cm line emission and/or pure molecular hydrogen gas with no CO emission. The content of ionized hydrogen gas is computed following Paradis et al. (2011), using electron density $n_e = 1.52\,\mathrm{cm}^{-3}$ and mean H α intensity of 26.3 Rayleigh corresponding to the regime defined as 'typical H II regions' in the article. This yields a total ionized hydrogen mass of $M_{H II} = 1.7 \times 10^7\,\mathrm{M_\odot}$, and thus a total interstellar hydrogen mass of $M_H = 6.6 \times 10^8\,\mathrm{M_\odot}$, with an estimated uncertainty of $2.1 \times 10^8\,\mathrm{M_\odot}$ that stems mostly from the uncertain amount of dark neutral gas (Bernard et al. 2008). Assuming a typical volume for the gas disc of the galaxy of $V = 2\pi R_{gas}^2 z_{gas}$, the average hydrogen density of the LMC is $n_H = 1.93\,\mathrm{H\,cm}^{-3}$.

2.3.7 Interstellar magnetic field

The interstellar magnetic field can be expected to vary across the extent of the galaxy and fluctuate on ~50−100 pc scales, for instance because of the stirring by SNRs and SBs. In the context of source populations, the magnetic field in different locations of the galaxy was randomly sampled from a uniform distribution with mean 4 µG and deviation 3 µG. The minimum 1 µG value corresponds to the strength of the ordered component of the magnetic field only, while the 4 µG mean value corresponds to the average strength for the ordered plus random components (Gaensler et al. 2005). What the maximum strength could be is unclear, as are the frequency and scales at which it is encountered, so we adopted a uniform and symmetric distribution extending up to 7 µG by lack of any better prescription. Yet, in the context of interstellar emission on large scales, the diffusion framework used here cannot handle inhomogeneous conditions so the magnetic field strength considered in electron diffusion is uniform at a value of 4 µG. The magnetic field topology can have an influence on particle transport, for instance the specific orientation of the regular component of the field or the spatially-dependent ratio of turbulent to regular components (see e.g. Gaggero et al. 2015a, in the context of the gamma-ray interstellar emission from the MW). Exploring these effects is however beyond the capabilities of the diffusion model framework used here, which cannot handle anisotropic diffusion.

2.3.8 Interstellar radiation field

The model for the interstellar radiation field (ISRF) was developed from the work of Paradis et al. (2011), in which the broad-band infrared dust emission of the LMC was linearly decomposed into gas phases and fitted to dust emission models, eventually yielding dust emissivity spectra $Q_Y(\nu)$ per unit column density for each gas phase Y and levels of stellar radiation heating the dust in each phase. From these and the average gas column densities corresponding to the adopted gas disc model, we could construct a complete ISRF average model that, for simplicity, we approximated as a sum of five Planck distributions:

$$U(\nu) \sim \sum_k \frac{u_k}{aT_k^4} B(\nu, T_k),$$ (14)

$$T_k \text{ in } \{2.73, 35, 330, 3800, 35000\} \text{ in K},$$ (15)

$$u_k \text{ in } \{0.26, 0.12, 0.025, 0.30, 1.20\} \text{ in eV cm}^{-3}.$$ (16)

The ISRF model is uniform and has no spatial dependence. More details about the derivation of the ISRF model can be found in Appendix C.

2.3.9 Alternative interstellar medium model

The model defined above for interstellar gas, magnetic field, and radiation field is intended as a set of average conditions applicable to the large scales over which most CRs will evolve and will be referred to as the 'average ISM model.' We also used a second set of interstellar conditions that may be more relevant to small scales and the vicinity of some CR sources, where large amounts of gas that fed massive star formation are still present. We assumed that, in such regions, the average neutral gas density is 10 times the galactic average density computed above, while the ionized gas column density becomes $6.18 \times 10^{20}\,\mathrm{H\,cm}^{-2}$, as computed following Paradis et al. (2011), using electron density $n_e = 3.98\,\mathrm{cm}^{-3}$, and an H α intensity of 113.3 Rayleigh corresponding to the limit between 'typical H II regions' and 'very bright H II regions' in the article. The radiation field model is stronger as a result of infrared radiation components scaling linearly with gas column densities. In the absence of any solid estimate, the magnetic field strength in these gas-rich regions is kept at its large-scale average value. This second model will be referred to as the 'gas-rich ISM model' and may be more appropriate for CRs confined to the vicinity of their sources (either because of suppressed diffusion or because of efficient energy losses as in the case of VHE electrons), or to SNRs or PWNe located in rich star-forming regions.

2.3.10 Emission maps

The layout of pion-decay and inverse-Compton interstellar emission over the galaxy is illustrated in Fig. 4, at a reference photon energy of 1 TeV. Hadronic emission is strongly correlated with the distribution of interstellar gas, owing to the long propagation range of CR protons that can fill the entire galactic volume, while leptonic emission is strongly correlated with the assumed distribution of injection sites, because the reach of CR electrons is limited by inverse-Compton and synchrotron losses.

2.4 Emission from the 30 Doradus star-forming region

Over recent years, the question of the behaviour of CRs during the very early stage of interstellar propagation, in the vicinity of their parent sources, has been the focus of numerous theoretical and observational analyses. A recent review of the current status of observations of this stage in the CR life cycle can be found in Tibaldo, Gaggero & Martin (2021).

A rationale behind that interest is that this stage can have consequences on several key observables of the CR phenomenon, for instance the isotopic and spectral properties of the local flux of CRs, or the morphology and spectrum of the large-scale interstellar emission (D'Angelo, Blasi & Amato 2016; D'Angelo et al. 2018). The vicinity of sources is also where evidence for acceleration of galactic CRs to PeV energies and beyond may more likely be found, if the latter are produced and confined only for a short phase in the evolution of (a subset of) the accelerators.

On the theoretical side, CRs freshly released from their accelerator can be expected to influence the transport conditions around it by the same kinetic processes that governed their confinement into the source during acceleration, i.e. self-generation of magnetic turbulence from resonant and non-resonant instabilities (Malkov et al. 2013; Bell et al. 2013). This may lead to enhanced local confinement over several 10 pc scales and 10–100 kyr durations, depending on particle energy and surrounding gas conditions (Nava et al. 2016, 2019; Brahimi, Marcowith & Ptuskin 2020). On the
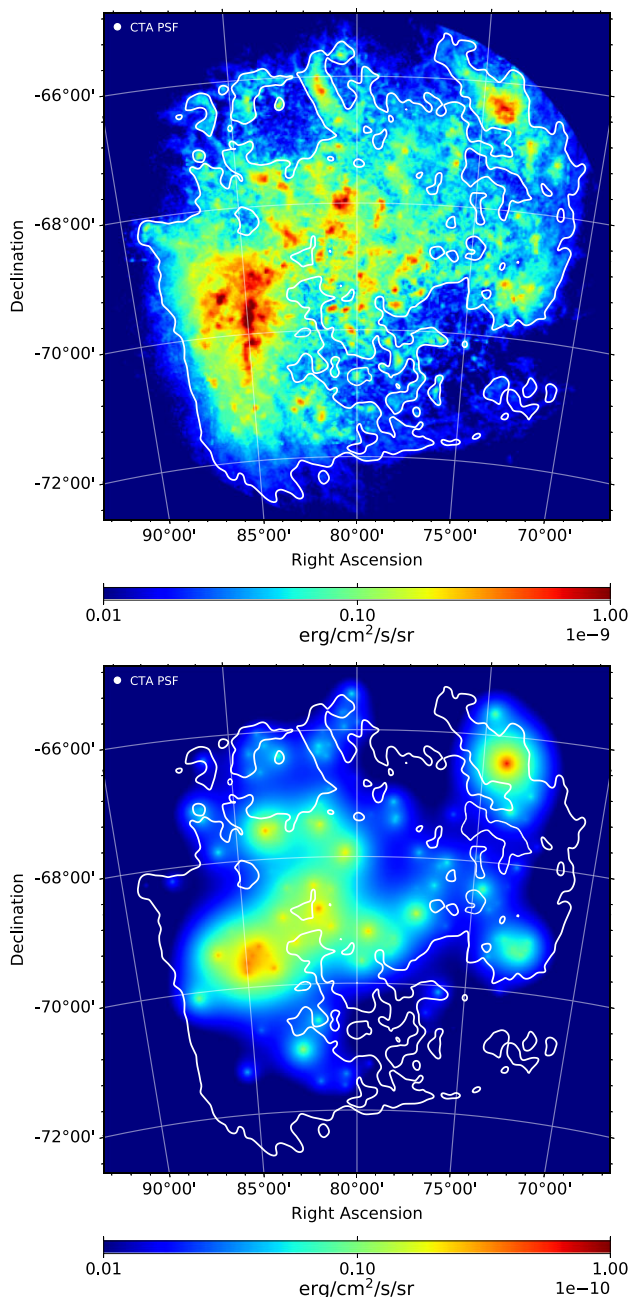
Figure 4. Emission maps in $E^2 \times \mathcal{S}(E)$ at $E = 1\,\mathrm{TeV}$ for large-scale interstellar emission from pion-decay (top panel) and inverse-Compton scattering (bottom panel). Note the different colour scale between the two maps.

observational side, there is growing evidence that specific transport conditions occur in the vicinity of some CR sources, from individual isolated objects such as SNRs, pulsars or PWNe, up to more extended sites such as star-forming regions (SFRs) and SBs.

The interpretation of Galactic observations is challenging because of the need for careful modelling and subtraction of foreground and background interstellar emission along the line of sight to a given source, to properly isolate interstellar emission on small/intermediate scales around it. In that respect, the external viewpoint on the nearby LMC can be a valuable complementary source of information. The

distance to the galaxy, however, restricts our probing of the vicinity of sources to physical scales of the order of $50-100\,\mathrm{pc}$ and above (or $0.06°-0.11°$, compared to the $0.05°-0.06°$ anticipated angular resolution of the southern array at $1\,\mathrm{TeV}$), not to mention the need for sufficient CR injection power to produce a detectable signal. For that reason, we investigated the possibility for the survey to constrain CR transport in the vicinity of the most prominent SFR in the LMC, 30 Doradus. N11 may also constitute an interesting target, although the lack of detectable nonthermal X-ray emission suggests it may be different in nature (Yamaguchi, Sawada & Bamba 2010). A region like 30 Doradus hosts massive stars by the hundreds (Walborn et al. 2014), and is thus potentially able to produce CRs in large quantities; combined with the vast amounts of gas and intense photon fields found in such a location, conditions are ideal for the study of young CRs. In addition to allowing the investigation of how CRs behave close to their sources, major SFRs are also well-motivated candidates for the acceleration of particles to the highest energies, in the PeV range or even beyond (Bykov 2001; Parizot et al. 2004; Aharonian, Yang & de Oña Wilhelmi 2019; Bykov et al. 2020).

We adopted a generic approach to the problem, independent of any specific scenario for CR acceleration in SFRs (e.g. acceleration by individual stars in the cluster, or via repeated shocks, or at the cluster's wind termination shock; see Parizot et al. 2004; Ferrand & Marcowith 2010; Bykov et al. 2018; Morlino et al. 2021). We restricted the physical description of the phenomenon to the following:

(i) Continuous injection of accelerated particles from a point source, with constant power and constant spectral shape assumed to be a power law in momentum with exponential cut-off; in practice, we considered the injection of protons over a duration of 5 Myr, with a hard spectrum with power-law index 2.25 and a cut-off at 1 PeV.

(ii) Spatial diffusion in a medium characterized by a two-zone concentric structure for diffusion properties, with an outer region typical of the average ISM and an inner region where diffusion is suppressed relative to the ISM; the ISM diffusion coefficient has the form introduced in Section 2.3, and we considered diffusion suppression as an overall reduction by factors ranging from a few to a few hundred, within a distance of 100 pc from the source.

(iii) Alongside with spatial diffusion, particles experience homogenous energy losses over the entire volume explored, both the inner and outer diffusion regions; for protons, these consist of hadronic interactions losses for which we adopted the average gas density introduced in Section 2.3 (limited variations around that value have little influence on the final outcome as the emission model is eventually corrected for the actual gas distribution around a given source; see below).

The above assumptions allow to compute a three-dimensional emissivity kernel that we integrate along lines of sight over the typical thickness of the gas disc, and then renormalize in each direction by the actual gas distribution towards a given region (similarly to what was done for the large-scale pion-decay emission model in Section 2.3), finally yielding an intensity distribution. Fig. 5 shows radial intensity profiles for different values of the suppression factor, and before correction of the intensity for any actual gas distribution. Fig. 6 shows the resulting intensity distribution for the 30 Doradus region, after correction for the actual gas distribution and for three cases of diffusion suppression.

With such a description of the problem, we restrict the discussion to that of knowing under which conditions a given SFR can be detected and identified as such. Specifically, we want to determine the
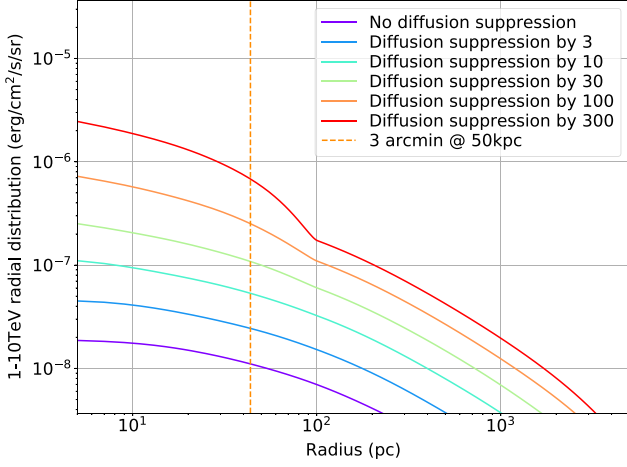
Figure 5. Radial 1–10 TeV intensity profiles for pion-decay emission resulting from CR protons continuously injected by a point-source over 5 Myr and diffusing away in a medium characterized by two zones: an outer region >100 pc typical of the average ISM and an inner region ≤100 pc where diffusion is suppressed relative to the ISM. The profiles shown here correspond to emission from a region filled with a homogenous gas density $n_H = 1.93\,\mathrm{H\,cm^{-3}}$, and the injection luminosity is arbitrarily set at $10^{40}\,\mathrm{erg\,s^{-1}}$. When used in specific cases, for instance the 30 Doradus region, the intensity distribution is corrected for the actual gas content of the region (see the text).

requirements in terms of injection power and diffusion suppression for the latter two objectives to be fulfilled (the spectral index of the injection spectrum is also a relevant parameter but we already assumed as reference scenario a rather low value). Since such parameters are essentially unknown, it is not possible to incorporate all SFRs in our global emission model for the galaxy in a coherent and justified way; instead, we will present below, in the results section, a parametric study of the prospects for the detection of 30 Doradus in the survey.

2.5 Dark matter

We assume that DM is made of stable particles, which may however annihilate with each other, producing a shower of standard model particles. This in turn would lead to either direct or secondary production of gamma–rays, at energies of a few GeV and above, thus making them potentially detectable with CTA (and other gamma-ray telescopes). We address the reader to the vast literature existing on the DM candidates and models complying with the many requirements and characteristics (e.g. Bertone 2010; Boyarsky, Ruchayskiy & Shaposhnikov 2009; Bœhm & Fayet 2004; Hu, Barkana & Gruzinov 2000; Blais, Kiefer & Polarski 2002, and references therein), adopting here for our purposes the generic definition of Weakly Interacting Massive Particles (WIMPs).

In the WIMPs DM scenario, the gamma-ray flux produced by the interaction follows:

$$\frac{d\Phi}{dE} = \frac{1}{8\pi} \frac{\langle \sigma v \rangle}{m_\chi^2} \frac{dN_\gamma}{dE} \int_{\Delta\Omega} \int_{\mathrm{l.o.s}} \rho^2(\ell)\, d\ell \qquad (17)$$

where $\frac{d\Phi}{dE}$ is the gamma-ray flux produced, $\langle \sigma v \rangle$ is the DM annihilation velocity-averaged cross-section, m_χ is the mass of the DM candidate, $\frac{dN_\gamma}{dE}$ is the gamma-ray spectrum produced by one single annihilation event (two DM particles annihilating into a shower of standard model particles), and $\rho(l)$ is the DM density distribution
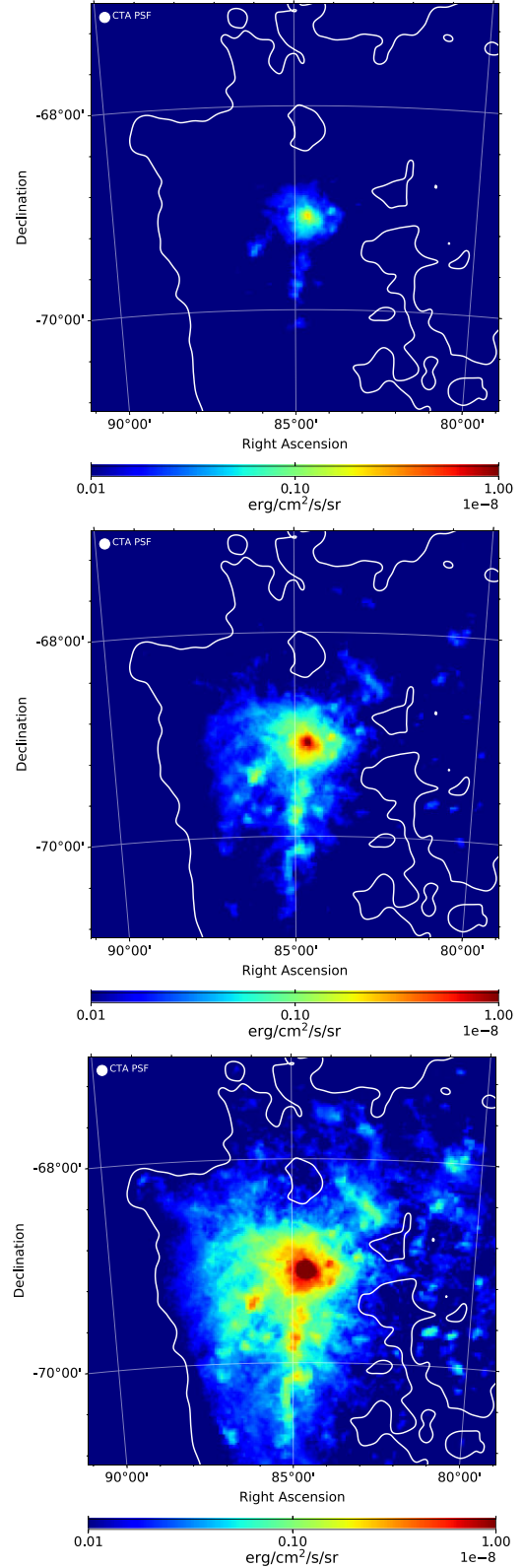
Figure 6. Intensity maps at 1 TeV for pion-decay emission from the 30 Doradus star-forming region, under three assumptions for the suppression of spatial diffusion within 100 pc of the central source: reduction by a factor of 3, 30, and 300 (from top to bottom panel, respectively).

Table 2. Benchmark DM profiles adopted in this work, using parameters extracted from table II in Buckley et al. (2015), keeping the same nomenclature. The J-factor, in the last column, is integrated over a field of view of $10°$.

Profile	α	β	γ	r_s (kpc)	ρ_0 ($M_\odot$ kpc^{-3})	J-factor (GeV^2 cm^{-5})
iso-min	2	2	0	2.4	2.9×10^7	5.96×10^{20}
iso-mean	2	2	0	2.4	3.7×10^7	9.71×10^{20}
iso-max	2	2	0	2.0	6.2×10^7	1.67×10^{21}
nfw-min	1	3	1	12.6	1.8×10^6	6.52×10^{20}
nfw-mean	1	3	1	12.6	2.6×10^6	1.36×10^{21}
nfw-max	1	3	1	17.6	2.5×10^6	2.85×10^{21}

within the target, with l being a generic variable representing position along the line of sight. The latter integral term is also known as 'J-Factor', and that is how it will be referred to from now on. Our goal is to test different DM models according to the parameters of equation (17). Each DM model will be included in the LMC emission model as a new diffuse source, and the potential of CTA to detect a source of this nature will be assessed.

It is important to stress that, according to the custom in high-energy DM searches with gamma-rays, we will treat both $\langle \sigma v \rangle$ and m_χ as free parameters, and adopt 'single annihilation' spectra assuming at each time the branching ratio of the interaction is one, namely that the entire annihilation takes place in the specific channel, then showing the results for different channels in order to bracket the possible outcome. Model-specific analyses relating $\langle \sigma v \rangle$ and m_χ to the parameters of the particle theory (Lagrangian) can be performed separately, and are outside the scope of this study.

The DM distribution of the LMC can be inferred by the gravitational structure of its disk, following the well-known 'rotation curve method'. This allows to infer the DM component of the gravitational potential for disk galaxies in an extended mass range, once a suitable set of tracers for the circular motion of the disk – at different galactocentric distances – and a good understanding of the visible component are available. DM is usually assumed to be spherically distributed, as there is little evidence for sizable departure from symmetry in hydrodynamical cosmological numerical simulations of galaxy formation and evolution, and we kept that assumption here. In order to be consistent with previous literature and allow direct comparison, while at the same time performing an independent analysis, we have closely followed the results of Buckley et al. (2015), which in turn adopt the data available in the literature and presented in Kim et al. (1998), Luks & Rohlfs (1992), and van der Marel & Kallivayalil (2014). We have adopted a Hernquist-Zhao six-parameter profile (Zhao 1996):

$$\rho(r) = \frac{\rho_0}{\left(\frac{r}{r_s}\right)^\gamma \left[1 + \left(\frac{r}{r_s}\right)^\alpha\right]^{\frac{\beta-\gamma}{\alpha}}} \tag{18}$$

centred at $(\alpha_{\mathrm{J2000}}, \delta_{\mathrm{J2000}}) = (80.0°, -69.0°)$, where r_s is the scale radius and ρ_0 is the characteristic density, both of which can be derived from the rotation curves of the LMC. These last two parameters are the ones that most affect the total mass of the specific DM halo, and therefore are most constrained by the observations of the LMC baryonic mass and dynamics mentioned above. When $\alpha = 1$ and $\beta = 3$, the Hernquist–Zhao profile is called a generalized NFW profile (gNFW) with flexible inner DM density slope γ. Setting $(\alpha, \beta, \gamma) = (1, 3, 1)$, we retrieve the Navarro–Frenk–White (NFW) profile (Navarro, Frenk & White 1996), while an isothermal profile is obtained setting $(\alpha, \beta, \gamma) = (2, 2, 0)$. Variations of these two profiles have been tested, with their parameters shown in Table 2 and plotted
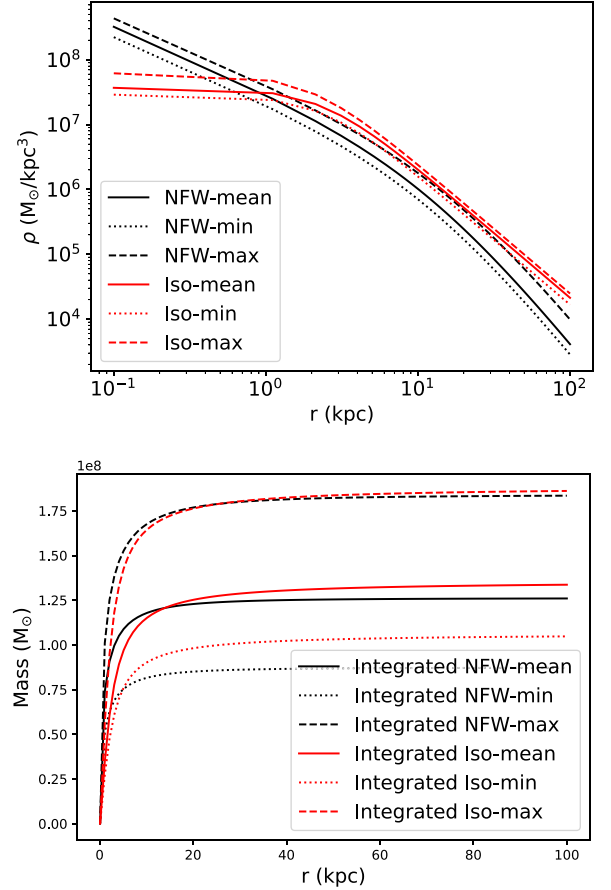

Figure 7. DM benchmark density profiles and integrated mass as a function of radius (top and bottom panels, respectively), computed using the parameters in Table 2.

in Fig. 7. These variations maximize and minimize the DM density, but are still compatible with the rotation curves.

For the computation of the density profiles and their corresponding J-factors, we have used the public code CLUMPY, a code for gamma-ray and neutrino signals from DM structures (Charbonnier, Combet & Maurin 2012; Bonnivard et al. 2016; Hütten, Combet & Maurin 2019). We have generated two-dimensional sky maps of the J-factor in equation (17), with the parameters listed in Table 2, in a field of view of $10°$. The J-Factor integrated in the $10°$ field of view, given in the last column of the table, was also calculated with CLUMPY. These sky maps correspond to the spatial part of the model and are combined with the gamma-ray spectra of different annihilation channels in the final DM emission model.

For the spectral part of the DM emission model (the dN_γ / dE term in equation 17), the recipes from Cirelli et al. (2011) were used, where the energy spectra of gamma-rays produced by different DM annihilation channels are provided. We study the $b\bar{b}$, W^+W^-, $\tau^+\tau^-$, and $\mu^+\mu^-$ channels, including electro-weak corrections as computed in Ciafaloni et al. (2011).

2.6 Emission model validation

The consistency of our emission model with our present-day knowledge of the LMC is checked against the following criteria:

(i) The total predicted interstellar gamma-ray emission should not exceed the integrated flux measured at 10 GeV. In Ackermann et al. (2015), 0.1–100 GeV extended emission was decomposed into a large-scale emission seemingly correlated with the gas disc and a handful of additional components of unclear nature. We therefore assumed that the interstellar emission at 10 GeV predicted by our model should not exceed the sum of all extended emission components found in Ackermann et al. (2015), which corresponds to an upper limit in flux density $F(E)$ at 10 GeV of $E^2 \times F(E) = 2 \times 10^{-11}\,\mathrm{erg\,cm^{-2}\,s^{-1}}$.

(ii) Gamma-ray emission on small scales ≤ 50 pc, either from individual sources or fine structures in interstellar emission, should not exceed upper limits on point-like emission in the 1–10 GeV and 1–10 TeV bands. As typical values, we used upper limits on SN 1987A derived in Ackermann et al. (2015) and Abramowski et al. (2015) and corresponding to $5.4 \times 10^{-13}\,\mathrm{erg\,cm^{-2}\,s^{-1}}$ at 10 GeV and $1.2 \times 10^{-13}\,\mathrm{erg\,cm^{-2}\,s^{-1}}$ at 1 TeV. Constraints have certainly improved since these studies due to increased exposure, but by a factor likely ≤ 2.

(iii) The total predicted interstellar radio synchrotron emission should not exceed the integrated flux measured at 1.4 GHz. Synchrotron emission at frequency 1.4 GHz arises mostly from 5 GeV CR leptons in the assumed mean $4\,\mu$G interstellar magnetic field (Blumenthal & Gould 1970), which are not those contributing to the gamma-ray signal in the CTA band, but such a check guarantees some continuity and consistency in leptonic emission over a wide range of energies. The total radio flux at 1.4 GHz measured from ATCA + Parkes observations is 426 Jy (Hughes et al. 2007). This includes an estimated 50 Jy from background point sources and ≥ 20 per cent from thermal bremsstrahlung from ionized gas. The total synchrotron emission therefore has an intensity ≤ 291 Jy at most. We checked that the assumptions made in computing the large-scale interstellar emission of leptonic origin lead to a total interstellar synchrotron intensity below this limit.

In practice, with the assumptions introduced in Section 2, the three criteria listed above are fulfilled and the comparison confirms that the various components of our model are well calibrated.

The criterion on the total interstellar gamma-ray emission is the most constraining since our baseline model predicts a 10 GeV flux that nearly saturates the maximum acceptable level. The Fermi-LAT measurement is thus very informative already and will restrict the allowed space for some parameters: for instance, it is not possible to strongly increase the CR proton injection rate while keeping all other parameters untouched. Actually, for given CR injection and spatial diffusion indices, the luminosity of the large-scale pion-decay component is set to first order by the product of injection rate, gas mass, and the inverse of spatial diffusion normalization, and none of these parameters is known to high accuracy (the most constrained being the gas mass, with 30 per cent uncertainty, and the least constrained the diffusion coefficient).

The criterion on small-scale, almost point-like, gamma-ray emission is also fulfilled. Small-scale emission peaks in the pion-decay model are about 4 times below the 10 GeV limit, which again shows that Fermi-LAT measurements are already constraining, and about 50 times below the 1 TeV limit. Small-scale emission peaks in the inverse-Compton model are more than two orders of magnitude below the 10 GeV and 1 TeV limits, in the baseline model relying on the average ISM model. Using the gas-rich ISM model instead, which comes with a higher ISRF and may be more appropriate for regions harbouring rich stellar populations, leads to higher emission maxima by a factor of 2–3, while using a harder injection spectrum
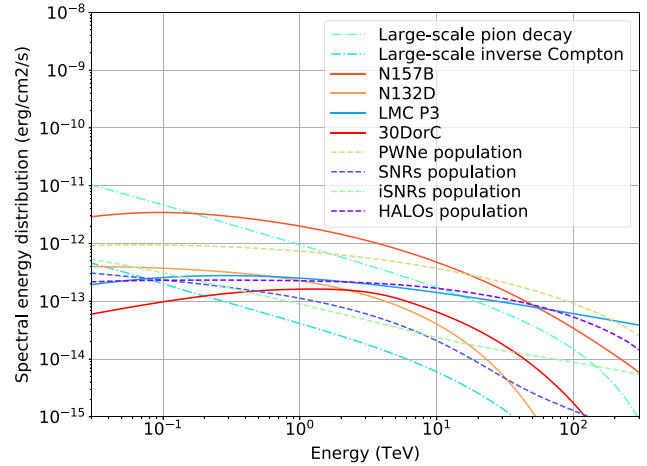

Figure 8. Spectral energy distribution of all emission components in our model (except for possible emission from dark matter and CRs in the vicinity of SFRs): the four currently known TeV sources (SNR N 132D, PWN N157D, 30 Doradus C, and binary LMC P3), large-scale interstellar emission from pion-decay and inverse-Compton scattering, and total emission from the SNRs, iSNRs, PWNe, and pulsar haloes populations.

for CR electrons, with a power-law index of 2.25, increases the small-scale emission peaks at 1 TeV by a factor of 20, which still remains largely below the current constraints. Last, in our realization of the source populations model, apart from a couple of extreme objects that would already be detectable with H.E.S.S., which nicely matches the current census of gamma-ray sources in the LMC, the populations of SNRs, iSNRs, PWNe, and pulsar haloes reach emission levels that are at most 2–3 times below the 10 GeV and 1 TeV limits.

The predicted 1.4 GHz synchrotron intensity in our model is 53 Jy, which is far below the limit defined above and may suggest our model would significantly underpredict the actual level of synchrotron emission. Our model assumes that 1 per cent of the total CR injection power is in the form of primary electrons, in agreement with estimates for the Galaxy (Strong et al. 2010), so increasing the predicted interstellar synchrotron flux would have to be done by acting on other parameters. Reducing the diffusion coefficient normalization or increasing the injection power are not options because of constraints on the pion decay component, which saturates the allowed level at 10 GeV (although a smaller diffusion coefficient would be allowed if the diffusion region has a finite size; see the comment in Appendix B). Instead, a slightly higher interstellar magnetic field would alleviate the discrepancy. Taking into account the contribution from secondary electrons would also reduce the gap, although by no more than 30 per cent according to the estimate of the contribution of secondaries presented below. On the other hand, the measured flux includes more than purely interstellar emission, for instance contribution from a population of unresolved discrete SNRs, or thermal emission from ionized gas, if it contributes more than 20 per cent of the total radio flux.

The integrated emission spectra for all components discussed above are shown in Fig. 8, except for possible emission from 30 Doradus. PWN N 157B dominates the galaxy's emission over most of the 0.1−100 TeV range; as a confirmation of its outlier nature, it is two to three times more luminous at 1 TeV than all PWNe in our synthetic population taken together. Similarly, N 132D is as bright at 1 TeV as the rest of the SNRs population, including interacting ones. The second most luminous component overall is large-scale interstellar pion-decay emission up to about 1 TeV,

and the mock PWNe population at higher energies. Large-scale inverse-Compton interstellar emission appears as a comparatively subdominant component, in agreement with Persic & Rephaeli (2022).

Secondary leptons from charged pions are not included in our model. The magnitude of their contribution can be estimated from the luminosity of the pion-decay gamma-ray component, which is $3.7 \times 10^{37} \, \text{erg s}^{-1}$ above 1 GeV. In that range, the spectrum of secondary leptons is very similar to that of gamma rays, albeit at least two times lower (Kelner, Aharonian & Bugayov 2006). The spectrum of secondary leptons at injection would thus be close to a power law with index 2.7 and luminosity above 1 GeV of $<1.9 \times 10^{37} \, \text{erg s}^{-1}$. Compared to the injection spectrum for primary electrons, a power law with index 2.65 and luminosity above 1 GeV of $6.5 \times 10^{37} \, \text{erg s}^{-1}$, this suggests that secondaries would be a correction to our model at the level of <30 per cent in the energy range of interest.

3 SURVEY SIMULATION AND ANALYSIS

3.1 Observation simulations

Observation simulation in this work means the generation of high-level data, ready for scientific analysis. In practice, it produces lists of events such as those that passed Cherenkov light detection, shower reconstruction, and gamma-hadron discrimination. Photon and background events are randomly generated from a model for celestial emission in the region of interest, a description of the instrument's performances, and a definition of the observations. The latter is addressed in the next section and sets the number, positions, and durations of all pointings in the survey. Due to the availability of instrument responses for a limited subset of observing conditions and in the absence of realistic scheduling constraints, this is done under simplifying assumptions.

The performances of the CTA observatory are defined in instrument response functions and background rates. The former describes how an incident gamma ray is converted into a measured event and is factorized into three terms for effective area, point spread function, and energy dispersion. The latter defines how events that are not gamma rays in origin are generated over the data space as a function of observing conditions. In this work, we used response *South_z40_50h* of the *prod5-v0.1* release,[5] valid over 50 GeV–200 TeV and appropriate for observations at 40° zenith angle averaged over azimuth angles (the LMC will be seen at best at ~46° elevation from the southern site). This is a description of the southern array that will be built during an initial construction phase of the project and will consist of 14 medium-sized telescopes and 37 small-sized telescopes. The project may later evolve towards a final full-scope configuration comprising 4 large-sized telescopes, 25 medium-sized telescopes and 70 small-sized telescopes on the southern site, but we did not investigate the prospects for such a configuration.

The emission model $\mathcal{S}$ for the LMC was introduced in previous sections and will be convolved with the instrument response functions $\mathcal{R}$ for given observing conditions. In the particular case of this work, we consider mainly sources that are steady (on human time scales). The only exception to this would be the gamma-ray binary LMC P3, which has its emission modulated

by orbital motion, but we do not focus on that particular aspect and assumed its phase-averaged emission to be constant. We therefore leave aside the general time dependence of the signals and the biases introduced by the instrument in photon arrival time measurements.

In the field of a pointing defined by parameters $\mathbf{p}$, the expected event measurement rates at a given position in the sky $\mathbf{r}$ and reconstructed energy E can be split into background events $\mathcal{M}^B$ and gamma-ray events $\mathcal{M}^S$:

$$\mathcal{M}_p^B(\mathbf{r}, E, \boldsymbol{\theta_B}) = \mathcal{B}(\mathbf{r}, E | \boldsymbol{\theta_B}, \mathbf{p}), \tag{19}$$

$$\mathcal{M}_p^S(\mathbf{r}, E, \theta_S) = \iint \mathcal{S}(\mathbf{r_0}, E_0 | \boldsymbol{\theta_S}) \mathcal{R}(\mathbf{r}, E | \mathbf{r_0}, E_0, \mathbf{p}) \, \mathrm{d}E_0 \, \mathrm{d}\mathbf{r_0}, \tag{20}$$

$$\mathcal{R}(\mathbf{r}, E | \mathbf{r_0}, E_0, \mathbf{p}) = \mathcal{A}(\mathbf{r_0}, E_0, \mathbf{p}) \mathcal{P}(\mathbf{r} | \mathbf{r_0}, E_0, \mathbf{p}) \mathcal{D}(E | \mathbf{r_0}, E_0, \mathbf{p}). \tag{21}$$

Lists of events with reconstructed energy, direction, and arrival time are randomly generated for each pointing from the above expected measurement rates.

The dependence of background rate $\mathcal{B}$, effective area $\mathcal{A}$, point spread function $\mathcal{P}$, and energy dispersion $\mathcal{D}$ on vector $\mathbf{p}$ encapsulates the general dependence of the instrument response on observation conditions (e.g. detector centre and orientation on the sky, pointing zenith and azimuth). In this work, however, we will neglect energy dispersion. Vectors θ_S and θ_B hold the various spectral and spatial parameters on which celestial and background models $\mathcal{S}$ and $\mathcal{B}$ depend. In the following, we will denote $\theta_S^{\mathbf{T}}$ and $\theta_B^{\mathbf{T}}$ the true values of these parameters, and $\tilde{\theta}_S$ and $\tilde{\theta}_B$ their estimated values (from the maximum likelihood estimator, see below).

3.2 Pointing strategy

The LMC is slightly larger than the field of view of CTA, so the survey will involve a number of overlapping observations to encompass the full galaxy. Because of the diversity of targets in the LMC, the optimal pointing layout is not obvious: concentrating the exposure over a smaller patch of the sky will maximize sensitivity to point-like sources in the innermost regions (e.g. PWNe, SNRs, and pulsar haloes); conversely, spreading the exposure well beyond the outskirts of the LMC will include nearly empty fields and provide more contrast for the detection of very extended sources with a size comparable to the field of view of the instrument (e.g. interstellar emission on galactic scales).

To ensure uniformity of the exposure at all energies, we aimed at a pointing pattern with a large number of short-duration pointings equally spaced from one another. We considered a layout in which pointings are distributed along concentric hexagons and equidistant from their closest neighbours. We searched for the optimal pointing spacing by evaluating its impact on the sensitivity to several representative source morphologies and positions in the survey field: (i) a point source at the position of SN 1987A, i.e. in central regions; (ii) a point source at the position of star-forming region N11, i.e. on the edge of the galaxy; (iii) interstellar pion-decay emission with the morphology computed in our emission model.

We compared different spreads of the exposure, parametrized as the maximum extent of the pattern (i.e. full width of outermost hexagon) and varied from 4° to 10°. Sensitivity curves for the three test sources listed above are presented in Fig. 9 and, in the case of point sources, compared to spectra of the Crab nebula rescaled by factors of 0.01 and 0.001 (Abeysekara et al. 2019), and to the LAT
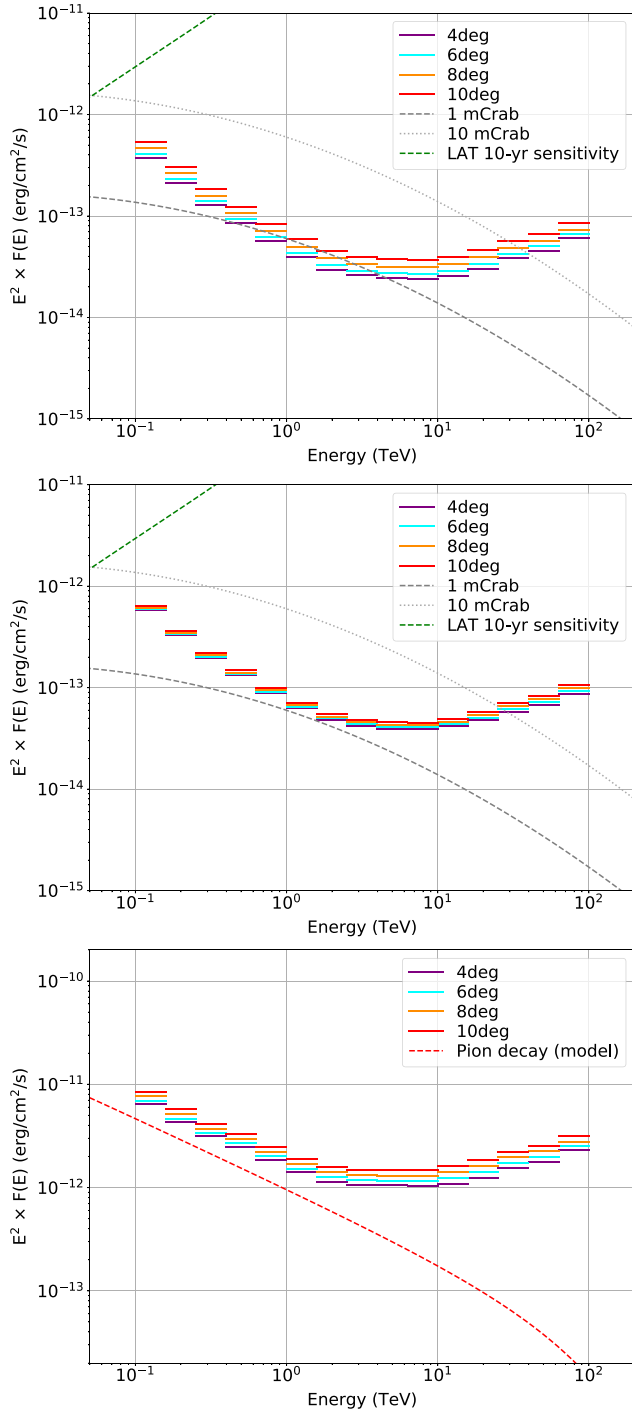
Figure 9. Sensitivity curves for point sources at the positions of SN 1987A and N11 and for our large-scale pion-decay emission model (from top to bottom panel, respectively), as a function of the pointing pattern. The latter consists of a large number of equally spaced pointings arranged along concentric hexagons, and we compared different spreads of the exposure, from $4°$ to $10°$. Overlaid as reference for the point sources are spectra of the Crab nebula rescaled by factors of 0.01 and 0.001, and the LAT P8R3 10-yr sensitivity for Galactic coordinates (l,b) = ($120°$,$45°$).

P8R3 10-yr sensitivity[6] for Galactic coordinates (l,b) = ($120°$,$45°$). The meaning and computation of sensitivity curves will be defined below but we emphasize that we checked that some parameters of the data analysis have no impact on the conclusions reported here (in particular the size of the region of interest used in the binned analysis).

As could be anticipated, sensitivity to a centrally located point-like source improves as exposure becomes more concentrated, by a factor <2 that is approximately constant over the energy band. The sensitivity gain seems however to flatten as the pattern size drops below $6°$. Sensitivity to a diffuse source such as our large-scale pion-decay emission model shows a similar behaviour, although less pronounced at low energies <1 TeV. There does not seem to be any benefit of adding nearly empty fields to the survey, probably because interstellar emission as modeled here has sufficient structure on small angular scales that it can be easily disentangled from instrumental background. In contrast to the two previous sources, sensitivity to a point source located in the outskirts of the galaxy is nearly insensitive to the exposure spread, with a maximum effect at the level of 30 per cent at 100 TeV. This likely results from exposure spread being compensated by a higher number of pointings having their centers close to the boundaries of the galaxy.

We eventually adopted a pointing pattern consisting of 331 pointings of 3698 s each, equally spaced along 10 concentric hexagons centred on (α_{J2000}, δ_{J2000}) = ($80.0°$, $-69.0°$). This corresponds to a spacing between adjacent pointings of $0.3°$ and to a maximum extent of $6°$, as illustrated in Fig. 10. In a given pointing, sensitivity typically drops beyond an off-axis angle of $3°-4°$, depending on energy in the $0.1-10$ TeV range, which ensures a broad enough coverage of the galaxy and its outskirts. Although a smaller pointing spacing would have provided a slightly better sensitivity to all emission components tested here, keeping a wide enough survey footprint covering the galaxy at large is key for making discoveries.

3.3 Simulated data analysis

Source characterization is achieved by maximum likelihood estimation of the parameters of a model for some region of interest in the simulated observations. In this work, we used a likelihood analysis for binned data and Poisson statistics, as implemented in the ctools package (Knödlseder et al. 2016), and we stacked data such that events from all pointings are added and instrument response functions are averaged over all observations (see 'Combining observations' in ctools user manual). The applicability of such an approach was demonstrated in Knödlseder et al. (2019) on real data from the H.E.S.S. experiment.

The region of interest is typically a $8° \times 8°$ square centered on (α_{J2000}, δ_{J2000}) = ($80.0°$, $-69.0°$) and aligned on equatorial coordinates, except for DM analyses where a $10° \times 10°$ region was used to fully capture the very extended signals considered. Within this area, events are binned in $0.02° \times 0.02°$ spatial pixels and 0.1 dex spectral intervals spanning 100 GeV to 100 TeV. The high lower energy bound compared to the full range that should be accessible to CTA is warranted by the rapid degradation of

---

[6]https://www.slac.stanford.edu/exp/glast/groups/canda/lat_Performance.htm
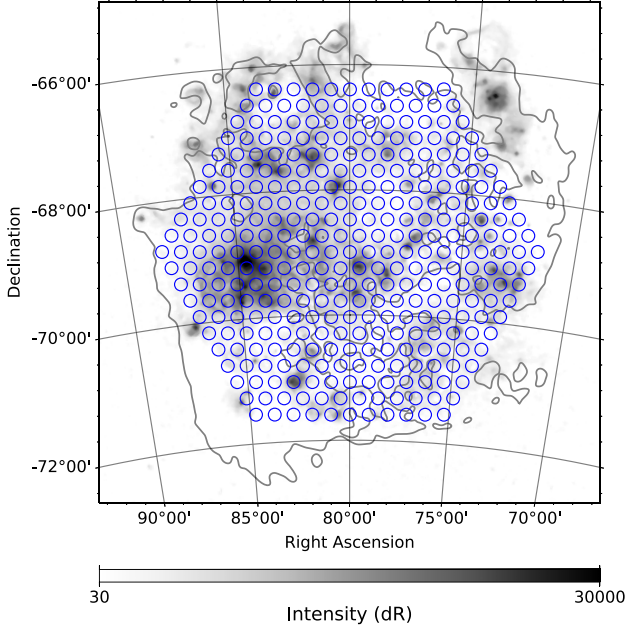
Figure 10. Pointing pattern adopted in the study. Each blue circle corresponds to the centre of one among 331 equally spaced pointings of nearly 1h each, arranged along 10 concentric hexagons centered on (α_{J2000}, δ_{J2000}) = (80.0°, −69.0°). The whole pattern spans 6°, and each pointing has an effective gamma-ray field of view of 3°−4° in off-axis radius in the 0.1−10 TeV range. For comparison, the anticipated angular resolution of the southern array at 1 TeV is about 0.05°−0.06°.

performance $<100\,\text{GeV}$ for zenith angles $>40°$ at which the LMC will be observed.

The logarithm of the likelihood is computed from measured number of counts in the data cube D and predicted number of counts in the model cube M:

$$D = \{n_{i,j}\}, M = \{\mu_{i,j}\} \tag{22}$$

$$\ln \mathcal{L}(\mathcal{M}^B, \mathcal{M}^S|D) = \sum_{i,j} n_{i,j} \ln \mu_{i,j} - \mu_{i,j} \tag{23}$$

In the above equations, i is the index on spectral intervals and j the index on spatial pixels. The dependence of the likelihood on the parameters and functional form of the models for instrumental background and celestial emission is expressed as a dependence on model functions $\mathcal{M}^B$ and $\mathcal{M}^S$.

For a given set of observations, predicted model counts are obtained by sampling $\mathcal{M}^B$ and $\mathcal{M}^S$ at bin centres ($\boldsymbol{r}_j$, E_i), multiplying by bin volume $\Delta\Omega_j\Delta E_i$ and pointing livetime $\Delta T_{\mathbf{p}}$, and finally summing over all pointings:

$$\mu_{i,j} = \mu_{i,j}^B + \mu_{i,j}^S, \tag{24}$$

$$\mu_{i,j} = \sum_{\boldsymbol{p}} (\mathcal{M}_{\boldsymbol{p}}^B(\boldsymbol{r}_j, E_i, \boldsymbol{\theta_B}) + \mathcal{M}_{\boldsymbol{p}}^S(\boldsymbol{r}_j, E_i, \boldsymbol{\theta_S})) \times \Delta\Omega_j \times \Delta E_i \times \Delta T_{\boldsymbol{p}}. \tag{25}$$

In the framework of this analysis, models are factorized into two terms $\mathcal{M} = \mathcal{H} \times \mathcal{F}$, with $\mathcal{H}$ describing the (possibly energy-dependent) morphology and $\mathcal{F}$ defining the spectral shape.

Optimum parameters $\tilde{\theta}_{\mathbf{S}}$ and $\tilde{\theta}_{\mathbf{B}}$ are searched for iteratively such that the likelihood is maximized:

$$\ln \mathcal{L}(\tilde{\mathcal{M}}^B, \tilde{\mathcal{M}}^S|D) = \ln \mathcal{L}(\mathcal{M}^B(\tilde{\theta}_{\mathbf{B}}), \mathcal{M}^S(\tilde{\theta}_{\mathbf{S}})|D). \tag{26}$$

The significance of a source component or source parameter in the model is assessed in terms of the test statistic (TS):

$$\text{TS} = 2\ln \frac{\mathcal{L}(\tilde{\mathcal{M}}^B, \tilde{\mathcal{M}}^S_{\text{test}}|D)}{\mathcal{L}(\tilde{\mathcal{M}}^B, \tilde{\mathcal{M}}^S_{\text{null}}|D)}, \tag{27}$$

where $\tilde{\mathcal{M}}^S_{\text{test}}$ is the optimum model including the additional tested source component or parameter, for instance an additional source component with non-zero normalization or a cut-off parameter in the spectrum of a component, and $\tilde{\mathcal{M}}^S_{\text{null}}$ is the optimum model without it (Cash 1979). A value TS > 25 is adopted as a criterion for significant detection of a source (either over the full energy range or within narrower intervals as in the case of sensitivity curves). In practice, the fitting of model parameters and calculation of the significance of sources was done using the *ctlike* function from ctools.

For low-significance source components, we calculated flux upper limits, usually in narrow energy bins. Keeping the spatial and spectral shape parameters of the component of interest fixed, and varying only its normalization, Wilks' theorem (Wilks 1938) states that the TS function asymptotically approaches a χ^2-distribution with one degree of freedom under the null hypothesis. We therefore adopted as upper limit the flux normalization such that TS = 2.71, which corresponds to a 95 per cent Confidence Level (CL) upper limit. The calculation of flux upper limits was performed with function *ctulimit* from ctools and used in particular to set constraints on the DM annihilation cross section $\langle \sigma v \rangle$, as described in Section 2.5.

In the analyses presented below, we frequently made use of so-called *Asimov* data sets. An *Asimov* data set (Cowan et al. 2011) is a representative data set in which the number of counts in a given bin in the data space corresponds exactly to the model expectation, without any statistical fluctuation. When fitting a model to such a data set, the true values of the model parameters are perfectly recovered, if the model used for simulation and fitting is the same. The main interest of such an approach is to get mean results for source significance and detection upper limits, without the need for a large number of realizations of simulated data (which in the present case is quite computer-intensive as it would require simulating the full 340 h of observations about 1000 times or more for each analysis set-up).

4 DETECTION PROSPECTS

4.1 Sensitivities

We begin by presenting the survey sensitivity to some of the components in our emission model. Sensitivity was computed in independent energy bins, typically 5 per decade, as the source flux yielding on average a detection with TS = 25 in each bin. It depends strongly on source morphology but also on position in the field, first because the exposure is slightly uneven and second because other neighbouring or overlapping emission components may increase the detection threshold. Yet, the sensitivity curves presented below were computed for each source independently, considering only the instrumental background as other source component and not the full emission model. In most cases, this is partly justified by the fact that diffuse interstellar components in our baseline emission model are too weak to seriously alter sensitivity. In specific regions, however, source confusion may be a problem and limit our ability to detect and/or separate weak source components. The data points for the sensitivities to the emission components discussed below are provided in Table 3 for convenience and may be used in future assessments of the detectability of some sources for specific models (e.g. SN 1987A).

Table 3. Sensitivities to several emission components considered in this work, expressed in $E^2 \times F(E)$ with the threshold flux density $F(E)$ defined in Section 4.1: in columns four to seven, sensitivities to point sources at the positions of currently known VHE sources in the LMC; in the eighth column, sensitivity to a point source at the position of SN 1987A; in the last two columns, sensitivities to extended emission templates for large-scale pion-decay and inverse-Compton radiation from the ISM. The sensitivities were computed in each energy bin as the flux yielding a detection with TS = 25 on average, for a binned and stacked analysis over a $8° \times 8°$ region of interest centered on $(\alpha_{J2000}, \delta_{J2000}) = (80.0, -69.0)$.

Bin	Lower bound (TeV)	Upper bound (TeV)	N 157B	N 132D	30 Dor C	LMC-P3 (erg cm^{-2} s^{-1})	SN 1987A	LMC-IC	LMC-Pion
1	0.100	0.158	4.137e−13	3.803e−13	3.968e−13	4.387e−13	4.103e−13	9.193e−12	6.962e−12
2	0.158	0.251	2.356e−13	2.152e−13	2.261e−13	2.505e−13	2.322e−13	5.772e−12	4.664e−12
3	0.251	0.398	1.421e−13	1.297e−13	1.370e−13	1.515e−13	1.397e−13	3.986e−12	3.397e−12
4	0.398	0.631	9.498e−14	8.671e−14	9.179e−14	1.015e−13	9.336e−14	2.941e−12	2.675e−12
5	0.631	1.000	6.297e−14	5.732e−14	6.084e−14	6.759e−14	6.185e−14	2.052e−12	2.001e−12
6	1.000	1.585	4.419e−14	4.022e−14	4.290e−14	4.769e−14	4.329e−14	1.468e−12	1.527e−12
7	1.585	2.512	3.370e−14	3.070e−14	3.282e−14	3.648e−14	3.294e−14	1.135e−12	1.256e−12
8	2.512	3.981	2.961e−14	2.703e−14	2.908e−14	3.216e−14	2.898e−14	9.983e−13	1.173e−12
9	3.981	6.310	2.796e−14	2.563e−14	2.744e−14	3.030e−14	2.743e−14	9.277e−13	1.161e−12
10	6.310	10.000	2.729e−14	2.478e−14	2.665e−14	2.970e−14	2.682e−14	8.583e−13	1.149e−12
11	10.000	15.849	2.942e−14	2.647e−14	2.869e−14	3.207e−14	2.899e−14	8.546e−13	1.229e−12
12	15.849	25.119	3.418e−14	3.034e−14	3.326e−14	3.726e−14	3.396e−14	9.046e−13	1.413e−12
13	25.119	39.811	4.256e−14	3.750e−14	4.129e−14	4.608e−14	4.259e−14	1.021e−12	1.744e−2
14	39.811	63.096	4.999e−14	4.176e−14	4.793e−14	5.419e−14	5.022e−14	1.049e−12	1.993e−12
15	63.096	100.000	6.492e−14	4.992e−14	6.139e−14	7.047e−14	6.610e−14	1.138e−12	2.521e−12
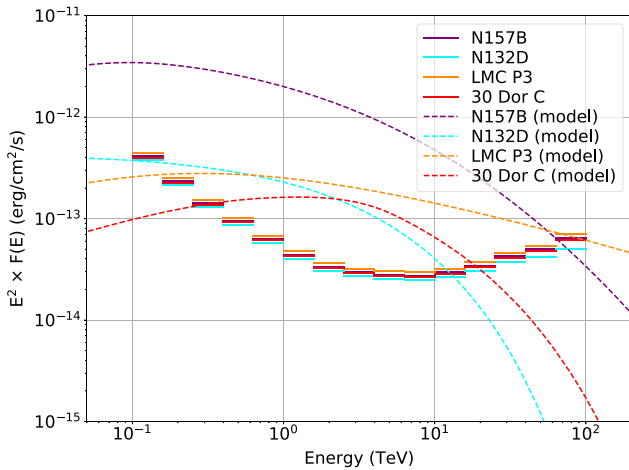
Figure 11. Sensitivity of the survey to point sources at the positions of the four VHE objects currently known in the LMC. Overlaid in dashed lines are the true spectra of the components in the emission model.

Figure 12. Sensitivity of the survey to a point source at the position of SN 1987A, compared to simple models for pion decay emission from the remnant (see Section 4.3 for details). Also shown as gray lines are power-law spectra with photon indices 2.2, 2.5, and 2.8 normalized such that they yield a broadband detection with TS = 25 for a point source at the position of SN 1987A.

Fig. 11 presents sensitivity curves for point sources at the positions of the four VHE objects currently known in the LMC, together with the original true spectra used for these components in our emission model. Obviously, these objects will be detected with high significance in small individual energy bins over most of the band, thus allowing fine spectral studies as will be discussed below in Section 4.2. Also apparent in this plot is the fact that sensitivity slightly depends on position in the field, with sensitivity loss of the order of ∼20 per cent over most of the range, peaking at ∼50 per cent at the very highest energies ∼100 TeV, as we go from central (N 132D, cyan sensitivity curve) to more peripheral (LMC P3, orange sensitivity curve) positions within the galaxy. We checked how the sensitivity to 30 Doradus C is affected by the proximity of the very strong N 157B source, and found that it degrades only by ∼10 per cent at the lowest energies ∼100 GeV.

Fig. 12 displays the sensitivity of the survey to a point source at the position of SN 1987A, in order to help assessing the de-

tectability of the object as function of different models of particle acceleration in the remnant. A more quantitative discussion of the prospects is provided below, in Section 4.3. Also shown as gray lines are power-law spectra normalized such that they yield a global detection with TS = 25 for a point source at the position of SN 1987A. Those were determined iteratively from a series of simulated observations and model fits (using only instrumental background and SN 1987A as model components), adjusting the normalization of the SN 1987A source until convergence to a global TS = 25. As a reference for the discussion to follow, these detection thresholds correspond to 1−10 TeV luminosities in the range of $2.0-2.4 \times 10^{-14}$ erg cm^{-2} s^{-1}. Taking into account variations at the 20 per cent level on sensitivity, depending on position in the field, we will henceforth assume that the typical
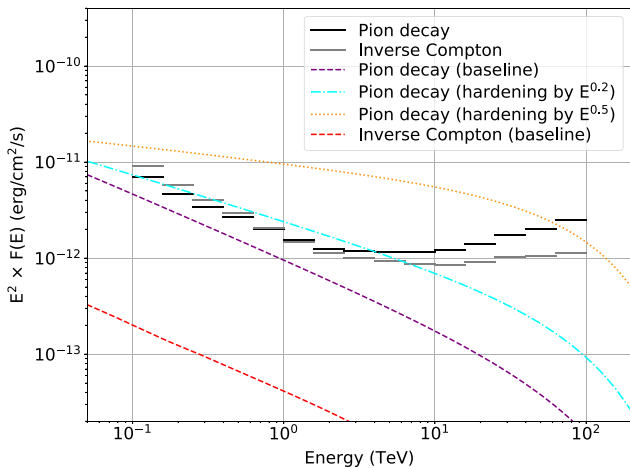
Figure 13. Sensitivity of the survey to large-scale interstellar emission from pion-decay and inverse-Compton scattering, with the specific morphology resulting from our emission model assumptions. Overlaid in dashed lines are the baseline spectra of the components in the emission model. In the case of pion decay, two variants are also shown in which the spectrum was hardened by multiplication with a power-law of index +0.2 and +0.5 and a pivot energy at 10 GeV.

$1-10$ TeV sensitivity of the survey to point sources is in the range of $1.6-2.9 \times 10^{-14}$ erg cm^{-2} s^{-1}.

Fig. 13 shows the sensitivity of the survey to large-scale interstellar emission from pion decay and inverse Compton scattering. In contrast to the sensitivities introduced before for point sources, which were mostly influenced by the position in the survey footprint, the survey to such extended components depends on the specific morphology resulting from assumptions made when building the emission model (e.g. diffusion coefficient, distribution of CR injection sites; see Section 2.3). In addition, we emphasize that the sensitivity is computed in very optimistic conditions, using the true source energy-dependent morphology and instrumental background properties in a full spatial-spectral likelihood fit. Nevertheless, this provides a useful reference as the best situation one can hope for and Fig. 13 shows that, even if this ideal set-up, large-scale inverse-Compton emission remains out of reach while pion decay could be detected with modest significance (TS ~ 60). The plot however illustrates the potential of the survey to detect or constrain large-scale pion-decay emission if it happens to be harder than assumed in our model. Such a prospect will be addressed more extensively below, in Section 4.4.

4.2 Known point sources

Fig. 11 makes it clear that the sensitivity level reached by the survey will allow detections of the four currently known VHE sources with very high significance and fine spectral studies over most of the energy range. Each one of these sources would deserve its own broadband modelling, taking into account a wealth of multiwavelength data, to establish which particular aspects of particle acceleration can be addressed by the CTA. This is however left out of the scope of the present paper and, in the following, we illustrate the potential of future spectral studies and tie these prospects to considerations on the physics at play in these objects.

Pulsar wind nebula N 157B belongs to a plerion involving PSR J0537 − 6910 and the ∼5000-yr-old SNR 0537.8−6910. The whole system has a diameter of 24 pc and presumably results from

the explosion of a ∼25 M$_\odot$ O8-O9 star and is likely associated with the OB association LH99 (Chen et al. 2006; Micelotta, Brandl & Israel 2009). The 16-ms pulsar is the most rapidly spinning and most powerful young pulsar known, with a spin-down luminosity of $\dot{E} = 4.9 \times 10^{38}$ erg s^{-1} (Marshall et al. 1998). N 157B was detected in H.E.S.S. observations and is the first and only PWN detected outside of the Milky Way in this energy band (Abramowski et al. 2012, 2015). This is accounted for by the high spin-down power of the pulsar combined with an intense infrared photon field for inverse-Compton scattering. In the CTA survey of the LMC, N 157B would be detected significantly from 100 GeV up to 100 TeV. With the physical model assumed here, which saturates the 2015 upper limit from Fermi-LAT at 100 GeV (Ackermann et al. 2016), detection in the low-energy range <1 TeV will allow an unambiguous connection of the HE and VHE domains and the exploration of a spectral range that probes a region of the particle spectrum where most of the spin-down power of the pulsar may be channeled (if the particle spectrum peaks around 100 GeV as assumed in Zhang, Chen & Fang 2008). In particular, it might be useful to figure out why N 157B seems to be a much less efficient particle accelerator than the Crab (Abramowski et al. 2015). At the other end of the band, a better characterization of the cut-off region around 100 TeV will provide key information about the maximum energies that can be reached and retained in young and powerful pulsar wind nebulae, especially in the context of X-ray observations revealing a cometary nebula expanding to large volume into a low-pressure parent SNR (Chen et al. 2006). Pulsed gamma-ray emission from PSR J0537−6910, similar to that observed from the Crab pulsar (Ansoldi et al. 2016), will also most likely be searched for in the 100 GeV–1 TeV range, although non-detection at GeV energies suggests a low pulsed fraction (Ackermann et al. 2015), and the strong steady emission from the nebula will make it difficult to extract such a signal.

N 132D is the brightest X-ray (and gamma-ray) SNR in the galaxy, with an estimated age of 2450 ± 195 yr (Law et al. 2020). The blast wave has a physical diameter of about 20 pc and exhibits a quite irregular morphology characterized by a horseshoe shape, with the southern part plowing through dense molecular clouds (Sano et al. 2015), giving rise to copious X-ray thermal emission (Borkowski, Hendrick & Reynolds 2007), while the northern part is blowing out in a lower density medium and is much dimmer in most bands. It was detected with both Fermi-LAT and H.E.S.S. (Abramowski et al. 2015; Ackermann et al. 2016; H.E.S.S. Collaboration et al. 2021), with a hard spectrum <100 GeV in the Fermi-LAT band and a much softer spectrum >1 TeV in the H.E.S.S. band. N 132D is extremely bright in the GeV range, actually the highest luminosity of all known GeV SNRs (Bamba et al. 2018; Acero et al. 2016), and therefore seems to be a prolific accelerator, in transition between young GeV-hard/TeV-bright and middle-aged GeV-bright/TeV-dim SNRs. In this evolutionary stage, the highest energy particles $\gtrsim$ 100 TeV have escaped the remnant and the content of ∼10 TeV particles may be close to its maximum (Ptuskin & Zirakashvili 2003, 2005). Transition objects like N 132D may be key to study how CRs progressively enrich the ISM and propagate in the vicinity of sources. The authors of Bamba et al. (2018) estimated that the gamma-ray emission cannot be predominantly leptonic in origin because the high GeV luminosity and faint non-thermal X-ray emission impose a small magnetic field strength and exceedingly large energy in accelerated electrons; the gamma-ray emission thus has to be mostly hadronic, and the authors estimated that particles still contained in N 132D have a maximum energy of 30 TeV. In this scenario, emission in the 10 TeV range is a mix of inverse-Compton and pion-decay contributions. An additional contribution to the signal, not considered in Bamba

et al. ([2018](#)) but mentioned in Vink et al. ([2021](#)), may come from the highest-energy particles that escaped the remnant and ought to radiate efficiently in the large amounts of molecular gas located in the close neighbourhood ($10^5\,M_\odot$, according to Banas et al. [1997](#)). Given the young age of N 132D, and if some kind of self-confinement is at work despite the abundance of neutrals in the medium, such particles should still be in the vicinity of the remnant (Nava et al. [2016](#)). N 132D would be detected with high significance in the low-energy range <1 TeV, and up to ∼10 TeV, which will allow testing the above ideas.

30 Dor C should not be confused with H II region 30 Dor and was actually named so because it appeared as a clearly separated component in the structure of the region in radio wavelengths (Le Marne [1968](#)). It was identified as a SB from radio, Hα, and X-ray observations (Mills & Turtle [1984](#); Mathewson et al. [1985](#); Dunne, Points & Chu [2001](#)). It has a diameter of about 90 pc and is powered by OB association LH 90 (Lucke & Hodge [1970](#)), composed of several clusters with estimated ages spanning $3-7$ Myr (Testor, Schild & Lortet [1993](#)). Its most distinctive feature is strong non-thermal X-ray emission filling most of its volume but being particularly bright along the northwestern part of its bounding shell (Bamba et al. [2004](#); Kavanagh et al. [2015](#)). The non-thermal emission spectrum is well accounted for from radio to X-rays under the assumption of an exponentially cut-off synchrotron model with a maximum electron energy of 80 TeV for a magnetic field of 10 µG (Kavanagh et al. [2015](#)). The origin of emitting particles however remains unclear. They could result from acceleration in the SB volume, for instance from strong stellar wind collisions in the central star clusters, interior SNR shocks interacting with high density gas clumps within the bubble, or turbulent acceleration, and later be captured in the magnetized SB shell (Kavanagh et al. [2015](#)); alternatively, they could be produced at the forward shock of an SNR that expanded during ≲20 kyr in the tenuous SB interior until reaching and colliding with its shell (Bamba et al. [2004](#); Yamaguchi, Bamba & Koyama [2009](#)). The latter scenario has received recent support from an observed anticorrelation between optical and X-ray shell morphologies, suggesting that the expanding shock has reached the shell and that parts of it are stalled in the densest regions while others continue with high velocities through gaps in the layer (Kavanagh et al. [2019](#)). This also provides a convenient explanation for enhanced X-ray emission from the SB walls, reheated by the interior SNR shock collision, an idea well motivated by both observations (Jaskot et al. [2011](#)) and simulations (Krause & Diehl [2014](#)). 30 Doradus C was detected at TeV energies in H.E.S.S. observations but the origin of the gamma-ray emission associated remains unclear. In the scenario promoted in Kavanagh et al. ([2019](#)), the TeV emission comes from inverse-Compton scattering of the same population of energetic electrons that powers X-ray synchrotron emission, and any hadronic contribution would be secondary. The survey should enable us to test this idea via significant detection in the <1 TeV region, where hadronic and leptonic contribution would markedly differ (Abramowski et al. [2015](#)). The search for a hadronic contribution can also be carried out at the other end, above 10 TeV, where subdominant pion decay emission could extend much beyond the inverse-Compton spectrum downturn because protons and nuclei are not loss-limited, contrary to electrons.

LMC P3 is a binary system comprising a compact object of unknown nature, a neutron star being preferred (Corbet et al. [2016](#); van Soelen et al. [2019](#)), and an O5-type stellar companion. This source was first discovered in the X-ray band as a hard point source in very energetic SNR (Bamba et al. [2006](#)), and later identified as a high-mass X-ray binary in the X-ray band again (Seward et al.

[2012](#)). A GeV source was later detected in coincidence with SNR DEM L241 (Ackermann et al. [2016](#)), and later confirmed as a gamma-ray binary through a 10.3 d orbital modulation of the signal in the GeV (Corbet et al. [2016](#)) and TeV range (Abdalla et al. [2018a](#)). The orbital parameters of the system were subsequently refined in van Soelen et al. ([2019](#)). It is an object of a rare kind, with only about half a dozen currently known members of the class (Dubus [2013](#)), and in any case the first such source detected outside the Milky Way and the most luminous of all, with an orbit-averaged luminosity in the $1-10$ TeV range of $1.4 \pm 0.2 \times 10^{35}$ erg s^{-1}. This binary is also very unique since it is in a SNR, implying a relatively young system, and this may explain why it is the brightest gamma-ray binary. H.E.S.S. observations of LMC P3 (also named HESS J0536–675) led to the detection of significant emission over only 20 per cent of the orbit, in contrast to similar object LS 5039 but akin to 1FGL J1018.6–5856 (Abdalla et al. [2018a](#)). High-significance detection of the object over most of the CTA energy range should allow a more accurate characterization of the orbital light curve, together with phase-resolved spectral analyses hardly accessible with the current H.E.S.S. sensitivity. Combined with ever-improving data from Fermi-LAT until CTA becomes operational, this will allow thorough investigation of the origin of the GeV and TeV emission from LMC P3, especially their different behaviours such as the observed phase offset in the orbital variability (Abdalla et al. [2018a](#)). Given the recent identification of the system, the questions to be addressed in LMC P3 are still rather generic to gamma-ray binaries: clarifying the various processes shaping gamma-ray emission from binaries and their relative contributions, in that specific object and along its orbit, and in particular, moving forward in the growing consensus that different populations of particles, accelerated in different regions (pulsar magnetosphere, pulsar wind, wind-wind collision layer) and/or by different mechanisms (shock acceleration, reconnection), are involved and manifest themselves through specific spectral and temporal signatures in different (gamma-ray) wavebands (Dubus [2013](#)).

4.3 SN 1987A

SN 1987A is a source of major interest in the LMC, as a well-studied remnant that could provide insight into the very first stages of particle acceleration following a core-collapse SN explosion. Particle acceleration in SN 1987A is already at work, as evidenced by the increasing radio synchrotron emission detected from the remnant since about 1200 days after outburst (Zanardo et al. [2010](#)). The radio spectrum exhibits a power-law shape and its index over the 843 MHz to 8.6 GHz frequency range has evolved from -0.932 ± 0.051 to -0.758 ± 0.037 over year 5 to year 19 after explosion (Zanardo et al. [2010](#)). As of late 2013–early 2014, the spectral index over the 0.072– 8.64 GHz range is -0.74 ± 0.02 (Callingham et al. [2016](#)), which implies an emitting electron population having a power-law distribution of index 2.5. This is steeper than the canonical flat distribution with index 2.0 expected for diffusive shock acceleration in the test particle limit. Such a steep distribution could result from acceleration in a CR modified shock, with a subshock compression ratio of 3 that affects the acceleration of the lower energy particles (Zanardo et al. [2010](#); Callingham et al. [2016](#), and references therein); alternatively, it can result from acceleration in the presence of subdiffusion transport across the shock front due to trapping of particles in braided magnetic field structures (Kirk, Duffy & Gallant [1996](#)), or from the drift of magnetic structures with respect to the downstream thermal plasma (Caprioli, Haggerty & Blasi [2020](#)). Whatever the origin for this steep distribution, radio observations probe particle energies that are quite

far from what would be probed with CTA. For a typical magnetic field with an order-of-magnitude strength of 10 mG downstream of the forward shock in SN 1987A (Berezhko, Ksenofontov & Völk 2011, 2015), synchrotron emission in the 1–10 GHz range arises from sub-GeV electrons. How the particle distribution behaves beyond this range, up to what maximum energy, and in which proportions for electrons and nuclei remains currently unknown in the absence of detection at gamma-ray energies, and is precisely a major science case for CTA. Non-thermal X-ray emission was also detected from SN 1987A and could be a more direct probe of particles with energies relevant to CTA, but the very origin of the emission is unclear and contamination by an absorbed PWN is likely (Greco et al. 2021).

Several analyses or models of the shock dynamics linked to particle acceleration can be found in the literature (Zhekov et al. 2010; Berezhko et al. 2011; Dwarkadas 2013; Berezhko, Ksenofontov & Völk 2015; Petruk et al. 2017). The full problem is quite complex. The SN ejecta drove a blast wave in a circumstellar medium that was shaped by the progenitor star or system into a highly structured and anisotropic matter distribution summarized in Potter et al. (2014). Most of the mass encountered by the blast wave so far lies in an equatorial disc, a density enhancement in the circumstellar medium likely resulting from the interaction of dense wind emitted during the red giant phase of the progenitor and a subsequent fast wind emitted in a blue supergiant phase before explosion. It has a half-opening angle $15° \pm 5°$ and typical density $\sim 100 \, cm^{-3}$, and contains knots or fingers with density tens to hundreds times higher. In the polar directions is a bipolar bubble of hot shocked blue supergiant wind with density of $0.1 \, cm^{-3}$. In such an environment, the initial blast wave gave rise to a variety of shocks with different velocities: forward shock propagating in most of the volume of the equatorial ring, reverse shock propagating in the SN ejecta, transmitted and reflected shocks triggered from interaction with dense clumps. Each of the models mentioned above relies on specific assumptions for the respective contributions of the various shocks at play in SN 1987A and the conditions in which they evolve. It is beyond the scope of this work to present a complete and up-to-date model or discussion of the non-thermal processes in SN 1987A. Instead, for illustrative purposes mostly, we provide below model spectra from a very simple model that however captures some of the important constraints available today.

Starting with the energetics, the total swept up mass so far is of the order of $0.1 \, M_\odot$ (Potter et al. 2014), by a forward shock that has been expanding over the past years at a velocity of $3890 \, km \, s^{-1}$ estimated from radio observations (Ng et al. 2013). This corresponds to 1.5×10^{49} erg of kinetic energy that flowed into the forward shock front, about 1 per cent of the estimated total initial ejecta kinetic energy of the explosion, or 4 per cent if we restrict this ratio to the solid angle subtended by the equatorial disk (Potter et al. 2014). We supposed that a canonical 10 per cent of this kinetic energy went into diffusive shock acceleration of protons. The proton spectrum is assumed to follow a broken power-law distribution in momentum starting from 100 MeV/c, with a change in slope at 1 GeV/c and an exponential cut-off at an arbitrary momentum of 100 TeV/c. The sub-GeV part of the spectrum has a fixed index 2.5, as required by radio observations of synchrotron emission from electrons. We checked that injecting a fraction of order 10^{-4} of the energy into accelerated electrons, and assuming they radiate in a 10 mG downstream magnetic field (Berezhko et al. 2011, 2015), yields a synchrotron intensity at the Jy level at 1 GHz, as observed (Callingham et al. 2016).

We then considered different assumptions for the spectrum slope at higher energies. A minimalist and worst-case model assumes that the spectrum simply extends with the same slope up to the cut-off energy. Alternative more optimistic models rely on the possibility of a hardening of the spectrum above some energy. Such concave shapes are characteristic of the non-linear diffusive shock acceleration (DSA) theory, at least in its most basic version, with spectra steeper or harder than the test-particle DSA prediction below or above transrelativistic energies, respectively (Drury & Voelk 1981; Eichler 1984; Berezhko & Ellison 1999). In the context of SN 1987A, this possibility was explored in Berezhko et al. (2011), Berezhko et al. (2015), whose latest model predicts a hardening up to a power-law index of about 1.8. Yet, the degree of hardening or even its very existence were largely questioned over the past decade. This stems mostly from the non-detection of a corresponding signature in radio or gamma-ray observations of young SNRs, with inferred indices for the emitting particle populations of $\sim 2.2-3.0$ (Caprioli & Haggerty 2019). Additional evidence challenging concave distributions from non-linear DSA came from analyses of locally measured CR spectra in the framework of standard Galactic propagation models (see e.g. Trotta et al. 2011; Evoli et al. 2019); despite coming with different assumptions on source and transport terms, they invariably require power-law indices in the range of $\sim 2.3-2.4$ for the nuclei injection spectra above $\sim 10 \, GeV$ (although it remains unclear in this context how exactly such injection spectra are shaped by the processes of acceleration in the source and escape from it).

For a series of possible proton spectra above 1 GeV, from the softest option with index 2.5 to the hardest option with index 1.8, we computed the associated pion-decay signal, under the assumption that the particle population is interacting with compressed gas downstream of the forward shock having a typical density $\sim 400 \, cm^{-3}$ (this corresponds to the above-mentioned upstream density in the equatorial disk, increased by a compression ratio of 4 appropriate for a strong shock; higher compression ratios of 6–7 are possible in the context of a CR-modified shock). A nuclear enhancement factor of 1.753 appropriate for the LMC is applied (see previously).

The resulting model spectra are shown in Fig. 12, together with the sensitivity of the CTA survey to a point source at the position of SN 1987A and the H.E.S.S. upper limit published in 2015 (Abramowski et al. 2015). Our most optimistic model with a hard spectrum is similar to that presented in Berezhko et al. (2015) and is already dismissed by the H.E.S.S. observations (Abramowski et al. 2015). At the other end, the worst-case model with a soft spectrum extending that of sub-GeV electrons is more than a factor 20 below the sensitivity curve, a gap that it would not be easy to close with corrections of order unity on the acceleration efficiency and/or downstream density. Our simple modelling suggests that meaningful spectral analyses would be accessible to CTA for rather flat spectra, with power-law slopes of ~ 2.0, which would imply processes flattening or hardening up the spectrum towards high energies.

While this is already interesting enough, we emphasize that an object like SN 1987A deserves a tailor-made modelling harnessing the growing wealth of multiwavelength information on the shock history and environment. The very simple model used here implicitly relates the radio and gamma-ray emission whereas they could arise from distinct regions owing to different distributions of the CR species and targets involved in the respective radiative processes; for instance, radio could be mainly produced in the lower density ionized regions above and below the equatorial plane, while gamma rays would predominantly come from the higher density clumps (see Figs 4 and 5 in Berezhko et al. 2015). Furthermore, there ought to be more than plain and simple acceleration at the forward shock as presented here, for instance a contribution from reflected shocks

reaccelerating freshly accelerated particles while enhancing further the density in which they radiate, such that prospects for detection and study may well be more promising. In addition, the conditions of particle acceleration and non-thermal emission are most likely strongly time-dependent, and may significantly evolve over the next $10-20$ yr, a reality that is not captured in the rough model used here where the spectral index or downstream density are fixed to a single value; gamma-ray emission with a soft spectrum with photon index $\sim 2.3-2.4$, as observed in many Galactic SNRs, would become within reach of simple broadband detection pending a flux increase by a factor of $3-4$ (compare the cyan curve and gray lines in Fig. 12). At the very least, the above discussion demonstrates that the survey should bring us into the right ballpark, especially if the emission from SN 1987A is on the rise, and tell us something about proton acceleration in SN 1987A, at last.

4.4 Large-scale interstellar emission

As illustrated in Fig. 13, the spectral sensitivity of the survey to the specific intensity distribution of inverse-Compton emission is at best a factor of 30 above the expected emission level in the case of the average ISM model. Using the more intense ISRF of the gas-rich ISM model pushes the emission level up by a factor of a few and only a very hard electron injection spectrum with power-law index $\lesssim 2.2$ would lead the predicted inverse-Compton emission to rise close to the survey sensitivity. Including the contribution of secondary leptons from charged pions would increase the level of the emission by no more than 30 per cent, according to the estimate of the contribution of secondaries presented in Section 2.6, and this additional component would have a more uniform spatial distribution likely making its detection more challenging. Overall, interstellar inverse-Compton emission on galactic scales may be out of reach of the CTA survey of the LMC.

Prospects for detecting galactic pion-decay emission are more encouraging. The spectral sensitivity of the survey to the intensity distribution of our baseline pion decay emission model is a factor of ~ 2 above the expected total flux level at energies below a few TeV. High-significance detection as a very extended component and fine-binned spectral studies therefore seem to be excluded for the baseline model, but pion-decay emission with a harder spectrum could be detectable in several individual energy bins, at the very least in the regions most rich in gas. We review in Appendix D some motivations for considering the possibility of harder emission than assumed in our baseline model, and we provide below quantitative prospects for the detectability of pion decay over galactic scales in the LMC.

The potential of VHE diffuse interstellar emission for the study of the highest energy CRs, up to the knee, has been demonstrated already for the Galaxy (Lipari & Vernetto 2018; Cataldo et al. 2019). The CTA survey of the LMC may provide valuable complementary information. This is illustrated in Fig. 13, where the sensitivity to the pion decay emission template is compared to total emission spectra for the baseline model, and for the baseline model hardened by multiplication with power laws with indices $+0.2$, to reflect a possible harder interstellar population of CRs above $200-300$ GV as measured locally by AMS-02, and $+0.5$, to mimic the extreme case of the LMC having a spectrum similar to that of starburst galaxies M82 or NGC253 (Acciari et al. 2009; H.E.S.S. Collaboration et al. 2018; Ajello et al. 2020). Henceforth, we will refer to these models as BASE, HARD020, and HARD050, respectively. The hardened variants of the model yield spectra with power-law photon indices ranging approximately from 2.55 to 2.25 (away

from the ~ 100 TeV cut-off that arises from the assumed 1 PeV maximum proton energy). We emphasize here that these modified models, with emission levels up to $\sim 10-20$ times that of our baseline model in the $1-10$ TeV range, are still consistent with the non-detection with H.E.S.S. of small-scale features in interstellar emission.

Fig. 13 illustrates that model HARD020, with properties similar to those inferred for central regions of the Milky Way, could be detectable in individual energy bins over most of the $0.1-10$ TeV range, while model HARD050, representative of the few starburst galaxies studied over the GeV–TeV range, could be spectrally resolved over the entire energy band, up to almost 100 TeV. In terms of broadband detection, in the ideal case of a full spatial-spectral maximum-likelihood approach with the true source model, models BASE, HARD020, and HARD050 would be detected with average TS values of about 60, 350, and 6650, respectively. Despite such significance levels, however, recovering the emission on large, galactic scales may not be trivial and will most likely be restricted to just a few regions of the galaxy. Presenting a complete and realistic data analysis aimed at extracting large-scale emission of unknown true distribution is beyond the scope of this paper. Instead, we illustrate in Fig. 14 the layout of significant diffuse emission by showing TS maps obtained from Asimov data sets by fitting a test source consisting of a 2D Gaussian with fixed $\sigma = 0.1°$ for the spatial part, and a power-law with fixed photon index 2.5 for the spectral part, on a regular grid of 80×80 positions spanning the whole field. For model BASE, extended emission over several tenths of a degree is recovered at only one position in the galaxy, in the molecular ridge south of 30 Doradus, and with limited significance peaking at TS ~ 20. Model HARD020 offers the perspective of more accessible and widespread emission, with significant degree-scale emission in two regions, the molecular ridge and the molecular cloud complexes towards star-forming region N44, with TS values peaking at ~ 100. Last, model HARD050 makes it possible to detect interstellar emission over a region spanning about one-third of the galaxy and covering many gas-rich and active star-forming locations. Should this model be a good description of the LMC, the separation of diffuse emission from populations of sources in these sites will become a major issue.

The most prominent feature in the TS maps is the so-called molecular ridge. It is a cloud complex stretching ~ 2 kpc south of 30 Doradus, at right ascension $84°$ and from declination $-69.5°$ to $-71°$. It consists in dense clouds bathed in lower density molecular gas (Fukui et al. 2008). Together with an arc-like structure delineating the southeastern edge of the galaxy (less visible in our model map), the region contains an estimated 35 per cent of the total CO-traced molecular gas mass of the galaxy (Mizuno et al. 2001), and about 20 per cent of the total amount of atomic gas (which would then be the dominant gas phase by mass in this area, since there is about eight times more atomic gas than molecular gas in the galaxy; see Section 2.3) (Luks & Rohlfs 1992). The existence of so much interstellar gas packed in this region offers a useful way to probe the background level of CRs in the galaxy, ensuring an efficient production of gamma-rays over a relatively small patch of the sky that fits into one CTA field of view, thus restricting the data analysis challenge to the search for a moderately extended source. On the other hand, such a region may be particularly prone to ionization-dependent transport effects, like those investigated in Bustard & Zweibel (2021) for GeV CRs. Fast transport in cold dense gas, if also applicable to TeV CRs, would tend to lower the pion-decay emission of these gas phases, although Bustard & Zweibel (2021) seem to suggest that the impact is mostly on emission layout and not
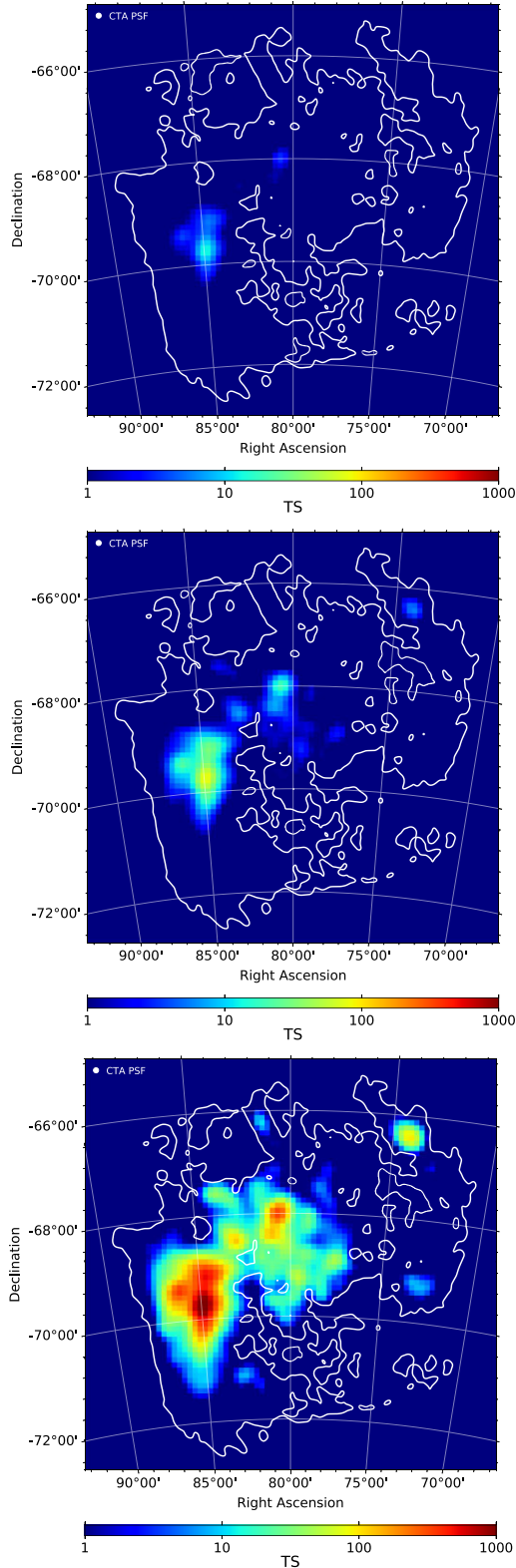
Figure 14. Average TS maps for three galactic pion-decay emission models: the baseline set-up (top panel) and hardened variants obtained by scaling the energy dependence with power laws of index +0.2 and +0.5 (middle and bottom panel, respectively) These are referred to as BASE, HARD020, and HARD050 in the text. The TS maps were obtained from Asimov data sets using as test source a 2D Gaussian model with fixed $\sigma = 0.1°$ associated to a power-law spectral model with fixed photon index 2.5.

so much on total luminosity, which would mitigate the problem for a distant source like the LMC.

4.5 The 30 Doradus star-forming region

As mentioned in Section 2.3, 30 Doradus was not included as a CR injection site in our model for large-scale interstellar emission, mainly because the region as such was not detected as a peculiar or outstanding source in Fermi-LAT observations and not detected at all in the HE.S.S. survey, probably due to its relatively young age (see discussion and arguments in Appendix A). There is, however, a huge potential for particle acceleration and gamma-ray production in 30 Doradus, so emission should be present at some level and we here investigate under which conditions it could be accessible to the CTA survey.

We focus on the region as a whole, in the sense of a site delivering a large amount of mechanical power, a fraction of which can be tapped for particle acceleration, irrespective of how exactly the latter is achieved. In interpreting Suzaku X-ray observations of the 30 Doradus nebula, the authors of Cheng, Wang & Lim (2021) came up with an estimated 8.3×10^{52} erg of total mechanical energy injected by the central OB association NGC 2070, more precisely by a stellar population made up of two subgroups with estimated ages 2 and 4 Myr (Sabbi et al. 2012), although more extended star formation up to 6–8 Myr is also proposed (Schneider et al. 2018). In this framework, most of the energy was released from stellar winds and only 1.3×10^{52} erg is expected to result from SNe. Bearing in mind the uncertainty on the actual star formation history, this corresponds to a mechanical luminosity of $\sim 10^{39}$ erg s^{-1} during a few Myr, similar to the value inferred for the most massive star-forming regions in the Galaxy (Aharonian et al. 2019).

We implemented the SFR emission model described in Section 2.4 in the specific case of 30 Doradus. We considered six possibilities for diffusion suppression within 100 pc of the SFR centre – 1, 3, 10, 30, 100, 300 times smaller than the average interstellar value over large galactic scales – and for each value we computed the corresponding diffusion kernel and the associated pion-decay emission for the actual gas distribution in the region. At this point, only the morphology of each model matters, and the normalization is arbitrary. In a first study, we performed an iterative series of simulations and analyses of survey observations of the SFR, with instrumental background as the only other source component, renormalizing the SFR source model between iterations until the process converges towards a global detection with TS = 25 over the full energy range. The eventual renormalization factor of the SFR model sets the minimum CR injection luminosity, hence gamma-ray emission level, that would allow detecting the SFR for a given diffusion suppression factor. In a second study, we perform the same kind of iterative search, aiming this time at the minimum renormalization of the model that would allow its significant differentiation from the reference case of diffusion without suppression (i.e. CRs released by the SFR diffuse out with the average galactic coefficient). We adopted TS = 16 as the minimum significance level in that case.

The results are shown in Fig. 15. If diffusion around 30 Doradus is not suppressed, the required CR injection power for global TS = 25 detection corresponds to about 40 per cent of the assumed $\sim 10^{39}$ erg s^{-1} mechanical power of the cluster (under the hypothesis of a power-law injection spectrum with index 2.25 extending from 1 GeV to a cut-off energy of 1 PeV). This rather high value is not unmotivated theoretically for SFRs (Bykov 2001) and it remains allowed in terms of energetics: the energy census in 30 Doradus and other SBs (30 Doradus C or DEM L192 for instance) reveals
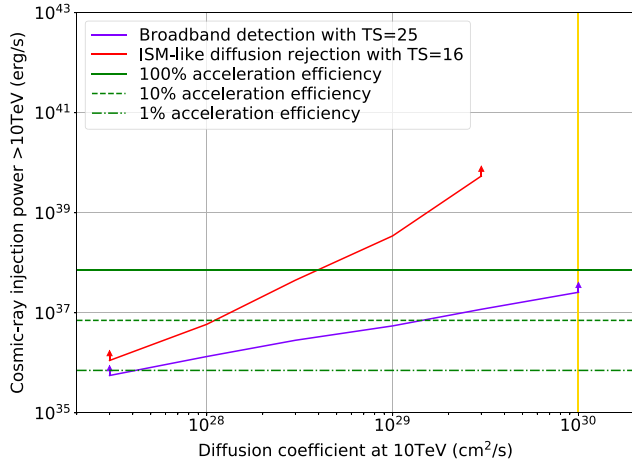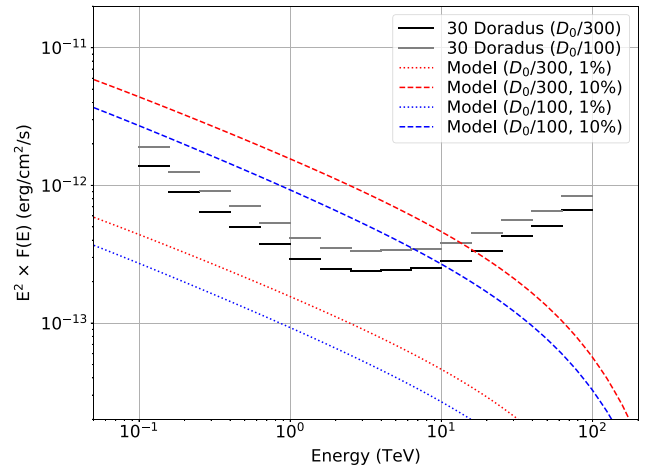
Figure 15. Integrated sensitivity to pion-decay emission from CRs injected at the centre of SFR 30 Doradus and diffusing away, expressed as the minimum CR injection power above 10 TeV, as a function of the 10 TeV diffusion coefficient in the <100 pc vicinity. The purple curve shows the requirement to achieve a global detection with TS = 25 over the full energy range, while the red curve shows the requirement to achieve both detection and significant rejection of fast diffusion typical of the average galactic disk at a level of TS = 16. The green curves display the level of >10 TeV CR injection in 30 Doradus, for different efficiencies in converting the ~10^{39} erg s^{-1} mechanical luminosity into >1 GeV CRs, and the yellow vertical line marks the large-scale average value of the diffusion coefficient, for reference.

Figure 16. Spectral sensitivity to pion-decay emission from CRs injected at the centre of SFR 30 Doradus and diffusing away in a <100 pc region where diffusivity is suppressed by a factor of 100 or 300 with respect to the average galactic value. Overlaid are model spectra for 1 per cent and 10 per cent efficiencies in converting the assumed ~10^{39} erg s^{-1} mechanical luminosity of 30 Doradus into >1 GeV CRs.

that half or more of the injected energy is not found in the form of kinetic or thermal energy in the SBs, hence lost to some channels not accounted for in classical SB models (Weaver et al. 1977; Mac Low & McCray 1988); CR acceleration with high efficiencies is one possibility (Butt & Bykov 2008), although there are several other competing and well-motivated mechanisms (Cheng et al. 2021). On the other hand, constraints on acceleration from stellar winds in several Galactic clusters can be as low as 1 per cent (Maurin et al. 2016), although most objects in this study are much smaller and younger than 30 Doradus and thus not directly comparable. As diffusion suppression increases, CRs are more confined in the vicinity of the source, which raises gamma-ray emission from the region and diminishes the energetics required for detection. For diffusion suppression factors of a few hundreds, 30 Doradus would be detectable for acceleration efficiencies below 1 per cent. Such a level of diffusion suppression is not unreasonable theoretically and seems indicated in similar Galactic SFRs (Aharonian et al. 2019).

Fig. 16 shows the spectral sensitivities to the specific emission morphologies resulting from the highest levels of diffusion suppression considered here, 100 and 300. They are compared to model spectra for 1 per cent and 10 per cent efficiencies in converting the assumed ~10^{39} erg s^{-1} mechanical luminosity of 30 Doradus into >1 GeV CRs. It appears that even with such efficient confinement in the vicinity of the SFR, acceleration efficiencies of 10 per cent at least would be required to detect the source up to 10 TeV, where the turnover due to the 1 PeV cut-off in the proton spectrum barely starts to be discernible. It therefore seems that the survey sensitivity may not be enough to investigate the possible role of SFRs in the production of the highest-energy galactic CRs, unless the injection is harder than assumed here (power-law index of 2.25).

While prospects for simple detection of 30 Doradus as an SFR are encouraging, its identification as such may be more challenging. Even

more challenging would be the inference of the CR injection power, which depends on the actual diffusion coefficient (Aharonian et al. 2019). Solid evidence serving both goals would be the significant detection of a spatial intensity distribution characteristic of central injection and suppressed diffusion (see Fig. 5). A complete and realistic assessment of such a prospect, including decomposing the emission into a radial profile while simultaneously determining foreground and background interstellar emission from the galaxy, is beyond the scope of the present work. Instead, we quantified the requirement for being at least able to differentiate the emission profile characteristic of diffusion suppression at a given level from no diffusion suppression at all. Fig. 15 shows that the requirements on the level of injection then become more demanding. In the case of diffusion suppression by a factor of a 100 or more, acceleration efficiencies in the range of 1–10 per cent are required for the SFR to be detected and identified as having a specific emission profile not compatible with fast diffusion typical of the average galactic disc. This does not necessarily ensure a recovery of the diffusion coefficient true value with high precision, though, but it could be used at the very least to set an upper limit on the diffusion coefficient in the vicinity of the source. For lower diffusion suppression factors, below a few tens, the requirements for morphological separation ramp up to prohibitive values of the injection power, in excess of 100 per cent. In this range, source detection remains possible but it would be impossible to constrain the intensity distribution to a specific diffusion profile.

Last, we emphasize that the above prospects should be considered as optimistic because they were derived from simulations including 30 Doradus as only astrophysical source. In the process of detecting and studying such an extended target, the unknown interstellar emission from the galactic disk would come as a nuisance parameter. While our baseline model for it suggests it could hardly be detectable, and thus not affect too much the above estimates, alternative models could bring the level of large-scale interstellar emission to much higher values that could jeopardize a proper identification of 30 Doradus as a gamma-ray emitting SFR (see Section 4.4).

4.6 Source population

The realization of the source population model introduced in Section 2.2 contains 71 SNRs, 10 iSNRs, 91 PWNe, and 167 haloes around mature pulsars, so a total of 339 objects. In Section 4.1, we determined that the typical point source sensitivity reached in the CTA survey is $1.6-2.9 \times 10^{-14}\,\mathrm{erg\,cm^{-2}\,s^{-1}}$ in the 1–10 TeV range, with variations due to position in the field and spectral shape. As illustrated in Fig. 1, this would allow the detection of at most a dozen objects, and only half of that if we are conservative and assume the higher end of the sensitivity range. We show below that the latter conservative estimate seems more appropriate to what can actually be achieved.

For SNRs and iSNRs, our model suggests that the survey would give access to a handful of sources making up the very high end of the luminosity distribution only, those objects resulting from high explosion energies and/or high acceleration efficiencies and/or very dense target fields (gas or photons). Less than 10 per cent of the PWNe population could be probed, which could however double the number of known such objects in the LMC. Currently only three have been identified: N 157B, already detected as TeV source; B0540-69, which holds promise for detection with CTA owing to its highly powerful Crab-twin pulsar (Martin et al. 2014); and B0453-685 (Gaensler et al. 2003; McEntaffer, Brantseg & Presley 2012). In the framework of our model, a comparable number of pulsar haloes would be detected in the survey, despite the optimistic assumption that all middle-aged pulsars past the PWN stage do experience such an evolutionary phase (see Martin et al. 2022a, for arguments on the possible rarity of pulsar haloes).

We implemented a blind search for point-like sources in one simulation of the survey based on the full model, i.e. including the four known sources, pion-decay and inverse-Compton large-scale emission templates, plus all SNRs, iSNRs, PWNe, and pulsar halos from the realization of our population model. This was done using the *cssrcdetect* tool from the ctools package, which implements a peak detection algorithm in a significance map. By trial and error, comparing the output to the true population of sources, we found that the optimum parameters are: (i) a counts map in the 1–100 TeV range, for the calculation of the significance; (ii) an averaging radius of $0.5°$, to compute the mean value and standard deviation in each pixel; (iii) an exclusion radius of $0.2°$, to exclude counts around a previously detected source; (iv) a correlation kernel consisting in a disk with radius of $0.05°$, to smooth the input counts map.

Using a significance threshold of 5σ leads to the detection of ten sources, the four known ones and six mock objects. The layout of these sources is illustrated in Fig. 17, which displays also the distribution of the 13 most luminous objects in our mock population model, with 1–10 TeV fluxes $>2.0 \times 10^{-14}\,\mathrm{erg\,cm^{-2}\,s^{-1}}$. Among the 13 brightest mock sources, three are not recovered when using a 5σ detection threshold because they are the faintest of the subset and have unfavourable spectra yielding the lowest photon fluxes. They are detected when lowering the threshold to 3σ, but at this point a non-negligible number of spurious detections appear, at positions devoid of true sources in our model. Leaving known sources aside, Fig. 17 reveals that half of the detected sources encompasses isolated mock objects, while the other half is positionally coincident with clusters of bright sources. In these locations, one source is detected where there are in reality two or three overlapping true sources strong enough to be detected individually each. This gives a first taste of the issue of source confusion in the LMC. Whether these could be separated by more dedicated studies, exploiting spectral differences
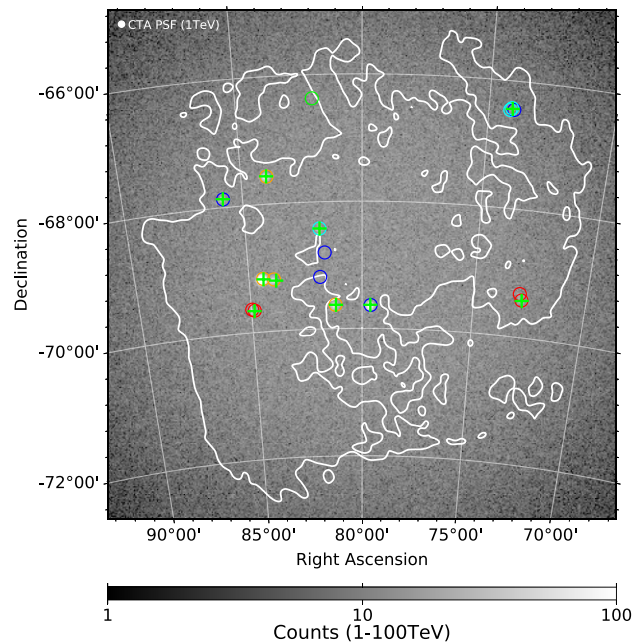
Figure 17. Distribution of point-like sources found in a blind search for a significance threshold of 5σ (green crosses). The coloured circles are the positions of the most luminous true sources in the model, with 1–10 TeV fluxes $>2.0 \times 10^{-14}\,\mathrm{erg\,cm^{-2}\,s^{-1}}$: SNRs in green, iSNRs in cyan, PWNe in blue, pulsar halos in red, and known sources in orange (same marker size for all such objects, irrespective of their true or mock physical extent). The background image in gray scale is a 1–100 TeV counts map.

and/or the improved angular resolution at higher energies and/or events subclasses with better incident direction reconstruction, is beyond the scope of this work.

We assessed whether the recovered sources have a significant extension and found only marginal evidence for extension in two sources, with TS values of $12-14$. We also checked that adopting a different hypothesis for source distribution, relaxing the scaling of the membership probability with H II region luminosity so as to yield sources more uniformly spread over all H II regions instead of clustered inside the most prominent ones, does not profoundly alter the picture. The limited effect is due to the fact that the 138 H II regions used in this work tend to be themselves clustered over a rather small fraction of the galaxy area.

We completed the blind search process by fitting the detected $>5\sigma$ sources over the full 0.1–100 TeV range, assuming for each source a simple power-law model. The positions of all sources were optimized in the process. Apart from the sources found in the blind search, only the true model for the instrumental background was fitted to the data (i.e. no models for large-scale interstellar emission). The ten sources are detected with TS values ranging from a few tens to a few thousands. The flux distribution of the fitted sources is shown in Fig. 18 and demonstrates an overall pretty satisfactory recovery of the true source fluxes, despite using a very simple procedure. The effect of source confusion in a limited number of cases is visible as a small deviation at the lowest detected fluxes.

4.7 Dark matter sensitivity curves

In this section, we calculate forecasts for the detection of an additional emission component due to the annihilation of DM particles.
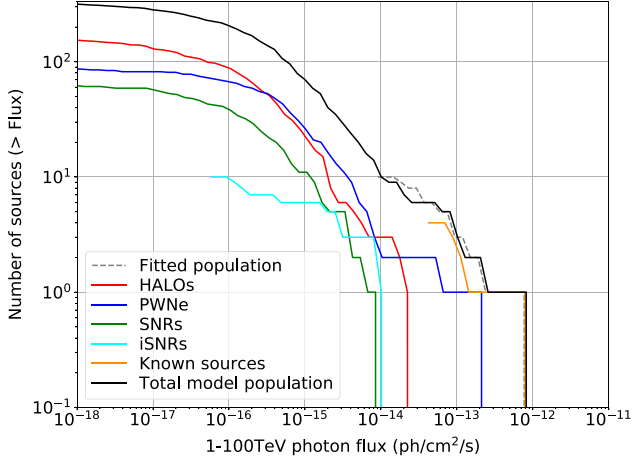
Figure 18. Flux distribution of the fitted $>5\sigma$ sources detected in the blind search, compared to the true flux distributions of the various source populations in the model.

The goal is to explore whether CTA will be able to observe the annihilation of WIMPs in the LMC, and if detection (or failure thereof) can be useful in the identification of DM candidates. In doing so, we incorporated the fact that the prospects for such detection or constraint depend on the degree of contamination of the observations by classical sources.

In line with the common use in the literature, we do not aim here at forecasts for a specific DM candidate but rather at sampling the range of signals that should be expected within a 'standard' WIMPs scenario. While treating $\langle \sigma v \rangle$ and m_χ as independent variables, we sample the 'single particle' spectrum of the annihilation, namely the gamma-ray emission produced in an annihilation process in which the two DM particles annihilate in different types of standard model primaries and generate a subsequent cascade of high-energy photons.

Using the DM profiles and spectra described in previous sections, we performed a likelihood analysis to calculate upper limits, as described in Section 3.3, using the function *ctulimit* from the CTOOLS software package. The Asimov data set for the full baseline emission model, used in the analyses presented in previous sections, is here used as a background from which we try to disentangle the DM emission. Each DM model is included in the fitted model separately and we calculate the differential flux upper limit, the integrated flux upper limit over the energy range 0.1 GeV-DM particle mass, and the integrated energy flux limit.

The limit in terms of $\langle \sigma v \rangle$ can be extracted from the resulting integrated flux limit, using equation (17), obtaining the corresponding value of $\langle \sigma v \rangle$, for the specific J-factor and particle mass. The sensitivity curves of $\langle \sigma v \rangle$ versus DM particle masses are shown in Figs 19–22. Three curves are shown in the plots for each annihilation channel and profile, corresponding to different scenarios regarding the gamma-ray background. The black lines represent the sensitivity curves obtained when including all the components of the LMC emission model in the fit. The crosses and blades represent the results reducing the fitted model to just the pion-decay template or the strongest point sources, respectively. In these cases, the full emission model is used in the observations simulation, but just a subset of the components are included in the fitted emission model on top of which we search for a DM signal.

The sensitivity curve is lower when fitting the full emission model, pointing to a better sensitivity to a DM signal when all
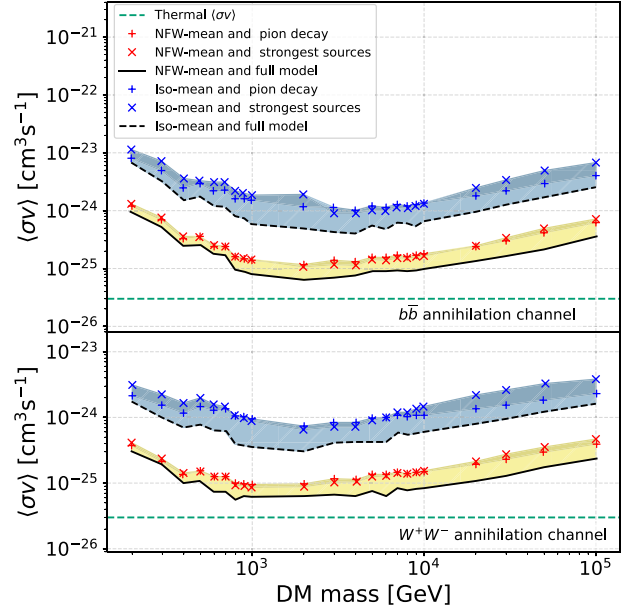
Figure 19. Sensitivity bands in terms of velocity-averaged annihilation cross section as a function of DM particle mass, resulting from the mean density profiles listed in Table 2 and the $b\bar{b}$ and W^+W^- annihilation channels, for different LMC emission models.
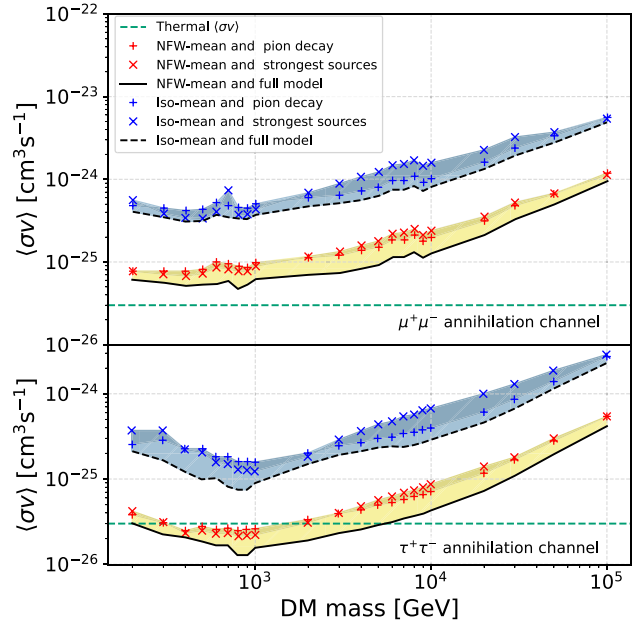
Figure 20. Same as Fig. 19 for the $\mu^+\mu^-$ and $\tau^+\tau^-$ annihilation channels.

true components of the emission are used in the analysis. This illustrates the advantage of having an extended object that can be spatially resolved, such as the LMC, the emission of which can be carefully decomposed. When using the full model, the baryonic emission components are more tightly constrained and better separated from the DM template. Alternatively, when using only a subset of the components (pion decay template or strongest sources), their correlation with other true components of the baryonic emission leads to a higher DM signal being required for significant
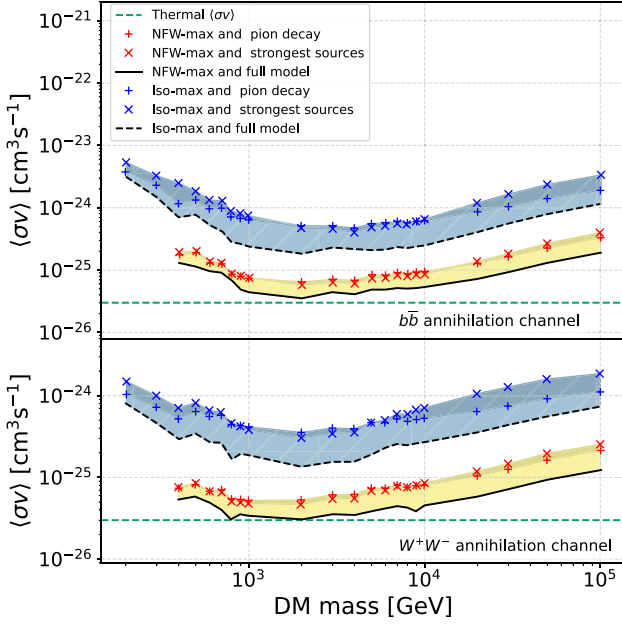
Figure 21. Sensitivity bands in terms of velocity-averaged annihilation cross section as a function of DM particle mass, resulting from the max density profiles listed in Table 2 and the annihilation channels: $b\bar{b}$, W^+W^-, for different LMC emission models.
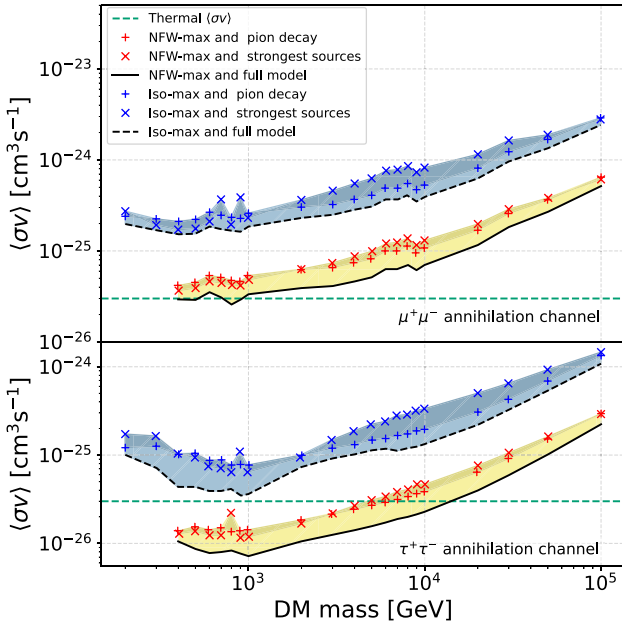
Figure 22. Same as Fig. 21 for the $\mu^+\mu^-$ and $\tau^+\tau^-$ annihilation channels.

detection. We therefore present the sensitivity curves in the shape of shaded bands, to illustrate the uncertainty on our knowledge of the actual composition of the LMC emission.

For the majority of models, the sensitivity bands lie above the canonical thermal cross section, which defines the range of WIMPs models which allow to recover the current DM density in the universe, and are considered canonical WIMPs. However, for channels with a higher integrated flux, like $\tau^+\tau^-$, and for the maximal version of the NFW profile, the sensitivity bands show that CTA could be able to

reach below the canonical cross-section parameter space in a range of masses around 1 TeV. A recent study on DM detection in the LMC using radio data (Regis et al. 2021) already excluded masses below 480 GeV for the $b\bar{b}$, W^+W^-, $\tau^+\tau^-$, $\mu^+\mu^-$ channels, but according to our results, CTA could extend those limits up to a few TeV, at least for some of the studied DM candidate models. These results are ideal because, among other things, we are assuming a perfect knowledge of the gamma-ray background emission, but still they point out that CTA observations of the LMC could be very useful to constrain the DM annihilation emission models.

Our forecast sensitivity is compatible with those inferred with a similar technique for other targets, for instance the GC as studied in Acharyya et al. (2021). Indeed, the possibility to detect DM in the LMC is weaker than in the GC, owing to the combined effect of the larger distance and shallower distribution (smaller J-factor) of the first with respect to the latter.

5 SUMMARY AND CONCLUSIONS

We simulated the observation and analysis of a 340 h survey of the LMC with CTA, based on an emission model comprising components for the four already known TeV point sources, the galaxy-scale interstellar emission, and mock populations of SNRs, PWNe, and pulsar halos. We also assessed prospects for the detectability of young remnant SN 1987A and star-forming region 30 Doradus, and we derived the constraints that can be obtained on the nature of dark matter from observing the massive halo of the LMC.

Known point sources PWN N 157B, SNR N 132D, HMXB LMC P3, and SB 30 Doradus C will be detected with very high significances over most of the 0.1–100 TeV range. The sensitivity of the CTA survey will allow for fine spectral studies and provide a meaningful extension of the spectra down to ∼100 GeV, thus allowing a reliable connection to the range probed with Fermi-LAT, and up to or beyond 10 TeV. Such a broad spectral coverage will be instrumental in characterizing the global particle acceleration efficiency, the respective contribution of different particle populations to the emission, and the maximum energies reached in these accelerators.

The young remnant from SN 1987A has not yet been detected in HE/VHE gamma-rays, so quantitative prospects are very much dependent on the assumed model for particle acceleration and its recent and future evolution. A simple model, informed by current constraints on the shock dynamics and the sub-GeV electron population, suggests that CTA could detect hadronic emission from a population of emitting nuclei whose spectrum flattens towards high energies up to power-law indices ∼2.0. A softer emission, as observed in many Galactic SNRs, could be within reach of the survey pending a flux increase by at least a factor of 3−4 over ∼2015−2035, which would trigger additional observations to get a meaningful spectral characterization.

Beyond known point sources or promising candidates, the survey should allow the detection of an additional half a dozen sources, typically with 1−10 TeV fluxes >2−3 × 10^{-14} erg cm^{-2} s^{-1}. Our source population model suggests that this sample would be dominated by pulsar-powered objects, and a couple of interacting SNRs. Source confusion may be an issue even for the small fraction of the source population accessible to the survey, with half of the simulated detections being found in locations where 2−3 bright sources overlap. Most sources will be detected as point-like objects, which will likely complicate their classification based on VHE observations alone.

Interstellar emission on the galaxy scale in the LMC is constrained by Fermi-LAT observations at 10–100 GeV, but its properties in the VHE remain essentially unexplored. Our baseline model for interstellar emission predicts that pion-decay dominates inverse-Compton radiation by at least an order of magnitude over the entire CTA range. If its spectrum extends from 10 GeV to higher energies with a rather soft photon index ∼2.7, it will remain mostly out of reach of the survey, except for the low-significance detection of emission over less than half a degree from the molecular ridge south of 30 Doradus. If the CR population in the LMC exhibits a spectral hardening above a few 100 GeV, as inferred from diffuse emission of the (innermost regions of the) MW and observed in the local flux of primary CR nuclei, and if this trend extends up to 10–100 TeV, then degree-scale interstellar pion-decay emission could be detected in the direction of major molecular cloud complexes, with high significance over the 0.1–10 TeV range.

Star-forming region 30 Doradus was not detected as a prominent and specific source in current GeV and TeV observations, but it has a clear potential for efficient production of CRs and HE/VHE radiation. In the framework of continuous injection of accelerated particles by 30 Doradus, followed by diffusion away from it, the region could be detected for acceleration efficiency of at least 40 per cent of the assumed ∼10^{39} erg s^{-1} mechanical power of the central stellar clusters. If diffusion in the <100 pc vicinity of the source is suppressed, the requirement on acceleration efficiency is relaxed down to below 1 per cent for diffusion suppression factors of a few hundreds. Detailed studies of such a target, including in particular a characterization of its intensity distribution, will however be challenging given the distance to the source and the need to separate it from foreground and background interstellar emission from the galaxy. Moreover, the survey sensitivity may not be sufficient to investigate the possible role of SFRs in producing PeV-scale galactic CRs.

Finally, prospects for the detection of a possible gamma-ray signal from DM annihilation were computed, harnessing the extended nature of the LMC, crucial to disentangle DM emission from a baryonic background, and its relatively high J-factor, comparable to other popular DM candidates such as dwarf spheroidals. Several DM density profiles, annihilation channels and particle masses have been tested on top of the baseline baryonic emission model for the LMC to compute the velocity-averaged annihilation cross-section required for detection. The majority of models lie about five to ten times above the canonical thermal cross-section, benchmark for self-annihilation in the case of WIMPs DM being a thermal relic. However, by adopting NFW density profiles, maximizing the DM density and still complying with the LMC rotation curves constraints, and annihilation channels yielding large integrated flux, like the $\tau^+\tau^-$ channel, the computed sensitivity reaches below the thermal cross section at ∼TeV energies, meaning these DM models could be detected or excluded by CTA, making the LMC a worthy candidate for DM searches.

The work introduced in this article provides a first quantitative assessment of the prospects opened by a deep survey of the LMC with CTA. It is rather optimistic in many assumptions, for instance data analysis methods relying exclusively on full spatial and spectral maximum likelihood approaches with perfect knowledge of the instrumental background distribution in the field of view. The material developed during this work should serve as a starting point for more detailed studies, for instance assessing the impact of alternative data analysis methods or refining the prospects for specific sources such as SN 1987A by comparing more advanced and dedicated models to the sensitivity curves provided here.

DATA AVAILABILITY

The full galaxy emission model developed in this work can be provided on request by the corresponding authors of the article. The tools for simulating the survey observations and analysing the resulting data are publicly available at http://cta.irap.omp.eu/ctools/index.html, and the instrument response functions can be downloaded from https://zenodo.org/record/5499840#.Y9D4nvGZMbY.

REFERENCES

Abdalla H. et al., 2018a, A&A, 610, L17
Abdalla H. et al., 2018b, A&A, 612, A1
Abdalla H. et al., 2018c, A&A, 612, A2
Abdalla H. et al., 2018d, A&A, 617, A73
Abdo A. A. et al., 2008, Science, 322, 1218
Abdo A. A. et al., 2010a, A&A, 512, A7 +
Abdo A. A. et al., 2010b, A&A, 523, A46 +
Abeysekara A. U. et al., 2017, Science, 358, 911
Abeysekara A. U. et al., 2019, ApJ, 881, 134
Abramowski A. et al., 2012, A&A, 545, L2
Abramowski A. et al., 2014, Phys. Rev. D, 90, 122007
Abramowski A. et al., 2015, Science, 347, 406
Acciari V. A. et al., 2009, Nature, 462, 770
Acero F. et al., 2009, Science, 326, 1080
Acero F. et al., 2016, ApJS, 224, 8
Acharyya A. et al., 2021, J. Cosmol. Astropart. Phys., 2021, 057
Ackermann M. et al., 2012, ApJ, 755, 164
Ackermann M. et al., 2015, Science, 350, 801
Ackermann M. et al., 2016, A&A, 586, A71
Ackermann M. et al., 2017, ApJ, 836, 208
Aguilar M. et al., 2015a, Phys. Rev. Lett., 114, 171103
Aguilar M. et al., 2015b, Phys. Rev. Lett., 115, 211101
Aguilar M. et al., 2017, Phys. Rev. Lett., 119, 251101
Aguilar M. et al., 2020, Phys. Rev. Lett., 124, 211102
Aharonian F., Yang R., de Oña Wilhelmi E., 2019, Nat. Astron., 3, 561
Ajello M., Di Mauro M., Paliya V. S., Garrappa S., 2020, ApJ, 894, 88
Albert A. et al., 2020, ApJ, 905, 76
Amenomori M. et al., 2021, Phys. Rev. Lett., 126, 141101
An Q. et al., 2019, Sci. Adv., 5, eaax3793
Ansoldi S. et al., 2016, A&A, 585, A133
Atoyan A. M., Aharonian F. A., Völk H. J., 1995, Phys. Rev. D, 52, 3265
Bamba A., Ueno M., Nakajima H., Koyama K., 2004, ApJ, 602, 257
Bamba A., Ueno M., Nakajima H., Mori K., Koyama K., 2006, A&A, 450, 585
Bamba A. et al., 2018, ApJ, 854, 71
Banas K. R., Hughes J. P., Bronfman L., Nyman L. Å., 1997, ApJ, 480, 607
Barger K. A., Lehner N., Howk J. C., 2016, ApJ, 817, 91
Bartoli B. et al., 2015, ApJ, 806, 20
Bell A. R., Schure K. M., Reville B., Giacinti G., 2013, MNRAS, 431, 415
Berezhko E. G., Ellison D. C., 1999, ApJ, 526, 385
Berezhko E. G., Ksenofontov L. T., Völk H. J., 2011, ApJ, 732, 58
Berezhko E. G., Ksenofontov L. T., Völk H. J., 2015, ApJ, 810, 63
Bernard J.-P. et al., 2008, AJ, 136, 919
Bertone G., ed., 2010, Particle Dark Matter: Observations, Models and Searches. Cambridge Univ. Press, Cambridge
Blais D., Kiefer C., Polarski D., 2002, Phys. Lett., B535, 11
Blasi P., Amato E., 2012, J. Cosmol. Astropart. Phys., 2012, 010
Blumenthal G. R., Gould R. J., 1970, Rev. Mod. Phys., 42, 237
Bonnivard V., Hütten M., Nezri E., Charbonnier A., Combet C., Maurin D., 2016, Comput. Phys. Commun., 200, 336
Borkowski K. J., Hendrick S. P., Reynolds S. P., 2007, ApJ, 671, L45
Boyarsky A., Ruchayskiy O., Shaposhnikov M., 2009, Ann. Rev. Nucl. Part. Sci., 59, 191
Bozzetto L. M. et al., 2017, ApJS, 230, 2
Brahimi L., Marcowith A., Ptuskin V. S., 2020, A&A, 633, A72
Buckley M. R., Charles E., Gaskins J. M., Brooks A. M., Drlica-Wagner A., Martin P., Zhao G., 2015, Phys. Rev., D91, 102001
Bustard C., Zweibel E. G., 2021, ApJ, 913, 106
Bustard C., Zweibel E. G., D'Onghia E., Gallagher J. S. I., Farber R., 2020, ApJ, 893, 29
Butt Y. M., Bykov A. M., 2008, ApJ, 677, L21

Bykov A. M., 2001, Space Sci. Rev., 99, 317
Bykov A. M., Ellison D. C., Gladilin P. E., Osipov S. M., 2018, Adv. Space Res., 62, 2764
Bykov A. M., Marcowith A., Amato E., Kalyashova M. E., Kruijssen J. M. D., Waxman E., 2020, Space Sci. Rev., 216, 42
Bœhm C., Fayet P., 2004, Nuc. Phys. B, 683, 219
Callingham J. R. et al., 2016, MNRAS, 462, 290
Caprioli D., Haggerty C., 2019, In Proc. 36th International Cosmic Ray Conference (ICRC2019). p. 209, preprint (arXiv:1909.06288)
Caprioli D., Haggerty C. C., Blasi P., 2020, ApJ, 905, 2
Cash W., 1979, ApJ, 228, 939
Cataldo M., Pagliaroli G., Vecchiotti V., Villante F. L., 2019, J. Cosmol. Astropart. Phys., 2019, 050
Cerri S. S., Gaggero D., Vittino A., Evoli C., Grasso D., 2017, J. Cosmol. Astropart. Phys., 10, 019
Charbonnier A., Combet C., Maurin D., 2012, Computer Phys. Commun., 183, 656
Chen Y., Wang Q. D., Gotthelf E. V., Jiang B., Chu Y.-H., Gruendl R., 2006, ApJ, 651, 237
Cheng Y., Wang Q. D., Lim S., 2021, MNRAS, 504, 1627
Cherenkov Telescope Array Consortium et al., 2019, Science with the Cherenkov Telescope Array. World Scientific Publishing Co. Pte. Ltd.
Ciafaloni P., Comelli D., Riotto A., Sala F., Strumia A., Urbano A., 2011, J. Cosmol. Astropart. Phys., 2011, 019
Cirelli M. et al., 2011, J. Cosmol. Astropart. Phys., 2011, 051
Cole A. A., Tolstoy E., Gallagher John S. I., Smecker-Hane T. A., 2005, AJ, 129, 1465
Corbet R. H. D. et al., 2016, ApJ, 829, 105
Cowan G., Cranmer K., Gross E., Vitells O., 2011, Eur. Phys. J. C, 71, 1554
Cristofari P., Gabici S., Casanova S., Terrier R., Parizot E., 2013, MNRAS, 434, 2748
D'Angelo M., Blasi P., Amato E., 2016, Phys. Rev. D, 94, 083003
D'Angelo M., Morlino G., Amato E., Blasi P., 2018, MNRAS, 474, 1944
de Avillez M. A., Breitschwerdt D., 2004, A&A, 425, 899
Drury L. O., Voelk J. H., 1981, ApJ, 248, 344
Dubus G., 2013, A&AR, 21, 64
Dunne B. C., Points S. D., Chu Y.-H., 2001, ApJS, 136, 119
Dwarkadas V. V., 2013, MNRAS, 434, 3368
Eichler D., 1984, ApJ, 277, 429
Evoli C., Gaggero D., Grasso D., Maccione L., 2012, Phys. Rev. Lett., 108, 211102
Evoli C., Aloisio R., Blasi P., 2019, Phys. Rev. D, 99, 103023
Ferrand G., Marcowith A., 2010, A&A, 510, A101
Fukui Y. et al., 2008, ApJS, 178, 56
Gaensler B. M., Hendrick S. P., Reynolds S. P., Borkowski K. J., 2003, ApJ, 594, L111
Gaensler B. M., Haverkorn M., Staveley-Smith L., Dickey J. M., McClure-Griffiths N. M., Dickel J. R., Wolleben M., 2005, Science, 307, 1610
Gaggero D., Urbano A., Valli M., Ullio P., 2015a, Phys. Rev. D, 91, 083012
Gaggero D., Grasso D., Marinelli A., Urbano A., Valli M., 2015b, ApJ, 815, L25
Gaustad J. E., McCullough P. R., Rosing W., Van Buren D., 2001, PASP, 113, 1326
Greco E. et al., 2021, ApJ, 908, L45
H.E.S.S. Collaboration, 2018, A&A, 617, A73
H.E.S.S. Collaboration, 2021, A&A, 655, A7
Harris J., Zaritsky D., 2009, AJ, 138, 1243
Hendrick S. P., Reynolds S. P., 2001, ApJ, 559, 903
Hu W., Barkana R., Gruzinov A., 2000, Phys. Rev. Lett., 85, 1158
Hughes A., Staveley-Smith L., Kim S., Wolleben M., Filipović M., 2007, MNRAS, 382, 543
Hütten M., Combet C., Maurin D., 2019, Comput. Phys. Commun., 235, 336
Jacyszyn-Dobrzeniecka A. M. et al., 2016, AcA, 66, 149
James P. A., Ivory C. F., 2011, MNRAS, 411, 495
Jaskot A. E., Strickland D. K., Oey M. S., Chu Y. H., García-Segura G., 2011, ApJ, 729, 28
Kafexhiu E., Aharonian F., Taylor A. M., Vila G. S., 2014, Phys. Rev. D, 90, 123014
Kavanagh P. J., Sasaki M., Bozzetto L. M., Filipović M. D., Points S. D., Maggi P., Haberl F., 2015, A&A, 573, A73
Kavanagh P. J. et al., 2019, A&A, 621, A138
Kelner S. R., Aharonian F. A., Bugayov V. V., 2006, Phys. Rev. D, 74, 034018
Kim S., Staveley-Smith L., Dopita M. A., Freeman K. C., Sault R. J., Kesteven M. J., McConnell D., 1998, ApJ, 503, 674
Kim S., Dopita M. A., Staveley-Smith L., Bessell M. S., 1999, AJ, 118, 2797
Kim S., Staveley-Smith L., Dopita M. A., Sault R. J., Freeman K. C., Lee Y., Chu Y.-H., 2003, ApJS, 148, 473
Kirk J. G., Duffy P., Gallant Y. A., 1996, A&A, 314, 1010
Knödlseder J. et al., 2016, A&A, 593, A1
Knödlseder J. et al., 2019, A&A, 632, A102
Komin N., Haupt M., H.E.S.S. Collaboration, 2019, In Proc. 36th International Cosmic Ray Conference (ICRC2019). p. 716, preprint (arXiv:1908.04656)
Krause M. G. H., Diehl R., 2014, ApJ, 794, L21
Krumholz M. R., Crocker R. M., Xu S., Lazarian A., Rosevear M. T., Bedwell-Wilson J., 2020, MNRAS, 493, 2817
Lapenna E., Mucciarelli A., Origlia L., Ferraro F. R., 2012, ApJ, 761, 33
Law C. J. et al., 2020, ApJ, 894, 73
Le Marne A. E., 1968, MNRAS, 139, 461
Leahy D. A., 2017, ApJ, 837, 36
Linden T., Auchettl K., Bramante J., Cholis I., Fang K., Hooper D., Karwal T., Li S. W., 2017, Phys. Rev. D, 96, 103016
Lipari P., Vernetto S., 2018, Phys. Rev. D, 98, 043003
Liu L., Gerke B. F., Wechsler R. H., Behroozi P. S., Busha M. T., 2011, ApJ, 733, 62
Lorimer D. R. et al., 2006, MNRAS, 372, 777
Lucke P. B., Hodge P. W., 1970, AJ, 75, 171
Luks T., Rohlfs K., 1992, A&A, 263, 41
Mac Low M.-M., McCray R., 1988, ApJ, 324, 776
Maggi P. et al., 2016, A&A, 585, A162
Malkov M. A., Diamond P. H., Sagdeev R. Z., Aharonian F. A., Moskalenko I. V., 2013, ApJ, 768, 73
Marshall F. E., Gotthelf E. V., Zhang W., Middleditch J., Wang Q. D., 1998, ApJ, 499, L179
Martin J., Torres D. F., Cillis A., de Oña Wilhelmi E., 2014, MNRAS, 443, 138
Martin P., Marcowith A., Tibaldo L., 2022a, A&A, 665, A132
Martin P., Tibaldo L., Marcowith A., Abdollahi S., 2022b, A&A, 666, A7
Mathewson D. S., Ford V. L., Tuohy I. R., Mills B. Y., Turtle A. J., Helfand D. J., 1985, ApJS, 58, 197
Maurin G., Marcowith A., Komin N., Krayzel F., Lamanna G., 2016, A&A, 591, A71
Mayer M., Brucker J., Holler M., Jung I., Valerius K., Stegmann C., 2012, preprint (arXiv:1202.1455)
McEntaffer R. L., Brantseg T., Presley M., 2012, ApJ, 756, 17
Micelotta E. R., Brandl B. R., Israel F. P., 2009, A&A, 500, 807
Mills B. Y., Turtle A. J., 1984, in van den Bergh S., de Boer K. S. D., eds, Structure and Evolution of the Magellanic Clouds, Vol. 108. p. 283
Mizuno N. et al., 2001, PASJ, 53, 971
Mori M., 2009, Astropart. Phys., 31, 341
Morlino G., Blasi P., Peretti E., Cristofari P., 2021, MNRAS, 504, 6096
Nava L., Gabici S., Marcowith A., Morlino G., Ptuskin V. S., 2016, MNRAS, 461, 3552
Nava L., Recchia S., Gabici S., Marcowith A., Brahimi L., Ptuskin V., 2019, MNRAS, 484, 2684
Navarro J. F., Frenk C. S., White S. D. M., 1996, ApJ, 462, 563
Neronov A., Semikoz D., 2020, A&A, 633, A94
Ng C. Y., Zanardo G., Potter T. M., Staveley-Smith L., Gaensler B. M., Manchester R. N., Tzioumis A. K., 2013, ApJ, 777, 131
Orlando E., 2018, MNRAS, 475, 2724
Paradis D., Paladini R., Noriega-Crespo A., Lagache G., Kawamura A., Onishi T., Fukui Y., 2011, ApJ, 735, 6
Parizot E., Marcowith A., van der Swaluw E., Bykov A. M., Tatischeff V., 2004, A&A, 424, 747
Pellegrini E. W., Oey M. S., Winkler P. F., Points S. D., Smith R. C., Jaskot A. E., Zastrow J., 2012, ApJ, 755, 40

Pennock C. M. et al., 2021, MNRAS, 506, 3540
Peretti E., Blasi P., Aharonian F., Morlino G., 2019, MNRAS, 487, 168
Persic M., Rephaeli Y., 2022, A&A, 666, A167
Petruk O., Orlando S., Miceli M., Bocchino F., 2017, A&A, 605, A110
Pietrzyński G. et al., 2013, Nature, 495, 76
Pothast M., Gaggero D., Storm E., Weniger C., 2018, J. Cosmol. Astropart. Phys., 10, 045
Potter T. M., Staveley-Smith L., Reville B., Ng C. Y., Bicknell G. V., Sutherland R. S., Wagner A. Y., 2014, ApJ, 794, 174
Ptuskin V. S., Zirakashvili V. N., 2003, A&A, 403, 1
Ptuskin V. S., Zirakashvili V. N., 2005, A&A, 429, 755
Recchia S., Blasi P., Morlino G., 2016, MNRAS, 462, L88
Regis M. et al., 2021, J. Cosmol. Astropart. Phys., 2021, 046
Remy Q., Tibaldo L., Acero F., Fiori M., Knödlseder J., Olmi B., Sharma P., 2022, In Proc. 37th International Cosmic Ray Conference. p. 886, preprint (arXiv:2109.03729)
Ridley J. P., Lorimer D. R., 2010, MNRAS, 406, L80
Sabbi E. et al., 2012, ApJ, 754, L37
Sano H. et al., 2015, ASP Conf. Ser., Revealing the Large-Scale Structures of Interstellar Gas Associated with the Magellanic SNR N132D, Vol. 499. Astron. Soc. Pac., San Francisco, p. 257
Sasaki M. et al., 2022, A&A, 661, A37
Schneider F. R. N. et al., 2018, A&A, 618, A73
Seward F. D., Charles P. A., Foster D. L., Dickel J. R., Romero P. S., Edwards Z. I., Perry M., Williams R. M., 2012, ApJ, 759, 123
Sofue Y., 1999, PASJ, 51, 445
Sofue Y., 2013, Mass Distribution and Rotation Curve in the Galaxy. p. 985
Staveley-Smith L., Kim S., Calabretta M. R., Haynes R. F., Kesteven M. J., 2003, MNRAS, 339, 87
Strong A. W., Porter T. A., Digel S. W., Jóhannesson G., Martin P., Moskalenko I. V., Murphy E. J., Orlando E., 2010, ApJ, 722, L58
Sturm E. et al., 2011, ApJ, 733, L16
Subramanian S., Subramaniam A., 2010, A&A, 520, A24
Sudoh T., Linden T., Beacom J. F., 2019, Phys. Rev. D, 100, 043016
Testor G., Schild H., Lortet M. C., 1993, A&A, 280, 426
Tibaldo L., Gaggero D., Martin P., 2021, Universe, 7, 141
Trotta R., Jóhannesson G., Moskalenko I. V., Porter T. A., Ruiz de Austri R., Strong A. W., 2011, ApJ, 729, 106
van den Bergh S., 1991, Phys. Rep., 204, 385
van der Marel R. P., Alves D. R., Hardy E., Suntzeff N. B., 2002, AJ, 124, 2639
van Soelen B., Komin N., Kniazev A., Väisänen P., 2019, MNRAS, 484, 4347
van der Marel R. P., Kallivayalil N., 2014, ApJ, 781, 121
Veilleux S., Cecil G., Bland-Hawthorn J., 2005, ARA&A, 43, 769
Vink J., Simoni R., Komin N., Prokhorov D., 2021, In Proc. 37th International Cosmic Ray Conference. p. 778, preprint (arXiv:2107.10946)
Walborn N. R. et al., 2014, A&A, 564, A40
Weaver R., McCray R., Castor J., Shapiro P., Moore R., 1977, ApJ, 218, 377
Wilks S. S., 1938, Ann. Math. Statist., 9, 60
Yamaguchi H., Bamba A., Koyama K., 2009, PASJ, 61, S175
Yamaguchi H., Sawada M., Bamba A., 2010, ApJ, 715, 412
Zabalza V., 2015, In Proc. 34th International Cosmic Ray Conference (ICRC2015). p. 922, preprint (arXiv:1509.03319)
Zanardo G. et al., 2010, ApJ, 710, 1515
Zhang L., Chen S. B., Fang J., 2008, ApJ, 676, 1210
Zhao H., 1996, MNRAS, 278, 488
Zhekov S. A., Park S., McCray R., Racusin J. L., Burrows D. N., 2010, MNRAS, 407, 1157

APPENDIX A: CR SOURCE DISTRIBUTION

Models for interstellar emission on a galactic scale were computed under the assumption of diffusion-loss transport in a uniform model of the ISM of CRs steadily injected from an ensemble of point sources. As a tracer for sites of CR injection related to the massive star population, we used a selection of H II regions from the catalogue of Pellegrini et al. (2012), which covers the entire galaxy and provides

an indirect mean to determine the membership distribution of young star clusters.

We restricted our selection to regions with H α luminosities above 10^{37} erg s^{-1}, a limit below which the H α luminosity function flattens as a result of stochastic ionizing populations; hence, a regime where our assumption of steady CR injection would be less and less valid. For reference, Pellegrini et al. (2012) indicate that an H α luminosity of 10^{37} erg s^{-1} corresponds to the Orion Nebula, which harbours a single O6.5 V star. Above this value, the luminosity function is close to a power law with a slope of -1.8 and extends up to the tremendous $10^{39.66}$ erg s^{-1} luminosity of the 30 Doradus region that is ionized by hundreds of O stars in cluster R136a. This object is literally extraordinary, even beyond LMC and within the Local Group, and actually dominates the output of the galaxy. In our model, we handled it separately from the rest of star clusters for three reasons: (i) including it as any other star cluster in a distribution of CR sources would result in CR injection and the related gamma-ray emission to be strongly concentrated in 30 Doradus, which may too favourably bias detection prospects; (ii) although there is some age spread over the region, most OB stars are young with ages <5Myr (Schneider et al. 2018), so it may well be that only very few SNe exploded in the recent past, hence a limited CR injection (see also Harris & Zaritsky 2009, about the very recent increase in star formation of 30 Doradus); and (iii) supporting the previous point, 30 Doradus is not conspicuous at GeV energies, at least not in proportion to its H α emission (Ackermann et al. 2016).

For all 138 remaining regions in our sample, we converted H α luminosity into ionizing luminosities, applying a correction for LyC radiation escape using the morphological classification and escape fraction determined by Pellegrini et al. (2012). We took ionizing luminosity as a measure of the richness of each star cluster, to which we assumed CR injection power is proportional. There are several caveats to this approach: while some proportionality between ionizing and CR injection powers can be expected in the limit of continuous and high star formation rate and CR acceleration by SNe only, the relationship is most likely subject to variations when one includes effects such as finite sampling of the initial mass function, stellar age spread, collective acceleration processes given the actual stellar cluster substructure, etc. Another caveat is that such a relation does not hold for the contribution from thermonuclear SNe, whose rate is relatively high in the LMC compared to that integrated over larger volumes and durations in the local Universe (by about a factor of two; see Maggi et al. 2016). This is most likely an effect of the actual star formation history of the LMC over the past 2 Gyr, which leads to a relatively high rate of thermonuclear SNe now. The spatial distribution of thermonuclear SNe will be less appropriately traced by H II regions, but we checked that adopting a less concentrated and more uniform distribution of CR sources does not affect our conclusions on the detectability of large-scale interstellar emission.

APPENDIX B: CR PROPAGATION

For large-scale interstellar emission, we consider that CR transport away from injection sites proceeds by spatial diffusion limited by energy losses, in a medium with homogeneous and isotropic properties. We solved the diffusion-loss equation for a point-like and stationary source following Atoyan, Aharonian & Völk (1995). The spectral density at radius r from the source and time t since injection start is obtained from

$$\frac{dN}{dE\,dV}(r, E, t) = \int_{t_{inj}}^{t} \frac{\dot{E}(E_0)}{\dot{E}(E)} \frac{Q(E_0)}{\pi^{3/2} r_{diff}^3} e^{-r^2/r_{diff}^2}\,dt_0 \qquad \text{(B1)}$$

where E_0 is the initial particle energy at injection time t_0 and integration runs over injection history. The earliest possible injection time t_{inj} is computed from the maximum cooling time from cut-off energy E_{cut} down to current energy E:

$$t_{inj}(E, t) = \max([0, t - t_{cool}(E_{cut}, E)]), \tag{B2}$$

$$t_{cool}(E_{cut}, E) = \int_E^{E_{cut}} \frac{de}{\dot{E}(e)}, \tag{B3}$$

while the diffusion radius r_{diff} is computed from diffusion coefficient D and energy loss rate $\dot{E}$:

$$r_{diff}(E_0, E) = 2 \left[\int_E^{E_0} \frac{D(e)}{\dot{E}(e)} \, de \right]^{1/2}. \tag{B4}$$

Proton and electron spatial distributions around the stationary source are computed by integrating over an injection duration of $t = 100\,\mathrm{Myr}$, instead of computing an exact steady-state solution. This accounts for the fact that the star formation history of the LMC was not steady over recent times, and in particular exhibits a drop in star formation at 100 Myr in most regions (but this has limited impact at the very high energies probed with CTA, at which particles diffuse on time-scales smaller than this assumed injection duration). The above solution implicitly assumes a zero density at infinity. If the extent of the diffusion region across the galaxy has a finite value, it should in principle be possible to retrieve a similar predicted emission by assuming a smaller diffusion coefficient (for diffusion-dominated transport).

APPENDIX C: INTERSTELLAR RADIATION FIELDS

The model for the ISRF was developed from the work of Paradis et al. (2011), in which the broadband infrared dust emission of the LMC was linearly decomposed into gas phases, eventually yielding dust emissivity spectra $Q_Y(\nu)$ per unit column density for each phase Y. The level of stellar radiation heating the dust was obtained from fits of these emissivities with predictions from the *DustEM* dust emission model under two different assumptions for the stellar field: dust in the molecular and atomic phases is exposed to a radiation field characteristic of the solar neighbourhood, $R^{Mathis}(\nu)$, while dust in the ionized phase is heated by a radiation field more appropriate to the vicinity of massive star clusters, $R^{GALEV}(\nu)$. For our purposes, we retained for our baseline model the results for the regime defined as 'typical H II regions' in the article (case 2), which covers most of the LMC disk and is thus appropriate for an average ISRF model on large scales.

In practice, infrared emissivities were scaled by gas column densities defined below, while stellar radiation fields were renormalized by the fitting factors r given in table 2 of Paradis et al. (2011) and further scaled by filling factors f_X for their respective gas phase X, ionized i or neutral n (atomic and molecular are grouped because the filling factor of the molecular phase is small compared to the atomic and ionized phases). The interstellar radiation spectral energy density $U(\nu)$ is the sum of components arising from stars and dust, plus the cosmic microwave background. It reads

$$U(\nu) = U_{dust}(\nu) + U_{stars}(\nu) + U_{CMB}(\nu), \tag{C1}$$

$$U_{dust}(\nu) = \frac{4\pi}{c} \left[N_{H\,I} Q_{H\,I}(\nu) + N_{H_2} Q_{H_2}(\nu) + N_{H\,II} Q_{H\,II}(\nu) \right], \tag{C2}$$

$$U_{stars}(\nu) = \frac{4\pi}{c} \left[r_i f_i R^{GALEV}(\nu) + r_n f_n R^{Mathis}(\nu) \right], \tag{C3}$$

with $f_i = f_n = 0.5$ (de Avillez & Breitschwerdt 2004). U_{CMB} is the radiation spectral energy density of the cosmic microwave background. The average hydrogen column densities for the atomic, molecular, and ionized phases are obtained from the gas masses and gas disc geometry assumed in Section 2.3:

$$N_{H\,I} = 1.85 \times 10^{21} \, \mathrm{H\,cm^{-2}}, \tag{C4}$$

$$N_{H_2} = 2.43 \times 10^{20} \, \mathrm{H\,cm^{-2}}, \tag{C5}$$

$$N_{H\,II} = 5.48 \times 10^{19} \, \mathrm{H\,cm^{-2}}. \tag{C6}$$

An alternative ISRF model, as part of the so-called gas-rich ISM model, was also developed assuming an average neutral gas column density ten times the average given above, while the ionized gas column density becomes $6.18 \times 10^{20} \, \mathrm{H\,cm^{-2}}$, as computed following Paradis et al. (2011), using electron density $n_e = 3.98 \, \mathrm{cm^{-3}}$, and an H α intensity of 113.3 Rayleigh corresponding to the limit between 'typical H II regions' and 'very bright H II regions' in the article.

APPENDIX D: HARDER INTERSTELLAR EMISSION

Analysis of the Galactic diffuse emission observed with Fermi-LAT in the 0.1–100 GeV range suggests a progressive increase in density and hardening of the spectrum of $\sim 10-100\,\mathrm{GeV}$ CRs as we move from outer to inner regions of the Milky Way, with a peak at galactocentric radii of a few kpc, the molecular ring position, which is also where the largest density of CR sources are expected to be found (Ackermann et al. 2012; Acero et al. 2016; Pothast et al. 2018). The typical spectral hardening of $\sim 0.2-0.4$ in power-law index can be explained by position-dependent transport properties (Evoli et al. 2012; Gaggero et al. 2015b; Recchia, Blasi & Morlino 2016; Cerri et al. 2017). In several of these works, CR source density is an important if not the main driver of CR transport properties, either directly, in producing efficient self-confinement, or indirectly, in generating perpendicular outflows and/or magnetic field topologies, with the result that regions harbouring a larger number of CR sources are associated with harder gamma-ray emission. With a supernova activity ~ 10 times lower than the Milky Way in a volume $\sim 30-40$ times smaller, the above effects could to some extent be at play in the LMC and produce an average pion-decay emission harder than assumed in our baseline model.

It is not clear, however, how this extrapolates to higher energies, especially those probed with CTA. Theoretically, different scenarios for the origin of the inferred hard spectrum of $\sim 10-100\,\mathrm{GeV}$ CRs in the inner Galaxy predict different behaviours at higher energies. Self-confinement, strongly suppressing diffusion and allowing advection to become a more dominant transport process (Recchia et al. 2016), is expected to cease above $\sim 100\,\mathrm{GeV}$, where the CR flux is too weak to excite significant turbulence; higher energy particles would thus enter a regime of diffusive transport in externally driven turbulence (Blasi & Amato 2012), which would soften their spectrum compared to a more advection-dominated regime at lower energies. Alternatively, anisotropic diffusion, with predominant parallel diffusion off the plane in the inner regions, would preserve a hard spectrum in the inner Galactic regions at higher energies.

Observationally, evidence for a hardening seems to extend to at least sub-TeV gamma-rays (Pothast et al. 2018; Neronov & Semikoz 2020). At higher energies, the body of available information grows rapidly (Abdo et al. 2008; Abramowski et al. 2014; Bartoli et al. 2015; Amenomori et al. 2021), but instrumental and data analysis challenges make it difficult to firmly establish the spectrum of diffuse

emission of purely interstellar origin (the main difficulties being background rejection, proper determination of individual source extension, and uncertain contribution from unresolved sources). The authors of Neronov & Semikoz (2020) inferred a hard gamma-ray spectrum at sub-TeV energies even in outer regions of the Galaxy, and Pothast et al. (2018) reports a systematically harder emission at all Galactocentric radii in the ≥ 30 GeV range. This suggests the possibility that hard spectra of CRs may be rather universal throughout most of the Galactic disk, which seems consistent with the hardening above $200 - 300$ GV observed in the spectra of the local flux of primary CR nuclei (Aguilar et al. 2015a, b, 2017; Aguilar et al. 2020), at least up to about 10 TeV (An et al. 2019).

Another piece of evidence for hard gamma-ray emission on galactic scales, hence possibly a hard interstellar population of CRs, comes from starburst galaxies. Hard spectra in the GeV range were measured (Ajello et al. 2020) and extend all the way up to the TeV range for a few starburst galaxies (Acciari et al. 2009; H.E.S.S. Collaboration et al. 2018). These are admittedly extreme in their interstellar conditions and not representative of the LMC; yet the very origin of the hard spectra remains unclear: they could be due to advection being the dominant transport mechanism up to very high energies (Peretti et al. 2019), or to a diffusion scheme specific to the actual interstellar conditions (Krumholz et al. 2020). To what extent one or the other scenario applies to the LMC is unknown. About possible advection in a galactic wind, a large-scale multiphase outflow was detected in the LMC on both near and far sides of the galaxy (Barger, Lehner & Howk 2016), with a velocity ~ 100 km s^{-1} that is on the low end of characteristic velocities for starburst-driven wind originating in star formation (Veilleux, Cecil & Bland-Hawthorn 2005; Sturm et al. 2011). Such an outflow can actually be driven by the CR population of the galaxy (see Bustard et al. 2020, for one among many recent developments on the topic), but whatever its origin, it has the potential to shape the spatial and spectral distribution of CRs in the galaxy depending on the actual values of other parameters governing CR transport in the ISM.

[1]*University of Alabama, Tuscaloosa, Department of Physics and Astronomy, Gallalee Hall, Box 870324 Tuscaloosa, AL 35487, USA*

[2]*Laboratoire Lagrange, Université Côte d'Azur, Observatoire de la Côte d'Azur, CNRS, Blvd de l'Observatoire, CS 34229, F-06304 Nice Cedex 4, France*

[3]*Laboratoire Leprince-Ringuet, CNRS/IN2P3, École polytechnique, Institut Polytechnique de Paris, F-91120 Palaiseau, France*

[4]*Departament de Física Quàntica i Astrofísica, Institut de Ciències del Cosmos, Universitat de Barcelona, IEEC-UB, Martí i Franquès, 1, E-08028, Barcelona, Spain*

[5]*Instituto de Astrofísica de Andalucía-CSIC, Glorieta de la Astronomía s/n, E-18008 Granada, Spain*

[6]*Instituto de Física Teórica UAM/CSIC and Departamento de Física Teórica, Universidad Autónoma de Madrid, c/ Nicolás Cabrera 13-15, Campus de Cantoblanco UAM, E-28049 Madrid, Spain*

[7]*Pontificia Universidad Católica de Chile, Av. Libertador Bernardo O'Higgins 340 Santiago, Chile*

[8]*Gran Sasso Science Institute (GSSI), Viale Francesco Crispi 7, I-67100 L'Aquila, Italy; and INFN-Laboratori Nazionali del Gran Sasso (LNGS), via G. Acitelli 22, I-67100 Assergi (AQ), Italy*

[9]*INAF – Osservatorio Astrofisico di Arcetri, Largo E. Fermi 5, I-50125 Firenze, Italy*

[10]*TÜBİTAK Research Institute for Fundamental Sciences, 41470 Gebze, Kocaeli, Turkey*

[11]*INFN Sezione di Napoli, Via Cintia, ed. G, I-80126 Napoli, Italy*

[12]*INFN Sezione di Padova and Università degli Studi di Padova, Via Marzolo 8, I-35131 Padova, Italy*

[13]*Institute for Cosmic Ray Research, University of Tokyo, 5-1-5, Kashiwa-no-ha, Kashiwa, Chiba 277-8582, Japan*

[14]*Kapteyn Astronomical Institute, University of Groningen, Landleven 12, NL-9747 AD, Groningen, Netherlands*

[15]*Department of Physics, Chemistry & Material Science, University of Namibia, Private Bag 13301, Windhoek 10005, Namibia*

[16]*Centre for Space Research, North-West University, Potchefstroom 2520, South Africa*

[17]*Universität Hamburg, Institut für Experimentalphysik, Luruper Chaussee 149, D-22761 Hamburg, Germany*

[18]*School of Physics and Astronomy, Monash University, Melbourne, Victoria 3800, Australia*

[19]*Department of Astronomy, University of Geneva, Chemin d'Ecogia 16, CH-1290 Versoix, Switzerland*

[20]*Université Paris-Saclay, Université Paris Cité, CEA, CNRS, AIM, F-91191 Gif-sur-Yvette Cedex, France*

[21]*Department of Physics, Graduate School of Science, The University of Tokyo, 7-3-1 Hongo, Bunkyo-ku, Tokyo 113-0033, Japan*

[22]*Research Center for the Early Universe, School of Science, The University of Tokyo, 7-3-1 Hongo, Bunkyo-ku, Tokyo 113-0033, Japan*

[23]*IPARCOS-UCM, Instituto de Física de Partículas y del Cosmos, and EMF-TEL Department, Universidad Complutense de Madrid, E-28040 Madrid, Spain*

[24]*Faculty of Science and Technology, Universidad del Azuay, Cuenca, Ecuador*

[25]*Deutsches Elektronen-Synchrotron, Platanenallee 6, D-15738 Zeuthen, Germany*

[26]*Centro Brasileiro de Pesquisas Físicas, Rua Xavier Sigaud 150, RJ 22290-180, Rio de Janeiro, Brazil*

[27]*Instituto de Astrofísica de Canarias and Departamento de Astrofísica, Universidad de La Laguna, E-38200 La Laguna, Tenerife, Spain*

[28]*Institut für Theoretische Physik, Lehrstuhl IV: Plasma-Astroteilchenphysik, Ruhr-Universität Bochum, Universitätsstraße 150, D-44801 Bochum, Germany*

[29]*Center for Astrophysics | Harvard & Smithsonian, 60 Garden St, Cambridge, MA 02138, USA*

[30]*CIEMAT, Avda. Complutense 40, E-28040 Madrid, Spain*

[31]*Max-Planck-Institut für Physik, Föhringer Ring 6, D-80805 München, Germany*

[32]*INFN Sezione di Perugia and Università degli Studi di Perugia, Via A. Pascoli, I-06123 Perugia, Italy*

[33]*Pidstryhach Institute for Applied Problems in Mechanics and Mathematics NASU, 3B Naukova Street, Lviv 79060, Ukraine*

[34]*Univ. Savoie Mont Blanc, CNRS, Laboratoire d'Annecy de Physique des Particules – IN2P3, F-74000 Annecy, France*

[35]*Center for Astrophysics and Cosmology (CAC), University of Nova Gorica, SI-5000 Nova Gorica, Slovenia*

[36]*INAF – Osservatorio Astronomico di Roma, Via di Frascati 33, I-00040, Monteporzio Catone, Italy*

[37]*ETH Zürich, Institute for Particle Physics and Astrophysics, Otto-Stern-Weg 5, CH-8093 Zürich, Switzerland*

[38]*INFN Sezione di Bari, via Orabona 4, I-70126 Bari, Italy*

[39]*Politecnico di Bari, via Orabona 4, I-70124 Bari, Italy*

[40]*INAF – Osservatorio Astronomico di Palermo 'G.S. Vaiana', Piazza del Parlamento 1, I-90134 Palermo, Italy*

[41]*Nicolaus Copernicus Astronomical Center, Polish Academy of Sciences, ul. Bartycka 18, PL-00-716 Warsaw, Poland*

[42]*IRFU, CEA, Université Paris-Saclay, Bât 141, F-91191 Gif-sur-Yvette, France*

[43]*Centre for Advanced Instrumentation, Department of Physics, Durham University, South Road, Durham DH1 3LE, UK*

[44]*INAF – Osservatorio di Astrofisica e Scienza dello spazio di Bologna, Via Piero Gobetti 93/3, I-40129 Bologna, Italy*

[45]*University of Geneva – Département de physique nucléaire et corpusculaire, 24 rue du Général-Dufour, CH-1211 Genève 4, Switzerland*

[46]*CCTVal, Universidad Técnica Federico Santa María, Avenida España 1680, Valparaíso, Chile*

[47]*The Henryk Niewodniczański Institute of Nuclear Physics, Polish Academy of Sciences, ul. Radzikowskiego 152, PL-31-342 Cracow, Poland*

[48]*INAF – Osservatorio Astronomico di Capodimonte, Via Salita Moiariello 16, I-80131 Napoli, Italy*

[49]*Aix Marseille Univ, CNRS/IN2P3, CPPM, 13288 Marseille cedex 09, France*

[50]*Université Paris Cité, CNRS, CEA, Astroparticule et Cosmologie, F-75013 Paris, France*

[51]*University of the Witwatersrand, 1 Jan Smuts Avenue, Braamfontein, 2000 Johannesburg, South Africa*

[52]*INFN Sezione di Torino, Via P. Giuria 1, I-10125 Torino, Italy*

[53]*Dipartimento di Fisica – Universitá degli Studi di Torino, Via Pietro Giuria 1, I-10125 Torino, Italy*

[54]*Palacký University Olomouc, Faculty of Science, Joint Laboratory of Optics of Palacký University and Institute of Physics of the Czech Academy of Sciences, 17. listopadu 1192/12, 779 00 Olomouc, Czech Republic*

[55]*INAF – Osservatorio Astrofisico di Catania, Via S. Sofia, 78, I-95123 Catania, Italy*

[56]*University of Oxford, Department of Physics, Clarendon Laboratory, Parks Road, Oxford OX1 3PU, UK*

[57]*INAF – Istituto di Astrofisica Spaziale e Fisica Cosmica di Milano, Via A. Corti 12, I-20133 Milano, Italy*

[58]*LUTH, GEPI and LERMA, Observatoire de Paris, Université PSL, Université Paris Cité, CNRS, 5 place Jules Janssen, F-92190 Meudon, France*

[59]*INAF – Istituto di Radioastronomia, Via Gobetti 101, I-40129 Bologna, Italy*

[60]*INAF – Istituto Nazionale di Astrofisica, Viale del Parco Mellini 84, I-00136 Rome, Italy*

[61]*Instituto de Astronomia, Geofísico, e Ciências Atmosféricas – Universidade de São Paulo, Cidade Universitária, R. do Matão, 1226, CEP 05508-090, São Paulo, SP, Brazil*

[62]*Instituto de Física de São Carlos, Universidade de São Paulo, Av. Trabalhador São-carlense, 400 – CEP 13566-590, São Carlos, SP, Brazil*

[63]*Max-Planck-Institut für Kernphysik, Saupfercheckweg 1, D-69117 Heidelberg, Germany*

[64]*Universitá degli Studi di Napoli 'Federico II' - Dipartimento di Fisica 'E. Pancini', Complesso Universitario di Monte Sant'Angelo, Via Cintia, I-80126 Napoli, Italy*

[65]*INFN Sezione di Bari and Università degli Studi di Bari, via Orabona 4, I-70124 Bari, Italy*

[66]*Institut für Astronomie und Astrophysik, Universität Tübingen, Sand 1, D-72076 Tübingen, Germany*

[67]*Université Bordeaux, CNRS, LP2I Bordeaux, UMR 5797, 19 Chemin du Solarium, F-33170 Gradignan, France*

[68]*Department of Astronomy and Astrophysics, University of Chicago, 5640 S Ellis Ave, Chicago, IL 60637, USA*

[69]*LAPTh, CNRS, USMB, F-74940 Annecy, France*

[70]*Institut für Physik & Astronomie, Universität Potsdam, Karl-Liebknecht-Strasse 24/25, D-14476 Potsdam, Germany*

[71]*Escola de Artes, Ciências e Humanidades, Universidade de São Paulo, Rua Arlindo Bettio, CEP 03828-000, 1000 São Paulo, Brazil*

[72]*Astronomical Observatory of Taras Shevchenko National University of Kyiv, 3 Observatorna Street, Kyiv 04053, Ukraine*

[73]*University of California, Davis, One Shields Ave., Davis, CA 95616, USA*

[74]*RIKEN, Institute of Physical and Chemical Research, 2-1 Hirosawa, Wako, Saitama, 351-0198, Japan*

[75]*Western Sydney University, Locked Bag 1797, Penrith, NSW 2751, Australia*

[76]*INAF – Istituto di Astrofisica e Planetologia Spaziali (IAPS), Via del Fosso del Cavaliere 100, I-00133 Roma, Italy*

[77]*Department of Physics, Nagoya University, Chikusa-ku, Nagoya, 464-8602, Japan*

[78]*INFN Sezione di Pisa, Edificio C – Polo Fibonacci, Largo Bruno Pontecorvo 3, I-56127 Pisa, Italy*

[79]*INFN Sezione di Roma Tor Vergata, Via della Ricerca Scientifica 1, I-00133 Rome, Italy*

[80]*Alikhanyan National Science Laboratory, Yerevan Physics Institute, 2 Alikhanyan Brothers St., 0036 Yerevan, Armenia*

[81]*INFN Sezione di Catania, Via S. Sofia 64, I-95123 Catania, Italy*

[82]*Departamento de Engenharias e Exatas, Universidade Federal Do Paraná - Setor Palotina, Rua Pioneiro, 2153, Jardim Dallas, CEP: 85950-000 Palotina, Paraná, Brazil*

[83]*Núcleo de Astrofísica e Cosmologia (Cosmo-ufes) & Departamento de Física, Universidade Federal do Espírito Santo (UFES), Av. Fernando Ferrari, 514. 29065-910. Vitória-ES, Brazil*

[84]*Astrophysics Research Center of the Open University (ARCO), The Open University of Israel, PO Box 808, Ra'anana 4353701, Israel*

[85]*Department of Physics, The George Washington University, Washington, DC 20052, USA*

[86]*FZU – Institute of Physics of the Czech Academy of Sciences, Na Slovance 1999/2, CZ-18221 Praha 8, Czech Republic*

[87]*National Institute of Technology, Ichinoseki College, Hagisho, Ichinoseki, Iwate 021-8511, Japan*

[88]*Universidad Nacional Autónoma de México, Delegación Coyoacán, 04510 Ciudad de México, Mexico*

[89]*Department of Physics and Astronomy and the Bartol Research Institute, University of Delaware, Newark, DE 19716, USA*

[90]*Universität Innsbruck, Institut für Astro- und Teilchenphysik, Technikerstr. 25/8, 6020 Innsbruck, Austria*

[91]*Dipartimento di Scienze Fisiche e Chimiche, Università degli Studi dell'Aquila and GSGC-LNGS-INFN, Via Vetoio 1, L'Aquila 67100, Italy*

[92]*Astronomical Observatory, Jagiellonian University, ul. Orla 171, PL-30-244 Cracow, Poland*

[93]*Friedrich-Alexander-Universität Erlangen-Nürnberg, Erlangen Centre for Astroparticle Physics, Nikolaus-Fiebiger-Str. 2, D-91058 Erlangen, Germany*

[94]*Astronomical Institute of the Czech Academy of Sciences, Bocni II 1401, CZ-14100 Prague, Czech Republic*

[95]*Faculty of Science, Ibaraki University, Mito, Ibaraki, 310-8512, Japan*

[96]*Institut de Fisica d'Altes Energies (IFAE), The Barcelona Institute of Science and Technology, Campus UAB, E-08193 Bellaterra (Barcelona), Spain*

[97]*Institut de Recherche en Astrophysique et Planétologie, CNRS-INSU, Université Paul Sabatier, 9 avenue Colonel Roche, BP 44346, F-31028 Toulouse Cedex 4, France*

[98]*Dept. of Physics and Astronomy, University of Leicester, Leicester LE1 7RH, UK*

[99]*Sorbonne Université, CNRS/IN2P3, Laboratoire de Physique Nucléaire et de Hautes Energies, LPNHE, 4 place Jussieu, F-75005 Paris, France*

[100]*Università degli studi di Catania, Dipartimento di Fisica e Astronomia 'Ettore Majorana', Via S. Sofia 64, I-95123 Catania, Italy*

[101]*Finnish Centre for Astronomy with ESO, University of Turku, Finland, FI-20014 University of Turku, Finland*

[102]*Department of Physics, Humboldt University Berlin, Newtonstr. 15, D-12489 Berlin, Germany*

[103]*INFN Sezione di Trieste and Università degli Studi di Trieste, Via Valerio 2 I, I-34127 Trieste, Italy*

[104]*Escuela Politécnica Superior de Jaén, Universidad de Jaén, Campus Las Lagunillas s/n, Edif. A3, E-23071 Jaén, Spain*

[105]*Anton Pannekoek Institute/GRAPPA, University of Amsterdam, Science Park 904, NL-1098 XH Amsterdam, the Netherlands*

[106]*Saha Institute of Nuclear Physics, Bidhannagar, Kolkata-700 064, India*

[107]*Dipartimento di Fisica e Chimica 'E. Segrè', Università degli Studi di Palermo, Via Archirafi 36, I-90123 Palermo, Italy*

[108]*INFN and Università degli Studi di Siena, Dipartimento di Scienze Fisiche, della Terra e dell'Ambiente (DSFTA), Sezione di Fisica, Via Roma 56, I-53100 Siena, Italy*

[109]*Department of Physics, Columbia University, 538 West 120th Street, New York, NY 10027, USA*

[110]*Department of Physics, Yamagata University, Yamagata, Yamagata 990-8560, Japan*

[111]*University of Białystok, Faculty of Physics, ul. K. Ciołkowskiego 1L, PL-15-245 Białystok, Poland*

[112]*Department of Physics, Tokai University, 4-1-1, Kita-Kaname, Hiratsuka, Kanagawa 259-1292, Japan*

[113]*Charles University, Institute of Particle & Nuclear Physics, V Holešovičkách 2, CZ-180 00 Prague 8, Czech Republic*

[114]*Astronomical Observatory of Ivan Franko National University of Lviv, 8 Kyryla i Mephodia Street, Lviv, 79005, Ukraine*

[115]*Institute for Space—Earth Environmental Research, Nagoya University, Furo-cho, Chikusa-ku, Nagoya 464-8601, Japan*

[116]*Kobayashi—Maskawa Institute for the Origin of Particles and the Universe, Nagoya University, Furo-cho, Chikusa-ku, Nagoya 464-8602, Japan*

[117]*Department of Physics and Astronomy, University of California, Los Angeles, CA 90095, USA*

[118]*Graduate School of Technology, Industrial and Social Sciences, Tokushima University, Tokushima 770-8506, Japan*

[119]*Cherenkov Telescope Array Observatory, Saupfercheckweg 1, D-69117 Heidelberg, Germany*

[120]*INAF - Istituto di Astrofisica Spaziale e Fisica Cosmica di Palermo, Via U. La Malfa 153, I-90146 Palermo, Italy*

[121]*University of Pisa, Largo B. Pontecorvo 3, I-56127 Pisa, Italy*

[122]*University of Rijeka, Faculty of Physics, Radmile Matejcic 2, 51000 Rijeka, Croatia*

[123]*INAF – Osservatorio Astronomico di Padova, Vicolo dell'Osservatorio 5, I-35122 Padova, Italy*

[124]*International Institute of Physics, Universidade Federal do Rio Grande do Norte, 59078-970 Natal, RN, Brasil*

[125]*Departamento de Física, Universidade Federal do Rio Grande do Norte, 59078-970, Natal, RN, Brasil*

[126]*Landessternwarte, Zentrum für Astronomie der Universität Heidelberg, Königstuhl 12, D-69117 Heidelberg, Germany*

[127]*Centre for Astro-Particle Physics (CAPP) and Department of Physics, University of Johannesburg, PO Box 524, Auckland Park 2006, South Africa*

[128]*Departamento de Astronomía, Universidad de Concepción, Barrio Universitario S/N, Concepción, Chile*

[129]*INAF – Osservatorio Astronomico di Brera, Via Brera 28, I-20121 Milano, Italy*

[130]*Main Astronomical Observatory of the National Academy of Sciences of Ukraine, Zabolotnoho Str., 27, 03143, Kyiv, Ukraine*

[131]*Space Technology Centre, AGH University of Science and Technology, Aleja Mickiewicza, 30, PL-30-059, Kraków, Poland*

[132]*Academic Computer Centre CYFRONET AGH, ul. Nawojki 11, PL-30-950, Kraków, Poland*

[133]*Cherenkov Telescope Array Observatory gGmbH, Via Gobetti, 40129 Bologna, Italy*

[134]*Department of Physical Science, Hiroshima University, Higashi-Hiroshima, Hiroshima 739-8526, Japan*

[135]*Institute of Space Sciences (ICE, CSIC), and Institut d'Estudis Espacials de Catalunya (IEEC), and Institució Catalana de Recerca I Estudis Avançats (ICREA), Campus UAB, Carrer de Can Magrans, s/n 08193 Cerdanyola del Vallés, Spain*

[136]*INAF – Osservatorio Astrofisico di Torino, Strada Osservatorio 20, I-10025 Pino Torinese (TO), Italy*

[137]*School of Physical Sciences, University of Adelaide, Adelaide SA 5005, Australia*

[138]*Department of Physical Sciences, Aoyama Gakuin University, Fuchinobe, Sagamihara, Kanagawa, 252-5258, Japan*

[139]*School of Physics and Astronomy, Sun Yat-sen University, 519082 Zhuhai, China*

This paper has been typeset from a TEX/LATEX file prepared by the author.